Open Research Online

The Open University's repository of research publications
and other research outputs

Detecting, locating and sizing leaks in gas-filled pipes using acoustical measurements

Thesis

How to cite:

Chilekwa, Victor (2006). Detecting, locating and sizing leaks in gas-filled pipes using acoustical measurements. PhD thesis The Open University.

For guidance on citations see FAQs.

© 2006 The Author

https://creativecommons.org/licenses/by-nc-nd/4.0/

Version: Version of Record

Link(s) to article on publisher's website:
http://dx.doi.org/doi:10.21954/ou.ro.0000add1

Copyright and Moral Rights for the articles on this site are retained by the individual authors and/or other copyright owners. For more information on Open Research Online's data policy on reuse of materials please consult the policies page.

oro.open.ac.uk

DETECTING, LOCATING AND SIZING LEAKS IN GAS-FILLED PIPES USING ACOUSTICAL MEASUREMENTS

Victor Chilekwa, MSc. BSc.

Thesis submitted to the Open University in part fulfilment of the requirements of the degree of Doctor of Philosophy

Department of Environmental and Mechanical Engineering

Technology Faculty

The Open University

30th. September 2006

DECLARATION

I declare that this thesis has been composed by me and that the work is my own.

ABSTRACT

A single leak in a duct can be detected, located and sized by measuring the input impedance of the duct and then analytically solving an inverse problem. However, previously applied analytical methods break down when it comes to predicting smaller hole sizes. Results are presented which show that, by treating smaller holes as capillaries and applying appropriate theoretical approximations, accurate predictions of smaller hole sizes are possible.

Extending the analytical methods to a duct containing multiple leaks is non-trivial as the resulting mathematical expressions are highly complex. In this thesis, an alternative approach which uses optimisation methodology to detect, locate and size multiple leaks in a duct is described. The optimisation algorithms are applied to a measurement of the duct's input impedance but they are able to cope with the presence of multiple leaks. Results are presented which illustrate the success of the optimisation approach in detecting, locating and sizing multiple leaks in a duct.

An objective function incorporating the theoretical input impedance of a model duct and experimental input impedance of the cylindrical pipe under investigation is designed. By studying the behaviour of the objective function and the application of different numerical optimisation methods, it is possible to determine those methods most suitable for investigating leaks. Results are presented showing that the Rosenbrock optimisation algorithm provides predictions of hole sizes and locations which are in good agreement with their actual values. The success of the Rosenbrock optimisation algorithm is attributed to function minimisation techniques incorporating non derivative based search directions and optimisation steps.

PUBLICATIONS ARISING

Conference Papers

V. Chilekwa, D.B. Sharp and T.J.W. Hill (2003), *Leak detection in musical wind instruments using acoustic pulse reflectometry***.** Proceedings of the Stockholm Music Acoustics Conference, August 6-9, 2003 (SMAC 2003), Stockholm, Sweden

V. Chilekwa and D.B. Sharp (2005), *"Detection, location and sizing of multiple leaks in a duct.* Proc. of Forum Acusticum 2005, Budapest, Hungary, 29 August - 02 September 2005; pp. 2569-2572

D.B. Sharp and V. Chilekwa (2006), *An optimisation approach to the location and sizing of multiple leaks in a duct*. Proceedings of the Institute of Acoustics Spring Conference, Southampton, 3-4 April 2006.

ACKNOWLEDGEMENTS

I would like to express profound gratitude to my supervisor, Dr. David Sharp, for his invaluable support, encouragement and guidance throughout the PhD. I am also highly thankful to my Head of Department Dr Rod Barratt and members of the Environmental and Mechanical Engineering department for their valuable inputs throughout my studies. Thanks must also go to the Open University for providing research funds which afforded me the chance to pursue this PhD.

Jim Whitehouse and Pete Seabrook made good company throughout my research studies and assisted in the physical production of this thesis.

I am grateful to members of the Instituts für Wiener Klangstil, Austria for collaborating with some aspects of this research. Professor Wilfried Kausel was instrumental in providing useful insight in the subject of optimization and provided parts of the code used in the investigations.

I am as ever, especially indebted to my wife and two lovely daughters for their love and support throughout my research studies. I also wish to thank my parents, brothers and sisters, who constantly show interest in my progress.

CONTENTS

LIST OF TABLES

LIST OF FIGURES

Chapter 1

Introduction

This report investigates the detection, locating and sizing of multiple leaks in ducts using acoustical means. The work develops and assesses a novel and efficient method for investigating leaks in tubular systems. The method involves acquiring response data using an acoustic pulse reflectometer and applying appropriate analytical or numerical optimisation algorithms. This work builds on research by Sharp [1] who used an acoustic pulse reflectometer to investigate single leaks present in the walls of musical wind instruments.

Acoustic pulse reflectometry involves measuring the time sequence of reflections produced when a sound pulse is injected into a duct of varying cross-sectional area. A leak, or hole, in the duct wall presents a significant change in impedance to the probing sound pulse. Information about the leak can be gained by applying theoretical equations to the change in impedance measured by the acoustic pulse reflectometer.

Originally, acoustic pulse reflectometry was developed as a seismological technique for the observation of stratifications in the earth's crust. It was first used to investigate ducts in the medical field in 1970 when it was applied to the measurements of airway dimensions [2-4]. A decade later, Benade and Smith [5] described an early attempt to measure the input impulse response of a musical wind instrument using acoustic pulse reflectometry. This research was continued by Smith [6], Watson and Bowsher [7, 8] and Watson [9]. They presented bore reconstructions of various brass instruments calculated from their input impulse responses. Sharp et al [10] extended the method of pulse reflectometry to enable single leaks in ducts to be monitored. The research described in this thesis develops Sharp's work to allow the inspection of ducts containing more than one leak. Another

aspect considered in this research is the inspection of leaks of capillary size, which thus far has not been developed.

Acoustic pulse reflectometry has the potential of offering a good alternative to the leak detection methods currently used in industry. This is particularly true in cases where the radius of the tubular system under investigation is less than the wavelength of the sound passing through the tube (i.e. for tubes of, say, less than 10 mm in radius) such that plane wave propagation can be assumed. The potential of the method is enhanced by the ability to predict the size of the leaks present; the more common methods in use only go as far as detecting and locating leaks. Furthermore, unlike the more common techniques, the method presented in this work has been extended to locating and predicting the number and sizes of multiple leaks which may be present in a tubular system. The method is also able to cope with the detection of very small leaks which is a rare feature in the current industrial methods of leak detection.

The other advantages of the method presented in this work are inherent in the fact that it is an acoustical method. Acoustical methods in general use digital signal processing and computing capabilities to process the data. As a result, they are easily standardised and less susceptible to human error than conventional methods. They tend to be non-intrusive as they are based on using a recording device to capture information from reflected sound signals instead of having to make physical measurements on the tube.

For the purpose of research, the acoustic pulse reflectometer has an advantage in that it can be fully constructed in the laboratory at a relatively low cost. The microphones which form part of the reflectometer can be connected to a conventional personal computer to enable sound signals to be recorded for subsequent analysis. The sound signal produced by the reflectometer loudspeaker is also generated by the same computer.

1.1 History of Leak Investigation Methods

Parker [11] presented an excellent historical overview of the development of leak detection methods in gas-filled pipes. He noted that early attempts to develop leak detection methods for gas-filled pipes first appeared in the 1930s and were presented in publications by Smith, [12]; Gilmore [13] ; Richardson [14] ; Larson [15]. Further work was published by McElwee [16]. The basis of all these publications was that, if one couples a sensor such as a microphone to the gas inside the pipe, leak generated noise is clearly audible, because the magnitude of the ambient noise is rendered negligible by high transmission loss through the external soil and the pipe wall. All these efforts were confined to a listening or passive approach.

The first systematic attempt to develop an improved means of leak detection in gas-filled pipes using acoustical methods was initiated in 1950 and continued until 1965. A record of progress in developing an operational system is contained in the publications by Reid and Hogan [17]. The work done by Hogan was significant as it presented a summary of the results of extensive field-testing involving six major gas utilities. He noted that the transfer of the technology to the pipeline operator was a major difficulty due to the complexity of the system and its operation. This same point was raised by Larson [15] in efforts to use a geophone for leak detection. He stated: “Thus far the best results have been obtained from operators who have had some college training along engineering lines.” Although some success in leak location was achieved in these studies, analysis of the data from the extensive field measurements indicated that the main problem was the unpredictable performance of the system, coupled with the inability to predict quantitatively the chance of success or failure in a given situation.

Kovecevich et al [18] discussed pressurized piping and boilers in utility and industrial power plants where acoustic leak detection systems have been in use since the early 1970s. These methods detect the continuous sound waves emanating from the turbulence created by the escaping gas.

Jolly [19] reviewed several different acoustic-based leak detection methods for gas-filled pipes and found the most promising method to be the low frequency impulse detection method. The impulse method uses sensors mounted at the ends of the pipeline. This method could capture the transient acoustic event associated with a rapid rupture. But the method could not detect small leaks, which grow over several hours. He found that when sensors are mounted on the outside of the pipe to detect the noise of a leak, the frequency range is typically 5 kHz to 300 kHz.

For the case of water-filled pipes, historically, much acoustical leak detection was carried using a crow bar or screw driver held firmly against a pipe to transmit sounds to the operator's ear [20]. There are still practitioners of this method now but today's pipe materials and operating conditions make these older methods much more difficult. Also, noise from vehicles or other machinery can be serious distractions to leak detection listening. Before 1980, the only methods used for leak detection in the water industry were conventional sounding techniques [20].

However, the great cost of losing treated water through leaks, and of repairing pipes due to unmonitored cracks, created a need for improved methods of leak detection. An example of the concern about leaks in the 1980s is the published results of the survey carried out in 70 European Cities [21] by the Standing Committee on Water Distribution of the International Water Supply Association (IWSA). The study established an average loss in the water supply networks of 15 %. These leaks in pipes caused unnecessary waste of

scarce resources and often endangered the environment. There was a clear understanding that improved methods of leak detection were required to reduce leaks. For example the American Water Works Association (AWWA) stated that an improvement of leak detection was “indispensable” [22], though at that time some successful techniques in use today were overlooked. They said of the acoustical correlation analysis that the method was found to be accurate within one to two metres, but proved expensive and time consuming for commercial application; thus its use is limited to difficult and unusual situations [23]. A more positive conclusion from these early records is the decision by the Fraunhofer-Institut fur Bauphysik (IBP), at the suggestion of Technische Werke der Stadt Stuttgart (TWS), to undertake an improvement of the then known acoustical inspection methods [24] with modern sensors and signal processing so that the leak detection can be made more effective.

Currently, one of the most practiced acoustical methods for leak detection in water-filled pipes is the cross-correlation method [25]. The method typifies the great advances in modern leak detection techniques. It is a computer based method (more reliable as it does not depend on the judgment of the operator) and provides a non-intrusive means of discovering and locating leaks rapidly. With this method, the sensors are attached at two points of contact (normally fire hydrants) with the pipe that bracket a suspected leak. The signals are transmitted from the sensors to the processing unit wirelessly. The processing unit computes the cross-correlation function of the two leak signals to determine the time lag between them. It then calculates the location of the leak based on a simple algebraic relationship between the time lag, sensor-to-sensor spacing, and sound propagation velocity in the pipe. The method consists of leak noise correlators, acoustic sensors such as accelerometers and hydrophones, wireless signal transmitters and receivers, and an electronic processing unit.

As a result of the earlier efforts discussed above and other initiatives reflected across the globe, several methods have been successfully developed and used to investigate leaks in tubular systems. The different methods have been developed to suit specific characteristics of the system being investigated and the level of information required. The methods can be broadly classified into non-acoustical and acoustical methods. The non-acoustical methods have developed from the basic leak detection techniques such as immersing a pumped tyre in water and observing the presence of bubbles due to the existence of leaks. Some of the non-acoustical methods currently in use are the penetrating dye, halogen, helium mass spectrometer methods. These methods have found use in detecting leaks in vacuum chambers, TV-cathode tubes, pressure vessels, aerosol containers, pumps, refrigeration systems, chemical and nuclear plants, beverage cans, electron microscopes etc. However these methods are not applicable in tubular systems where the length of the pipe can be a big limitation and acoustical methods tend to be preferred for this very reason.

1.2 Aims and Outline of Thesis

The aim of this research is to acquire acoustical signals from ducts using an acoustic pulse reflectometer and to use existing theory to extract information about leaks from the signals. The information extracted from the acoustical signals should offer solutions regarding the detection of leaks, location of the leaks and prediction of their sizes.

The specific goals of the research are to:

- review existing theory relevant to investigating leaks by acoustical means;
- repeat and evaluate the bore reconstruction methodology proposed by Sharp [1] for detecting and locating the position of a single leak in a duct;
- repeat and evaluate the analytical methods proposed by Sharp [1] for predicting the size of a single leak;

- extend the analytical methods for predicting the size of a single leak to holes of capillary size;
- use numerical optimisation to locate and size multiple leaks in a duct;
- use numerical optimisation to predict the number of leaks in a duct.

Chapter 2 deals with the basic duct theory. The chapter gives the definition of acoustic impedance and presents various different impedance equations. In particular, equations describing the change in impedance at a change in cross-sectional area within an object of cylindrical symmetry are considered. The input impedance of both a non-leaking and a leaking cylindrical pipe are also presented.

In Chapter 3, the technique of acoustic pulse reflectometry is discussed in detail together with the theory describing the acoustic reflections that result when a sound wave propagates within a tubular object of varying cross-sectional area. Equations for calculating the input impedance from measured acoustic reflections are developed and presented.

In Chapter 4, an analytical method for predicting the size of a single leak is discussed. Predictions of the sizes of different holes determined from acoustic pulse reflectometry measurements of the input impedance of a cylindrical pipe are presented. Finally, it is demonstrated that this analytical method cannot be extended to the investigation of multiple leaks.

In Chapter 5, the theory and methods of numerical optimisation are presented. The methods are discussed under the headings of single variable, two variable and multi variable optimisation methods.

In Chapter 6, numerical optimisation methods are applied to the problem of investigating a single leak in the wall of a cylindrical pipe. Predictions of both the size and position of a single leak are presented. A recommendation of which numerical optimisation methods are suitable for leak investigation problems is made.

In Chapter 7, the Rosenbrock algorithm, which is a zeroth order numerical optimisation method, is described and applied to the case of investigating multiple leaks in a cylindrical pipe. The method is first applied used to predict the size of two leaks of known location in the wall of the cylindrical pipe. The method is then extended to the prediction of both the sizes and the positions of three leaks. Finally, the Rosenbrock algorithm is used to predict the number of leaks in the wall of the cylindrical pipe.

The final chapter summarises the findings of this research and presents a series of recommendations for further work.

Chapter 2

Basic Duct Acoustics

2.1 Introduction

Sound can be defined as a disturbance in pressure that propagates through a compressible medium in the form of a longitudinal wave. In free air, sound waves propagate in a complex three dimensional manner. In an air-filled duct however, the waves are constrained to travel in one direction. These waves will propagate with either planar or non-planar wavefronts depending on their wavelength relative to the radius of the duct.

For acoustic waves of low frequency travelling in a cylindrical tube, plane wave propagation can be assumed. At such low frequencies, involving acoustic waves of sufficiently large wavelength, higher order modes are evanescent. That is, they decay rapidly with distance along the duct and so do not propagate.

The frequency at which each higher order mode converts from non-propagating to propagating or vice versa is called the cut-off frequency. The cut-off frequency corresponding to the first non-planar mode is $\omega_c = 1.84\frac{c}{r}$ for an air-filled cylindrical duct of radius r. Expressed in Hertz, this is approximately $f_c = \frac{100}{r}$. For example, in a cylindrical tube of radius r = 5 mm, the first non-planar mode has a cut-off frequency f_c = 20 kHz. At frequencies lower than f_c, higher order modes do not propagate inside

the duct. Consequently, waves with frequencies lower than the cut-off frequency can be considered to propagate as plane waves.

A mathematical description of the propagation of planar acoustic waves in non-leaking and leaking cylindrical ducts is the theme of this chapter.

2.2 Wave Equation in an Air-Filled Duct

The propagation of sound in a gas-filled cylindrical duct is well described by a single equation. The so-called wave equation is derived by considering the variation in length, pressure and density of an arbitrary section of the gas in the duct caused by the passage of a pressure wave.

Consider a section of gas which initially has a length δx. During the passage of the sound wave this length changes. For example, assume that the left face of the gas section moves under the influence of the sound wave from x to $x+\xi(x,t)$, while the right face moves from $x+\delta x$ to $x+\delta x+\xi(x+\delta x,t)$, as indicated in Figure 2-1. Its length has increased from δx to $\delta x+\xi(x+\delta x,t)-\xi(x,t)$. Therefore, its volume has increased by a factor of:

$$1+\left[\frac{\xi(x+\delta x,t)-\xi(x,t)}{\delta x}\right] \tag{2.1}$$

However, in the limit of small δx this is simply $1+\frac{\partial \xi}{\partial x}$ and so the volume of the section of gas is seen to have changed to

$$S\delta x\left(1+\frac{\partial \xi}{\partial x}\right) \tag{2.2}$$

where *S* is the cross-sectional area of the duct.

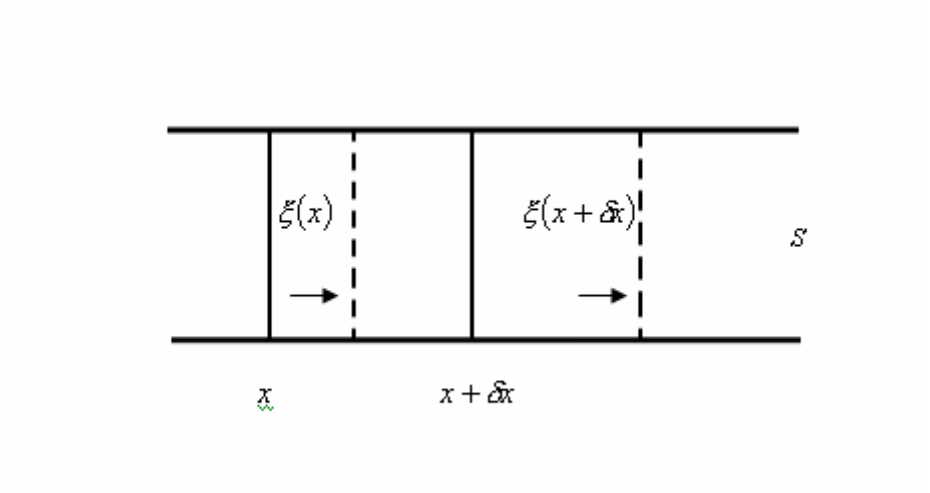

Figure 2-1: Change in the length of a gas section in a duct as an acoustic wave passes. The displacements of the left face and of the right face are not

The change in the pressure experienced by the section of the gas is evaluated by considering the force applied to it. The gas to the left of the section pushes toward the right, exerting a pressure $p_0 + p_1\left[x+\xi(x,t),t\right]$ on the left face of the section, while the gas to the right of the section pushes in the opposite direction exerting a slightly different pressure $p_0 + p_1\left[x+\delta x+\xi(x+\delta x,t),t\right]$, where p_0 is the ambient pressure and p_1 is the additional pressure due to the wave. In the small amplitude approximation, the slight difference between *x* and $x+\xi$ is unimportant in evaluating the function. Therefore, the net

force, F_x, in the x direction caused by the difference in the pressure across the section is given by

$$F_x = S\left[p_1(x,t) - p_1(x+\delta x,t)\right] = S\left(-\frac{\partial p_1}{\partial x}\right)\delta x. \tag{2.3}$$

Using Newton's second law of motion, $F = ma$, where F is the force, m is the mass and a is the acceleration term, the force exerted on the section of gas can also be written as:

$$F_x = \rho_0 S \delta x \frac{\partial^2 \xi}{\partial t^2} \tag{2.4}$$

where ρ_0 is the density of the original section. By combining Equations (2.3) and (2.4) the force term can be replaced as follows:

$$-\frac{\partial p_1}{\partial x} = \rho_0 \frac{\partial^2 \xi}{\partial t^2} \tag{2.5}$$

The final relationship required in the derivation of the wave equation arises from the fact that heat transfer during sound wave propagation is negligible. Under these adiabatic conditions the ideal gas law can be applied which shows that the total pressure p is uniquely determined as a function of the density ρ and that the atmospheric pressure gradient with no wave propagation is written as $\left(\frac{dp}{d\rho}\right)$.

Using a Taylor-series expansion, the pressure can be written as:

$$p \approx p(\rho_0) + (\rho - \rho_0) {}^{dp}\!/_{d\rho} \tag{2.6}$$

However, since $p = p_0 + p_1$, the second term on the right side of equation (2.6) approximates the new pressure p_1. Therefore,

$$p_1 \approx \left(\frac{dp}{d\rho}\right)(\rho - \rho_0) = \left(\frac{dp}{d\rho}\right)\rho_1 \tag{2.7}$$

As the change in density of the gas section is related to the expansion factor arising from the change in length, it can be written as

$$\rho_0 + \rho_1 = {}^{\rho_0}\!/_{\left(1 + \frac{\partial \xi}{\partial x}\right)} \tag{2.8}$$

Assuming that ${}^{\partial \xi}\!/_{\partial x}$ is a small quantity, a binomial expansion can be used to replace $\frac{1}{\left(1 + {}^{\partial \xi}\!/_{\partial x}\right)}$ with $\left(1 - {}^{\partial \xi}\!/_{\partial x}\right)$. Therefore, Equation (2.8) becomes

$$\rho_1 \cong -\rho_0 \frac{\partial \xi}{\partial x} \tag{2.9}$$

By substituting (2.9) into (2.7), the density term ρ_1 can be eliminated to give

$$p_1 = -\rho_0 \frac{dp}{d\rho}\left(\frac{\partial \xi}{\partial x}\right) \tag{2.10}$$

It is now possible to obtain the wave equation directly in terms of pressure by differentiating Equation (2.5) with respect to *x*.

$$\frac{\partial^2 p_1}{\partial x^2} = -\rho_0 \frac{\partial^2}{\partial t^2}\left(\frac{\partial \xi}{\partial x}\right) \tag{2.11}$$

Substituting for $\left(\frac{\partial \xi}{\partial x}\right)$ from Equation (2.10) into Equation (2.11) yields the wave equation:

$$\frac{\partial^2 p_1}{\partial x^2} = \frac{1}{c^2}\frac{\partial^2 p_1}{\partial t^2} \tag{2.12}$$

where *c* is the wave speed and is given by

$$c^2 = \left(\frac{dp}{d\rho}\right) \tag{2.13}$$

For an ideal gas,

$$\frac{p}{p_0} = \left(\frac{\rho}{\rho_0}\right)^{\gamma} \tag{2.14}$$

where γ is the ratio of specific heats. Therefore the wave speed *c* can be written as

$$c = \sqrt{\frac{\gamma p_0}{\rho_0}} \tag{2.15}$$

The relationship between the pressure and density variables is shown by the ideal gas law to be

$$p = \frac{\rho RT}{M} \tag{2.16}$$

where R = 8.314 J/kg-K is the universal gas constant [26], T is the absolute temperature of the gas in degrees Kelvin and M is the average molecular weight of the gas.

Equations (2.15) and (2.16) can be combined to give

$$c = \sqrt{\frac{\gamma RT}{M}} \tag{2.17}$$

For air, M = 0.02895 kg/mol and the ratio of the specific heats γ = 1.4 [26]. Therefore, at 20°C (equal to 293K),

$$c = \sqrt{\frac{1.4 \times 8.314 \times 293}{0.02895}} = 343 \text{ m s}^{-1} \tag{2.18}$$

2.3 Characteristic Impedance

2.3.1 Free Field

The characteristic impedance z_c of a medium is the ratio of sound pressure p to particle velocity u in free field (i.e. in a condition of no reflecting waves). This impedance is a material constant and is equal to the product of the density ρ of the medium and the speed of sound c in that medium.

$$z_c = \frac{p}{u} = \rho c \tag{2.19}$$

2.3.2 Air-Filled Cylindrical Duct

Due to the restrictions imposed by the dimensions of the cylindrical tube on the propagating acoustic wave, boundary conditions are introduced and it is convenient to introduce the volume velocity, $U = Su$, where S is the cross-sectional area of the tube and u is the particle velocity. The acoustic impedance at any cross-section in the tube is defined as the ratio of the pressure and the volume velocity:

$$Z = \frac{p}{U} \tag{2.20}$$

Combining equations (2.19) and (2.20), the acoustic impedance at a cross-section of area S is given by:

$$Z = \frac{p}{Su} = \pm\frac{\rho c}{S} \tag{2.21}$$

with the positive value applying to waves travelling in the $+x$ direction and the negative value applying to waves travelling in the $-x$ direction. The term $\frac{\rho c}{S}$ is defined as the characteristic impedance Z_c of the fluid-filled duct (in the current discussion, the fluid is air).

2.4 Input Impedance

The input impedance of a duct is defined as the ratio of the pressure and volume velocity at the entrance of the duct.

$$Z_{in} = \frac{p_{in}}{U_{in}} \tag{2.22}$$

where the volume velocity U_{in} is simply the particle velocity u_{in} multiplied by the cross-sectional area S_{in} at the entrance of the duct.

2.4.1 Input Impedance of a Non-Leaking Cylindrical Tube

A common method for evaluating the input impedance of a cylindrical tube involves first calculating the impedance at the end of the tube. By using appropriate formulations the impedance at any point along the tube can then be calculated. Figure 2-2 shows a

schematic diagram of a tube, indicating both the input impedance Z_{in} and the load impedance Z_{load} at the end of the duct.

Figure 2-2: Schematic diagram of a cylindrical duct

Assuming plane wave propagation but including the effect of losses, the input impedance of an air-filled cylinder of length l and radius r is given by [26]:

$$Z_{in} = Z_c \left(\frac{\frac{Z_{load} S}{\rho c} + j \tan \underline{k} l}{1 + j \frac{Z_{load} S}{\rho c} \tan \underline{k} l} \right) = \frac{\rho c}{S} \left(\frac{\frac{Z_{load} S}{\rho c} + j \tan \underline{k} l}{1 + j \frac{Z_{load} S}{\rho c} \tan \underline{k} l} \right) \tag{2.23}$$

where Z_{in} is the input impedance, Z_{load} is the load impedance (at the end of the cylinder), Z_c is the characteristic impedance, ρ is the air density, ω is the angular frequency, and $\underline{k} = k - j\alpha$ is the complex propagation constant, with

$$k = \frac{\omega}{c} \tag{2.24}$$

and

$$\alpha = \frac{1}{rc}\left(\sqrt{\frac{\eta\omega}{2\rho}} + (\gamma - 1)\sqrt{\frac{\kappa\omega}{2\rho C_p}}\right) \tag{2.25}$$

γ is the ratio of the principal specific heats of air, C_p is the specific heat of air at constant pressure, η is the coefficient of shear viscosity of air, κ is the thermal conductivity of air and c is the speed of sound in air. The complex propagation constant by Kinsler [26], described in this section, is an approximation of the complex wave number reported by Keefe [27] which will be introduced and explained in Section 3.2.4.

Note that Keefe [27] gives a more accurate, frequency dependent formulation of Z_c, but the deviation from $\frac{\rho c}{S}$ is extremely small and may therefore be neglected without introducing significant errors.

For an open-ended cylinder, the load impedance Z_{load} is the radiation impedance Z_{rad} which for an unflanged end is given by:

$$Z_{rad} = \frac{1}{4}\frac{\rho c}{S}\underline{k}^2 r^2 + j0.6\frac{\rho c}{S}\underline{k}r \tag{2.26}$$

Substituting Equation (2.26) into (2.23) gives the input impedance of an open-ended air-filled cylinder:

$$Z_{in} = \frac{\rho c}{S}\left(\frac{0.25\underline{k}^2 r^2 + j(0.6\underline{k}r + \tan \underline{k}l)}{(1 - 0.6\underline{k}r \tan \underline{k}l) + j0.25\underline{k}^2 r^2 \tan \underline{k}l}\right) \tag{2.27}$$

For a cylinder which is closed at the far end, the load impedance $Z_{load} = \infty$. In a similar manner, substituting into Equation (2.23) gives the input impedance of a closed-ended air-filled cylinder:

$$Z_{in} = -j\frac{\rho c}{S}\cot \underline{k}l \tag{2.28}$$

2.4.2 Input Impedance of a Leaking Cylindrical Tube

Figure 2-3 shows a schematic diagram of a straight tube which is open at the far end and comprises *n* leaks and *n+1* cylindrical sections. The input impedance of the whole duct, $Z_{in(1)}$, is made up of contributions from the impedances of the *n+1* cylindrical sections and the impedances of the *n* holes in the duct walls.

To calculate $Z_{in(1)}$, the load impedance, $Z_{load(n+1)}$, of the final cylindrical section must first be determined. As this is simply the radiation impedance at the end of the duct [28-30], then $Z_{load(n+1)} = Z_{rad}$ where Z_{rad} is calculated using Equation (2.26).

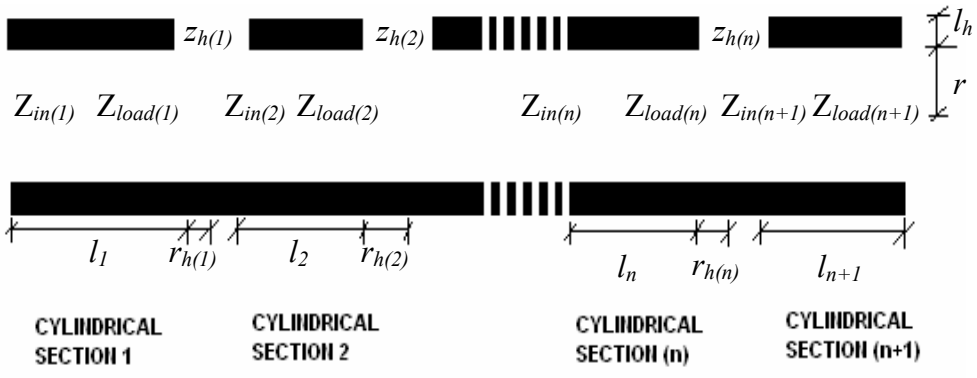

Figure 2-3: Schematic diagram of cylindrical duct with multiple leaks

The next step involves calculating the input impedance, $Z_{in(n+1)}$, of the $(n+1)^{th}$ cylindrical section as follows:

$$Z_{in(n+1)} = \frac{\rho c}{S}\left(\frac{\frac{Z_{load(n+1)}S}{\rho c} + j\tan \underline{k}l_{n+1}}{1 + j\frac{Z_{load(n+1)}S}{\rho c}\tan \underline{k}l_{n+1}}\right) \tag{2.29}$$

Once $z_{in(n+1)}$ has been calculated, $Z_{load(n)}$ can be calculated as follows:

$$Z_{load(n)} = \frac{Z_{h(n)}Z_{in(n+1)}}{Z_{in(n+1)} + Z_{h(n)}} \tag{2.30}$$

where $Z_{h(n)}$ is the impedance of the hole introduced in Section 2.4.3 and discussed in greater detail in Section 4.2.2. In the same manner as was seen in Equation (2.29), the input impedance of the n^{th} cylindrical section is then calculated from the load impedance $Z_{load(n)}$ where:

$$Z_{in(n)} = \frac{\rho c}{S}\left(\frac{\frac{Z_{load(n)}S}{\rho c} + j\tan \underline{k}l_{n}}{1 + j\frac{Z_{load(n)}S}{\rho c}\tan \underline{k}l_{n}}\right) \tag{2.31}$$

and l_n is the length of the n^{th} cylindrical section.

The procedure of calculating the load impedance, hole impedance and input impedance is repeated for each subsequent section until the first cylindrical section is reached and $Z_{in(1)}$ is found.

2.4.3 Input Impedance of a Side Hole

The input impedance of a hole in the wall of a duct can be modelled as the impedance of a short capillary tube. Exact expression for the series impedance and shunt admittance per unit length of capillary tube were derived by Kirchoff in the 19th century [31]. These expressions involve Bessel functions, which makes it difficult to investigate terms such as the radius of the capillary tube given the value of its impedance. However, Benade [5, 32, 33], Backus [28, 29, 34] and Keefe [27, 35, 36] have all introduced approximations which have enabled simplified expressions for the impedance and admittance to be derived in which the Bessel functions are dropped. These approximations depend on the relative sizes of the wavelength of the acoustic wave propagating in the capillary tube and the boundary layer thickness. Two such approximations are discussed in detail in Chapter 4 when they are employed in the calculation of the size of a single leak in a cylindrical duct from a measurement of the input impedance of the duct.

2.5 Conclusion

In this chapter, the theoretical input impedance of both a non-leaking cylindrical tube and a leaking cylindrical tube has been discussed. The input impedance for the non-leaking cylindrical tube has been shown to depend on the load impedance at the end of the tube. For the leaking cylindrical tube, the calculation of the input impedance also depends on the individual impedances of the leaks present in the duct.

The following chapter looks at an experimental method for measuring both the bore profile and the input impedance of a duct. This method is then employed in Chapter 4 to enable the detection, location and prediction of the size of a single leak in the wall of a duct.

Chapter 3

Acoustic Pulse Reflectometry

The methods for detecting, locating and sizing leaks in a duct that are developed in this thesis all rely on first measuring the related properties of input impulse response, bore profile and input impedance. Acoustic pulse reflectometry is a technique which enables the measurement of the input impulse response of a duct. Application of suitable algorithms to this measured input impulse response then enables a bore reconstruction to be calculated and the input impedance of the duct to be determined.

In this chapter, the technique of acoustic pulse reflectometry is described and the algorithms for calculating the bore profile and input impedance of a duct are explained. In addition, examples of input impulse response, bore profile and input impedance measurements made using acoustic pulse reflectometry are presented.

3.1 Acoustic Pulse Reflectometry

The technique of acoustic pulse reflectometry involves measuring the time sequence of reflections that is produced when a sound pulse is injected into a duct of varying cross-sectional area. With this information, and knowledge of the input pulse waveform, the input impulse response of the duct can be calculated. Application of a layer-peeling algorithm then enables the changes in impedance along the duct, and hence the bore profile, to be calculated.

3.1.1 Experimental Apparatus

A typical acoustic pulse reflectometry experimental set-up consists of a signal source, loudspeaker, source tube, microphone, amplification for both input and output signals and couplers for connecting the object under investigation to the source tube (as shown in Figure 3-1).

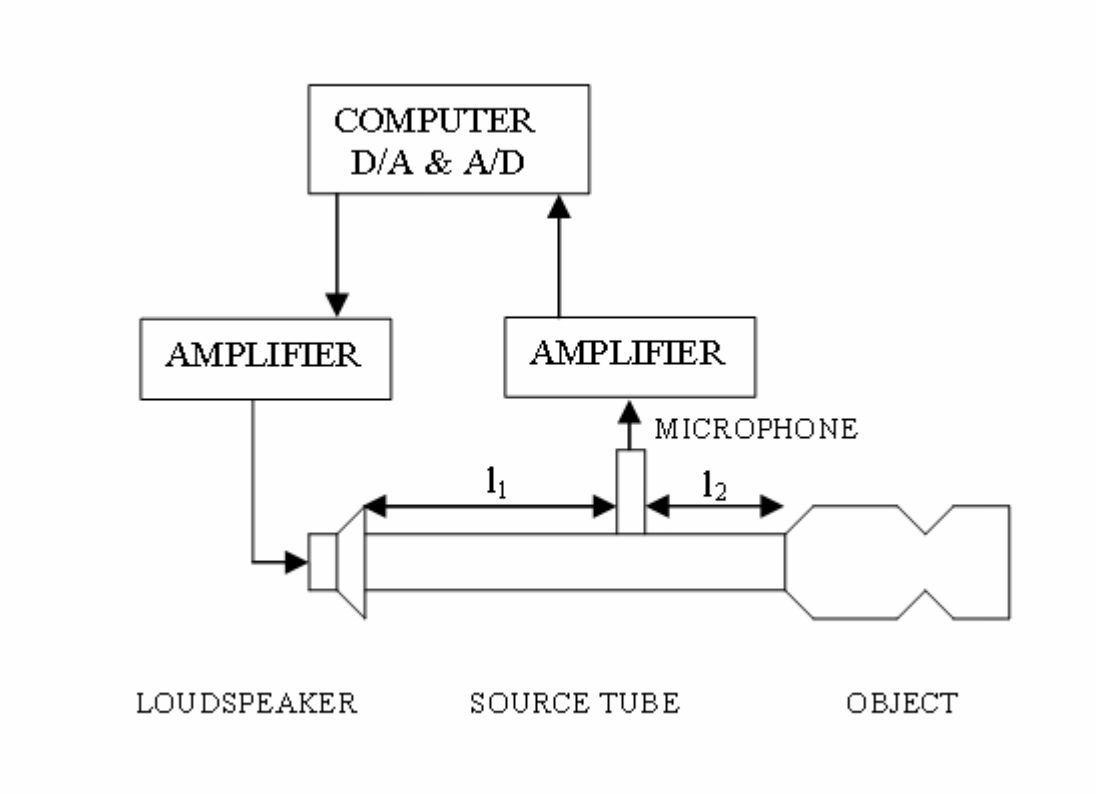

Figure 3-1: Schematic diagram of an acoustic pulse reflectometer

The reflectometer employed in the present study uses a National Instruments NI-6052E data acquisition board connected within a PC to generate an electric pulse. This electrical signal is amplified and sent to a Fane CD150 compression driver loudspeaker. The acoustic pulse that emerges from the loudspeaker is directed down a 6 m long coil of copper tubing (referred to as the source tube) of 5 mm internal radius into the object under investigation.

The reflections that return from the object are recorded by a Knowles EK3132 microphone embedded halfway along the length of the source tube (a distance l_1 = 3 m from the loudspeaker and a distance l_2 = 3 m from the coupling to the object). The distance l_2 ensures that there is no overlap of the reflections returning from the object with the tail of the excitation pulse. The distance l_1 ensures there is no overlap of the object reflections with further reflections from the loudspeaker. Using a sampling frequency of 50 kHz, the National Instruments data acquisition board samples the microphone signal which is then stored on the PC for subsequent signal processing. To improve the signal-to-noise ratio, the measurement procedure is repeated 1000 times and the samples are averaged.

3.1.2 Input Impulse Response

In order to determine the input impulse response of an object, it is necessary to remove the effects of the input pulse shape from the recorded object reflections. The signal processing technique used in this procedure is deconvolution. The input pulse shape is recorded by rigidly terminating the source tube with an end cap and repeating the procedure described in Section 3.1.1. The object reflections are then deconvolved with the input pulse shape to arrive at the input impulse response of the object [1, 37].

To demonstrate the evaluation of the input impulse response of a test object, Figure 3-2 shows an input pulse measured using the reflectometer described in Section 3.1.1. Meanwhile, Figure 3-3 shows the reflections that return from a stepped tube which comprises a cylindrical section of length 0.15 m and radius 5.9 mm and a cylindrical section of length 0.15 m and radius 3.85 mm. Figure 3-4 shows the input impulse response of the stepped tube, calculated by deconvolving the reflections of Figure 3-3 with the input pulse of Figure 3-2.

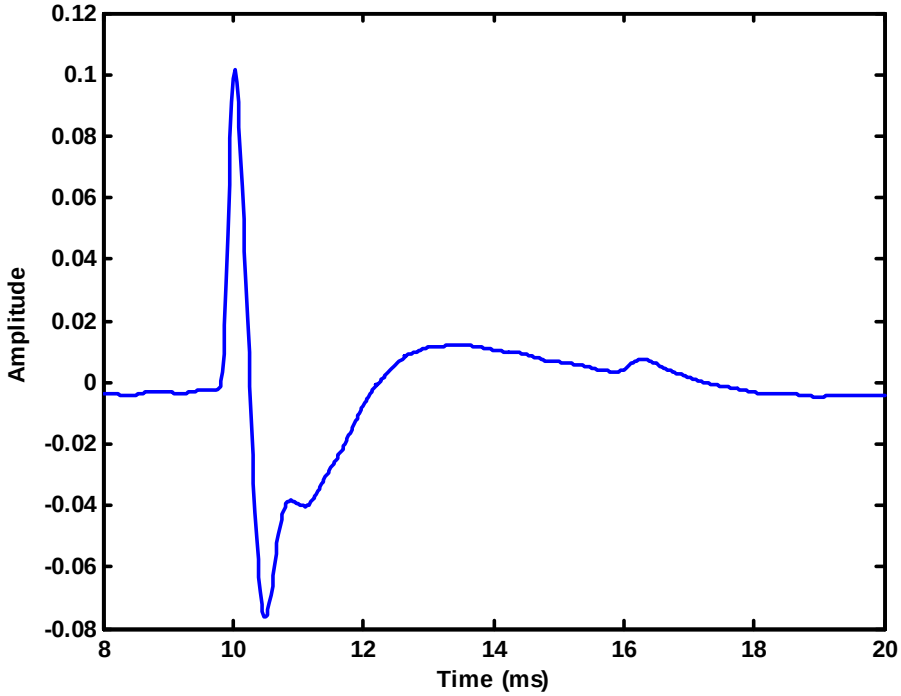

Figure 3-2: Input pulse

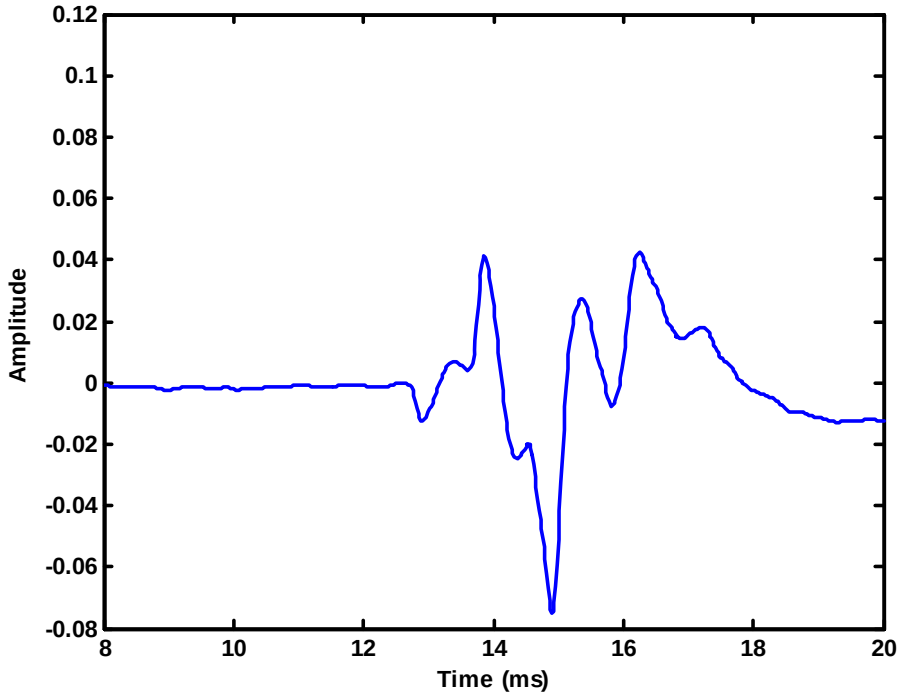

Figure 3-3: Reflections from stepped tube

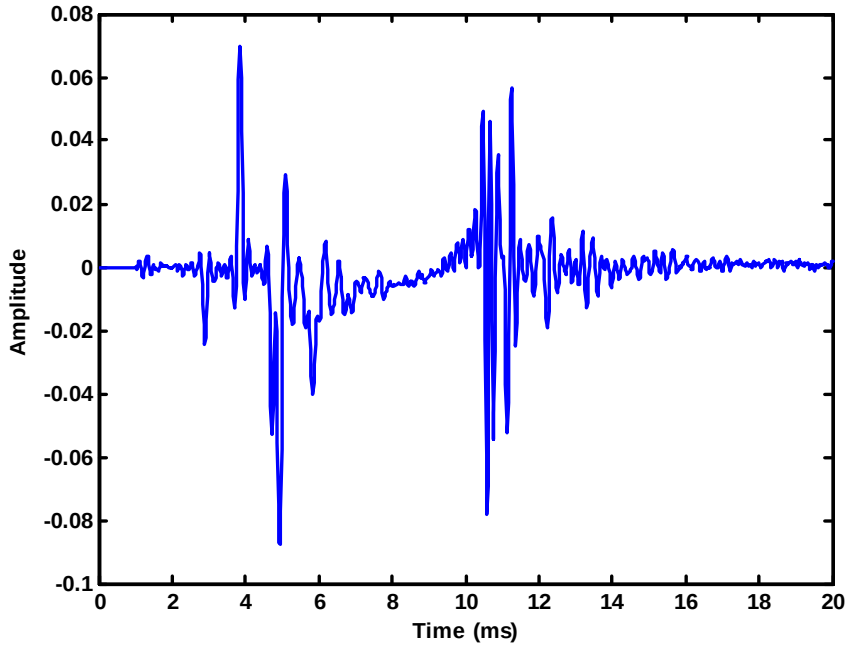

Figure 3-4: Input impulse response of stepped tube

3.2 Theory of Acoustic Reflection

To be in a position to understand how the bore profile and input impedance of a duct can be calculated from its input impulse response, it is first necessary to understand what happens to an acoustic pulse when it propagates within a duct of varying cross-sectional area.

3.2.1 Single Reflection from a Single Discontinuity

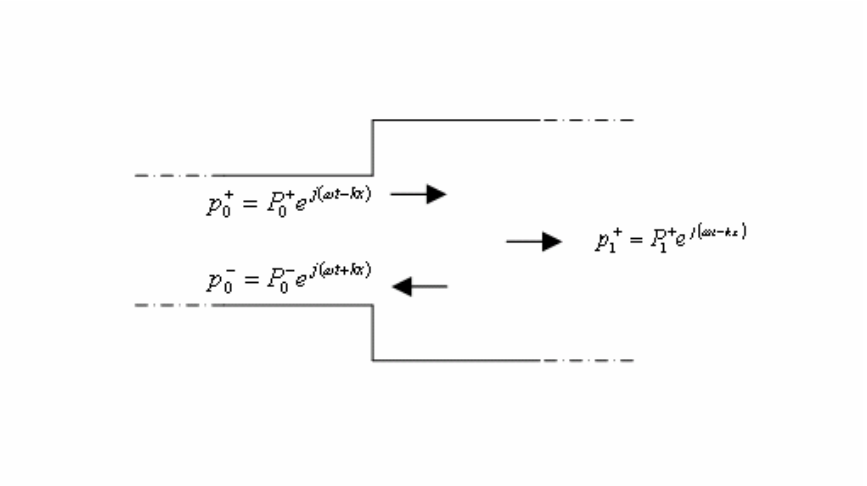

Figure 3-5: Reflection from a single discontinuity

At any change in cross-sectional area in a duct, there is an associated change in the acoustic impedance. As a result, when an acoustic pressure pulse encounters an increase or decrease in cross-sectional area, there is partial reflection and partial transmission of the pulse.

Figure 3-5 shows a cylindrical tube of cross-sectional area S_0 discontinuously joined to a second cylindrical tube of cross-sectional area S_1. When an incident pressure wave

$$p_0^+ = P_0^+ e^{j(\omega t - kx)} \tag{3.1}$$

reaches the boundary between the two cylinders, a reflected wave

$$p_0^- = P_0^- e^{j(\omega t + kx)} \tag{3.2}$$

and a transmitted wave

$$p_1^+ = P_1^+ e^{j(\omega t - kx)} \tag{3.3}$$

are generated. In this notation, $p_j^{\pm}$ indicates that the pressure wave propagates in cylinder j in the positive/negative x direction.

The pressure and velocity must be continuous across the boundary. Therefore, at $x = 0$,

$$p_0^+ + p_0^- = p_1^+ \tag{3.4}$$

$$\frac{p_0^+}{Z_{c0}} - \frac{p_0^-}{Z_{c0}} = \frac{p_1^+}{Z_{c1}} \tag{3.5}$$

(where $Z_{cj} = \frac{\rho c}{S_j}$ is the characteristic impedance of the *j*th cylinder).

Combining Equation (3.4) and Equation (3.5) gives:

$$\frac{p_0^-}{p_0^+} = \frac{Z_{c1} - Z_{c0}}{Z_{c1} + Z_{c0}} = \frac{S_0 - S_1}{S_0 + S_1} \tag{3.6}$$

However, at $x = 0$, the ratio of the instantaneous pressures of the incident and reflected waves is simply the ratio of their pressure amplitudes. Therefore, the reflection coefficient $r_{0,1}$ (the ratio of the pressure amplitude of the reflected wave to that of the incident wave) is

$$r_{0,1} = \frac{P_0^-}{P_0^+} = \frac{p_0^-}{p_0^+} = \frac{S_0 - S_1}{S_0 + S_1} \tag{3.7}$$

In a similar manner, an expression for the transmission coefficient $t_{0,1}$ (the ratio of the pressure amplitude of the transmitted wave to that of the incident wave) can also be found:

$$t_{0,1} = \frac{P_1^+}{P_0^+} = \frac{p_1^+}{p_0^+} = \frac{2S_0}{S_0 + S_1} \tag{3.8}$$

Examination of Equations (3.7) and (3.8) reveals that the reflection and transmission coefficients depend only on the change in cross-sectional area.

For a wave travelling from cylinder 1 towards cylinder 0, the reflection and transmission coefficients for the boundary can be found by interchanging the subscripts in Equations (3.7) and (3.8).

3.2.2 Multiple Reflections from Multiple Discontinuities

An acoustic wave propagating in a duct of varying cross-section will experience partial reflection and transmission at each change in cross-sectional area that it encounters. The result is that, after only a short time, there will be a complicated jumble of forward and backward travelling waves propagating within the duct. In this section, the time history of an acoustic pulse incident on a tubular object of varying cross-section is considered.

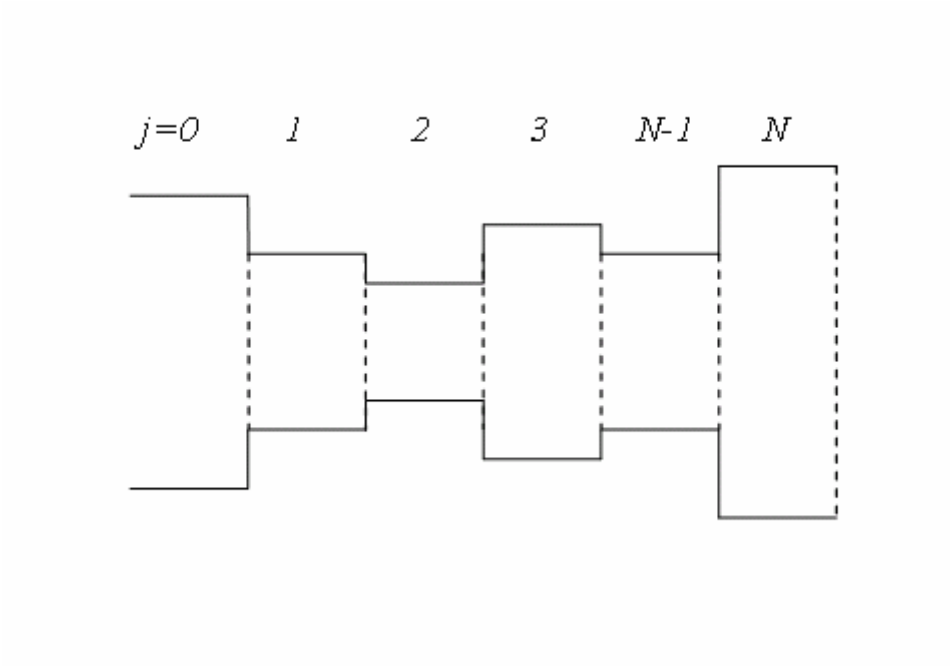

Figure 3-6: Cylindrically segmented tubular object

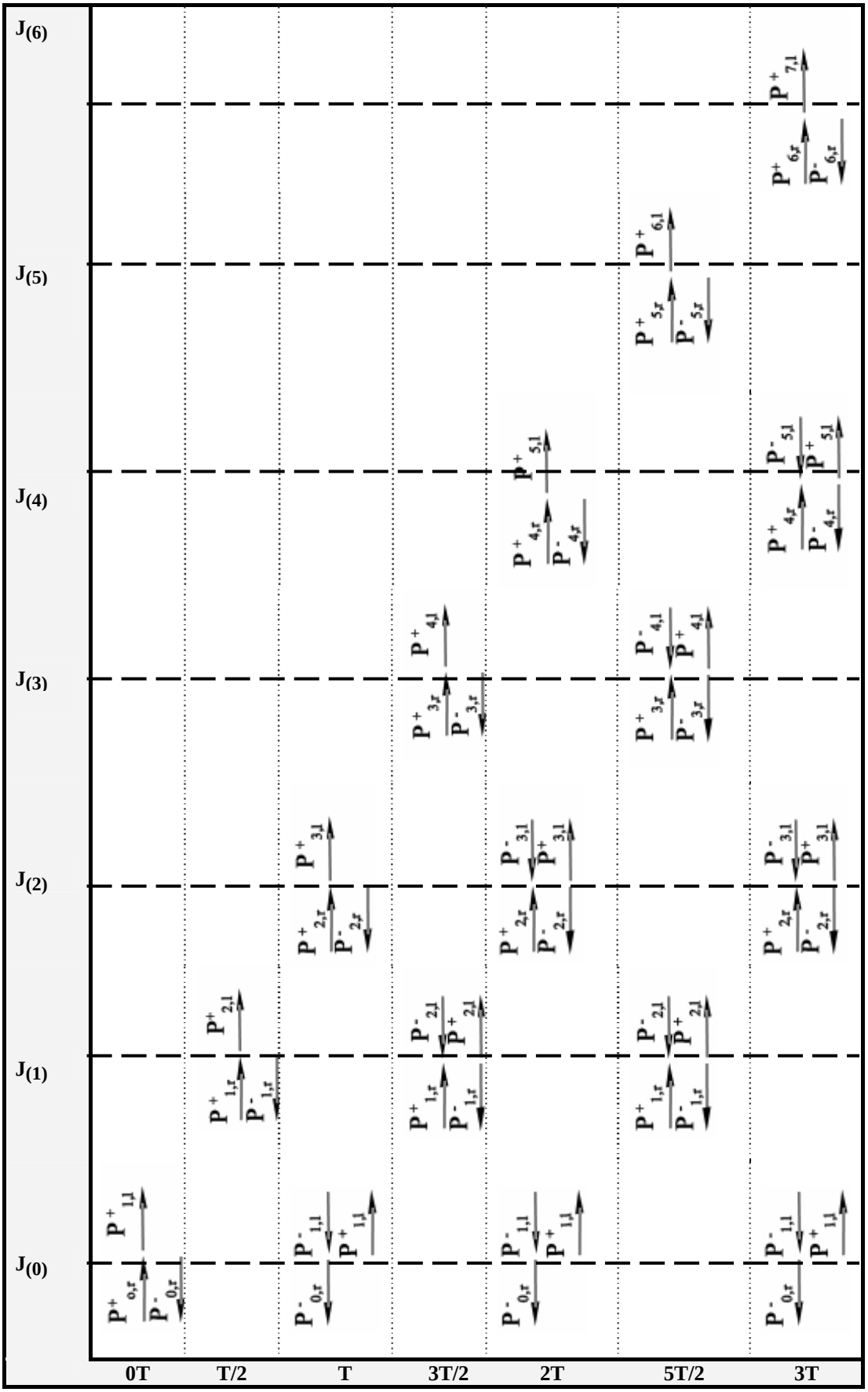

Figure 3-7: Schematic diagram of the time history of an acoustic wave propagating within a duct of varying cross-sectional area

A duct whose cross-sectional area varies with axial distance can be modelled by a series of N cylindrical segments, each of length L with corresponding two way travel time $T = 2L/c$. Figure 3-6 shows such a duct terminated at the left end by a semi-infinite cylinder (defined as being the 0th segment).

When an input pressure signal $p^{+}_{0,r}[nT]$ is incident on the object from the source tube (i.e. incident on the boundary between segments 0 and 1), the signal will be partially reflected and partially transmitted at each inter-segment boundary. In this notation, $p^{\pm}_{j,l/r}[nT]$ represents the contribution from the wave propagating in the positive/negative x direction, to the total pressure at the left/right end of the j^{th} cylindrical segment at the discrete time nT, where $n = 0, \frac{1}{2}, 1, \frac{3}{2} etc.$

If it is first assumed that the signal experiences no losses whilst propagating through the cylindrical segments, the time history of the acoustic wave as it propagates within the object can be displayed schematically (Figure 3-7). The arrows indicate the direction of propagation (forwards or backwards) in each segment at different times. The pressures at the left and right sides of each segment at different times are also displayed.

Over the next two sections, equations are developed which describe the relationships between the pressures at different positions in the duct.

3.2.3 Plane Wave Scattering at a Junction between Segments

Figure 3-8 shows an arbitrary junction (between the *j*th and *(j+1)*th segments) of the tubular object of Figure 3-6. As was discussed in Section 3.2.1, the pressure and volume velocity across the boundary between two cylindrical segments must be continuous. Therefore

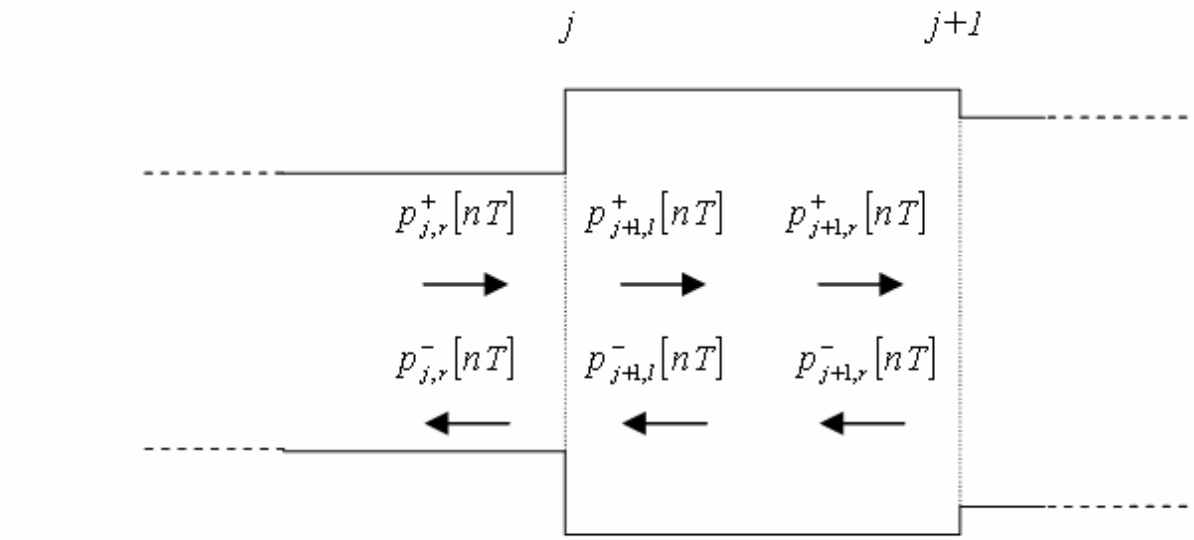

Figure 3-8: The jth and (j+1)th cylindrical segments

$$p^{+}_{j,r}[nT] + p^{-}_{j,r}[nT] = p^{+}_{j+1,l}[nT] + p^{-}_{j+1,l}[nT] \tag{3.9}$$

$$\frac{p^{+}_{j,r}[nT]}{Z_{cj}} - \frac{p^{-}_{j,r}[nT]}{Z_{cj}} = \frac{p^{+}_{j+1,l}[nT]}{Z_{c(j+1)}} - \frac{p^{-}_{j+1,l}[nT]}{Z_{c(j+1)}} \tag{3.10}$$

where $Z_{cj} = \frac{\rho c}{S_j}$ and $Z_{c(j+1)} = \frac{\rho c}{S_{j+1}}$ are the characteristic impedances of jth and $(j+1)^{\text{th}}$ cylindrical segments respectively.

Equations (3.9) and (3.10) can be rearranged to give the following matrix expression which relates the pressures on either side of the boundary to the cross-sectional areas of the two cylindrical segments. A matrix expression of this type, which relates properties either side of a junction, is often referred to as a scattering equation.

$$\begin{bmatrix} p^{+}_{j,r}[nT] \\ p^{-}_{j,r}[nT] \end{bmatrix} = \begin{bmatrix} \frac{S_j + S_{j+1}}{2S_i} & \frac{S_j - S_{j+1}}{2S_i} \\ \frac{S_j - S_{j+1}}{2S_j} & \frac{S_j + S_{j+1}}{2S_j} \end{bmatrix} \times \begin{bmatrix} p^{+}_{j+1,l}[nT] \\ p^{-}_{j+1,l}[nT] \end{bmatrix} \tag{3.11}$$

From Equation 3.7, the reflection coefficient for the junction between the jth and $(j+1)$th cylindrical segments can be written:

$$r_{j,j+1} = \frac{S_j - S_{j+1}}{S_j + S_{j+1}} \tag{3.12}$$

By combining Equations (3.11) and (3.12), the scattering equation can also be expressed in terms of the reflection coefficient:

$$\begin{bmatrix} p^{+}_{j,r}[nT] \\ p^{-}_{j,r}[nT] \end{bmatrix} = \frac{1}{1+r_{j,j+1}} \times \begin{bmatrix} 1 & r_{j,j+1} \\ r_{j,j+1} & 1 \end{bmatrix} \times \begin{bmatrix} p^{+}_{j+1,r}[nT] \\ p^{-}_{j+1,r}[nT] \end{bmatrix} \tag{3.13}$$

3.2.4 Plane Wave Propagation through a Cylindrical Segment

So far it has been assumed that sound propagation is lossless. In fact, viscous losses and heat conduction losses are significant when sound waves propagate within ducts of the diameters and lengths used in this project.

In order to take into account the effects of such losses, the following matrix expression can be used to relate the forward and backward traveling waves ($p^{+}_{j+1,l}[nT]$ and $p^{-}_{j+1,l}[nT]$) at the left side of the *(j+1)*th cylindrical segment to the forward and backward traveling waves ($p^{+}_{j+1,r}[nT]$ and $p^{-}_{j+1,r}[nT]$) at the right side of the segment.

$$\begin{bmatrix} p^{+}_{j+1,l}[nT] \\ p^{-}_{j+1,l}[nT] \end{bmatrix} = \begin{bmatrix} e^{\Gamma L} & 0 \\ 0 & e^{-\Gamma L} \end{bmatrix} \begin{bmatrix} p^{+}_{j+1,r}[nT] \\ p^{-}_{j+1,r}[nT] \end{bmatrix} \tag{3.14}$$

where the term $e^{-\Gamma L}$ represents the delay of $T/2$ experienced by an acoustic wave when propagating through a segment of length L and also the attenuation experienced by the wave. For a cylinder of radius r and length L, an expression for the complex wave number Γ is given by Keefe [27]:

$$\Gamma = \alpha(\omega) + \frac{i\omega}{v_p} \tag{3.15}$$

where $\alpha(\omega)$ is the frequency dependent attenuation due to boundary layer effects, ω is the angular frequency and v_p is the phase velocity. These parameters can be written as:

$$\alpha(\omega) = \frac{\omega}{c}\left(Ar_v^{-1} + Br_v^{-2} + Cr_v^{-3}\right) \tag{3.16}$$

$$\frac{\omega}{v_p} = \frac{\omega}{c}\left(1 + Ar_v^{-1} - Cr_v^{-3}\right) \tag{3.17}$$

where $r_v = \left(\frac{\omega p}{\eta}\right)^{\frac{1}{2}} r$, is the ratio of the duct radius to the viscous boundary layer, ρ is the air density and η is the coefficient of shear viscosity of air. The coefficients *A, B* and *C* depend on the thermodynamic constants:

$$A = \frac{1}{\sqrt{2}}(1 + D) \tag{3.18}$$

$$B = \left[1 + D - \frac{D}{2v} - \frac{D^2}{2}\right] \tag{3.19}$$

$$C = \frac{1}{\sqrt{2}}\left[\frac{7}{8} + D - \frac{D}{2v} - \frac{D^2}{2} - \frac{D}{8v^2} + \frac{D^2}{2v} + \frac{D^3}{2}\right] \tag{3.20}$$

where $v = \sqrt{\eta C_p / \kappa}$, $D = (\gamma - 1)/v$, C_p is the specific heat of air at constant pressure, κ is the thermal conductivity of air, γ is the ratio of the principal specific heats of air,

$c = 331.6\sqrt{1+\tau/273}$ is the speed of sound in air in m s^{-1} and τ is the air temperature in Kelvin.

The complex wave number, Γ, given in Equation (3.15) is related to the complex propagation constant, $\underline{k}$, described in Section 2.4.1 by a factor of *-j*, that is $\underline{k} = -j\Gamma$. It should be noted that the expressions for α in both the complex wave number, Equation (3.16), and the propagation constant, Equation (2.25), are the same if the higher order terms, $Br_v^{-2} + Cr_v^{-3}$, are ignored in the complex wave number. In fact, the expression for α used by Kinsler, introduced in Section 2.4.1, is an approximation of the expression used by Keefe described in this section. For large values of the hole radius, *r*, the sum of the high order terms, $Br_v^{-2} + Cr_v^{-3}$, is significantly smaller than the first term enabling the higher order terms to be ignored in the analytical calculations for the leak size with no significant loss of accuracy. For example a 2mm hole radius results in Ar_v^{-1} values of 1.68014×10^{-5} and 1.68014×10^{-6} for the frequency points of 200 Hz and 2000 Hz. The value of $Br_v^{-2} + Cr_v^{-3}$ is 3.98026×10^{-11} and 3.98026×10^{-13} for the frequency points of 200 Hz and 2000 Hz respectively.

Similarly, the phase velocity approaches the speed of sound for large values of the hole radius *r*. Therefore, in the expression for the propagation constant described in Section 2.4.1, Equation (2.24), the speed of sound is used as an approximation of the phase velocity. Again using the approach described above, the value of $Ar_v^{-1} - Cr_v^{-3}$ in Equation (3.17) is significantly less than unity for large values of *r* enabling the term to be ignored in the analytical calculations for the leak size. Indeed using the same example of a 2mm hole radius, the value of $Ar_v^{-1} - Cr_v^{-3}$ is 5.84693×10^{-6} and 35.84693×10^{-7} for the

frequency points of 200 Hz and 2000 Hz. When the term $Ar_v^{-1} - Cr_v^{-3}$ is significantly less than unity, $\frac{\omega}{v_p} \approx \frac{\omega}{c}$ and hence, $v_p \approx c$, as can be seen from Equation (3.17).

3.2.5 Plane Wave Propagation through Multiple Segments

By combining Equations (3.13) and (3.14), a single matrix equation describing plane wave propagation from one cylindrical segment to the next can be derived. The equation describes the pressure waves on the right side of the *j*th segment in terms of those on the right side of the *(j+1)*th segment.

$$\begin{bmatrix} P_{j,r}^{+}\left[e^{j\theta}\right] \\ P_{j,r}^{-}\left[e^{j\theta}\right] \end{bmatrix} = M_j \begin{bmatrix} P_{j+1,r}^{+}\left[e^{j\theta}\right] \\ P_{j+1,r}^{-}\left[e^{j\theta}\right] \end{bmatrix} \tag{3.21}$$

where θ is the discretised frequency and

$$M_j = \frac{1}{1+r_{j,j+1}} \begin{bmatrix} 1 & r_{j,j+1} \\ r_{j,j+1} & 1 \end{bmatrix} \begin{bmatrix} e^{\Gamma L} & 0 \\ 0 & e^{-\Gamma L} \end{bmatrix} \tag{3.22}$$

For a duct like that of Figure 3-6, which is modeled as *N* cylindrical segments and is coupled at the left end to a semi-infinite tube (the 'zeroth' segment), each of the segments has a matrix of the same form as Equation (3.22). The forward and backward travelling waves at the junction between the semi-infinite tube and the first segment can be expressed in terms of those in the final *Nth* segment through the multiple application of Equation (3.21)

$$\begin{bmatrix} P_{0,r}^{+}\left[e^{j\theta}\right] \\ P_{0,r}^{-}\left[e^{j\theta}\right] \end{bmatrix} = M_0 M_1 M_2 \cdots\cdots M_{n-1} \begin{bmatrix} P_{N,r}^{+}\left[e^{j\theta}\right] \\ P_{N,r}^{-}\left[e^{j\theta}\right] \end{bmatrix} = \begin{bmatrix} M_{aa} & M_{ab} \\ M_{ba} & M_{bb} \end{bmatrix} \begin{bmatrix} P_{n,r}^{+}[e^{j\theta}] \\ P_{n,r}^{-}[e^{j\theta}] \end{bmatrix} \tag{3.23}$$

In the frequency domain, the ratio of the backward traveling waves and the forward travelling waves at the entry of the duct is defined as the reflectance $IIR(e^{j\theta})$. The reflectance of the duct is therefore

$$IIR\left(e^{j\theta}\right) = \frac{M_{ba} + M_{bb}\dfrac{P_{N,r}^{-}\left[e^{j\theta}\right]}{P_{N,r}^{+}\left[e^{j\theta}\right]}}{M_{aa} + M_{ab}\dfrac{P_{N,r}^{-}\left[e^{j\theta}\right]}{P_{N,r}^{+}\left[e^{j\theta}\right]}} \tag{3.24}$$

Providing that the dimensions of the duct (and hence the elements of matrix *M*) are known, the reflectance can be determined from the ratio of the forward and backward travelling waves at the right end of the duct. This ratio depends on how the duct is terminated at the far end and can be expressed in terms of the load impedance Z_L at the end of the duct

$$\frac{P_{n,r}^{-}\left[e^{j\theta}\right]}{P_{n,r}^{+}\left[e^{j\theta}\right]} = \frac{Z_L / Z_N - 1}{Z_L / Z_N + 1} \tag{3.25}$$

where Z_N is the characteristic impedance of the N^{th} cylindrical segment.

For example, if the duct terminates in an unflanged open end, the load impedance is

$$Z_L = Z_N\left[\frac{1}{4}(kr)^2 + j0.6kr\right] \tag{3.26}$$

So, by combining (3.24), (3.25) and (3.26), the reflectance of the duct is

$$IIR\left(e^{j\theta}\right)=\frac{M_{ba}+M_{bb}\dfrac{\left[\frac{1}{4}(kr)^2-1+j0.6kr\right]}{\left[\frac{1}{4}(kr)^2+1+j0.6kr\right]}}{M_{aa}+M_{ab}\dfrac{\left[\frac{1}{4}(kr)^2-1+j0.6kr\right]}{\left[\frac{1}{4}(kr)^2+1+j0.6kr\right]}} \tag{3.27}$$

The reflectance is simply the frequency domain description of the input impulse response. Therefore, by inverse Fourier transforming the reflectance the input impulse response of the duct *iir[nT]* can be obtained.

3.3 Bore Reconstruction – The Inverse Problem

In Section 3.2, equations were described that enable the input impulse response of a duct to be calculated from its measured geometry. In order to carry out a bore reconstruction, it is necessary to solve the inverse problem of calculating the duct's geometry from a reflectometry measurement of its input impulse response.

3.3.1 Layer-Peeling Algorithm

In 1995, Amir, Rosenhouse and Shimony [38] developed a layer-peeling algorithm which calculates the radial dimensions of a duct from its input impulse response. The algorithm compensates for the attenuation experienced by the acoustic waves whilst propagating within the duct.

Consider again the duct model of Figure 3-6. An incident wave injected into the duct via the 'zeroth segment' (the semi-infinite tube) will experience partial reflection and partial transmission at each segment boundary within the duct. The wave propagation in the zeroth and first segments in such a case is shown in Figure 3-9.

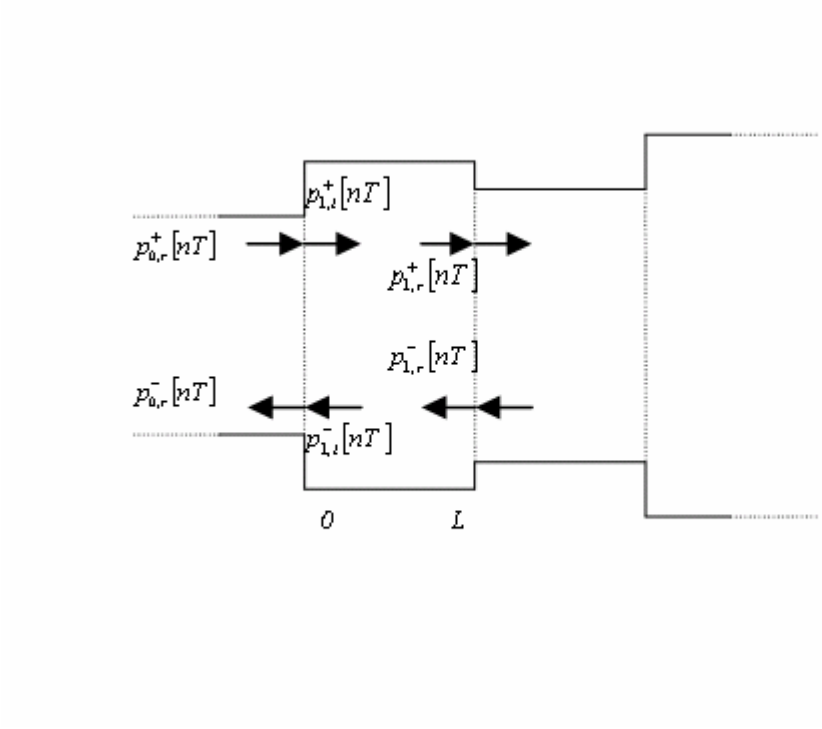

Figure 3-9: Forward and backward travelling waves in a duct

When the wave injected into the duct is an acoustic impulse ($p^+_{0,r}[nT] = \delta[nT]$) then the reflected wave is the input impulse response ($p^+_{0,r}[nT] = iir[nT]$). At time t =0 (defined as being the instant that the incident wave arrives at the entrance to the duct boundary between the zeroth and first segments), there are no backward travelling waves in the first cylindrical segment. That is, $p^-_{1,l}[nT]$ and $p^-_{1,r}[nT]$are both zero. Consequently, the backward travelling wave in the zeroth segment is simply the reflection of the forward

traveling wave in that segment. The reflection coefficient at the boundary between the segment 0 and segment 1 is therefore:

$$r_{0,1} = \frac{p^{-}_{0,r}[0T]}{p^{+}_{0,r}[0T]} = iir[0T] \tag{3.28}$$

where $p^{-}_{0,r}[0T]$ and $p^{+}_{0,r}[0T]$ are the incident and reflected waves and $iir[0T]$ is the input impulse response, all at $t = 0$.

In Equation (3.12), the reflection coefficient for the boundary between two arbitrary segments (the jth and the *(j+1)*th) was expressed in terms of the cross-sectional areas of those segments. Rearranging Equation (3.12) therefore allows the cross-sectional area of the $(j+1)$th segment to be expressed in terms of the area of the jth segment and the reflection coefficient $r_{j,j+1}$:

$$S_{j+1} = S_j \left(\frac{1 - r_{j,j+1}}{1 + r_{j,j+1}} \right) \tag{3.29}$$

Therefore, assuming that the cross-sectional area S_0 of the zeroth segment (the semi-infinite cylinder) is known, the area S_1 of the first segment can be found from the reflection coefficient $r_{0,1}$ using Equation (3.29). Assuming cylindrical symmetry, the radius of the segment can also be determined.

The forward and backward travelling pressure waves $p^{+}_{1,l}[nT]$ and $p^{-}_{1,l}[nT]$ at the left side of the first segment, can be obtained from the forward and backward waves in the zeroth segment by rearranging Equation (3.13), to give:

$$\begin{bmatrix} p_{1,l}^{+}[nT] \\ p_{1,l}^{-}[nT] \end{bmatrix} = \frac{1}{1+r_{0,1}} \times \begin{bmatrix} 1 & r_{0,1} \\ r_{0,1} & 1 \end{bmatrix} \times \begin{bmatrix} p_{0,r}^{+}[nT] \\ p_{0,r}^{-}[nT] \end{bmatrix} \tag{3.30}$$

Next the pressure waves at the right side of the first segment must be found. To determine the forward and backward travelling pressure waves $p_{1,r}^{+}[nT]$ and $p_{1,r}^{-}[nT]$, at the right side

of the first segment, a delay of *T/2* is added to $p_{1,l}^{+}[nT]$ and subtracted from $p_{1,l}^{-}[nT]$. In addition, a digital filter representing the losses in a cylindrical segment is applied. This filter depends on the radius of the segment.

Referring back to Equations (3.14) and (3.15), the continuous frequency domain lossy filter for waves propagating through a cylindrical segment is given by

$$H(\omega) = e^{-\Gamma l} = e^{-\alpha(\omega)l} e^{-j\omega l / v_p} \tag{3.31}$$

The numerical computation of the equivalent digital frequency domain lossy filter is detailed in [38, 39]. By inverse Fourier Transforming the discretized lossy filter, the digital filter $h_j[nT]$ is found.

Moving from the left side to the right side of a cylindrical segment, the forward travelling wave $p_{j,l}^{+}[nT]$is simply passed through the filter $h_j[nT]$. Meanwhile the backward traveling wave $p_{j,l}^{-}[nT]$is passed through the inverse filter of $h_j[nT]$.

$$p_{j,l}^{+}[nT] = p_{j,l}^{+}[nT] \otimes h_j[nT] \tag{3.32}$$

$$p_{j,l}^{-}[nT] = p_{j,l}^{-}[nT] \otimes^{-1} h_j[nT] \tag{3.33}$$

where the operators $\otimes$ and $\otimes^{-1}$ represent convolution and deconvolution, and $h_j[nT]$ is the digital lossy filter in the *j*th segment.

At the boundary between the first and second segments, when $t = T/2$, there is no backward travelling wave in the second segment. Therefore, the reflection coefficient at the junction between the first and second cylindrical segments is given by:

$$r_{1,2} = \frac{p_1^-[T/2]}{P_1^+[T/2]} \tag{3.34}$$

It should be noted that, when implementing the algorithm in practice, it is more convenient and entirely equivalent to subtract a delay of T from $p_{1,l}^-[nT]$ and leave $p_{1,l}^+[nT]$ unchanged. The time origin shift then requires the reflection coefficient $r_{1,2}$ to be calculated at $t = 0$ rather than at $t = T/2$.

Again, using Equation (3.29), the cross-sectional area S_2 can be obtained from the previously calculated cross-sectional area S_1 and the reflection coefficient $r_{1,2}$. The layer peeling procedure is carried out recursively until the reflection coefficient at each junction is determined and the entire area profile of the duct is calculated.

3.3.2 Experimental Results

Figure 3-10 shows a bore reconstruction of the stepped tube described in Section 3.1.2 (comprising cylindrical sections of radius 5.9 mm and 3.85 mm respectively). The reconstruction was calculated by applying the layer peeling algorithm to the measured

input impulse response of Figure 3-4. It can be seen that the cylindrical sections of radius 5.9 mm and 3.85 mm are reconstructed with reasonable accuracy.

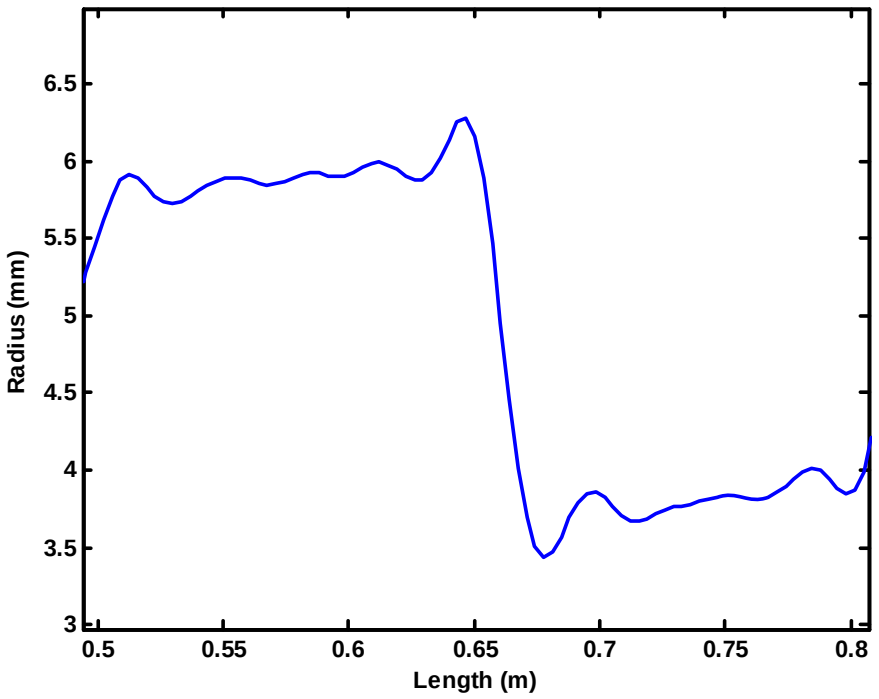

Figure 3-10: Bore reconstruction of stepped tube

3.4 Input Impedance

It is possible to calculate the complex input impedance of a tubular object from its input impulse response [2, 8, 9]. The equations for calculating the input impedance can be derived by describing the pressure and velocity at the object's input in terms of the excitation impulse and the input impulse response:

$$p_{0,r}[nT] = \delta[nT] + iir[nT] \tag{3.35}$$

$$Z_0 \times U_{0,r}[nT] = \delta[nT] - iir[nT] \tag{3.36}$$

where $p_{0,r}[nT]$ is the total pressure at the input to the tubular object at time nT, $U_{0,r}[nT]$ is the volume velocity at the object's input at time nT and $iir[nT]$ is the input impulse response of the object.

Equation (3.35) and (3.36) can be written in the frequency domain as

$$P_{0,r}[e^{j\theta}] = 1 + IIR[e^{j\theta}] \tag{3.37}$$

$$Z_0 \times U_{0,r}[e^{j\theta}] = 1 - IIR[e^{j\theta}] \tag{3.38}$$

where $P_{0,r}[e^{j\theta}]$ is the FFT of $p_{0,r}[nT]$, $U_{0,r}[e^{j\theta}]$ is the FFT of $U_{0,r}[nT]$ and $IIR[e^{j\theta}]$ is the FFT of $iir[nT]$.

The input impedance of a tubular object is defined as pressure divided by volume velocity. Using this definition, Equations (3.37) and (3.38) can be combined to express the input impedance in terms of the input impulse response:

$$Z_{in}[e^{j\theta}] = \frac{P_{0,r}[e^{j\theta}]}{U_{0,r}[e^{j\theta}]} = Z_0 \times \frac{1 + IIR[e^{j\theta}]}{1 - IIR[e^{j\theta}]} \tag{3.39}$$

Using Equation (3.39), the experimental value of input impedance of the stepped tube described in Section 3.1.2 was calculated from the input impulse response of Figure 3-4. The plot of the input impedance is shown in Figure 3-11 below.

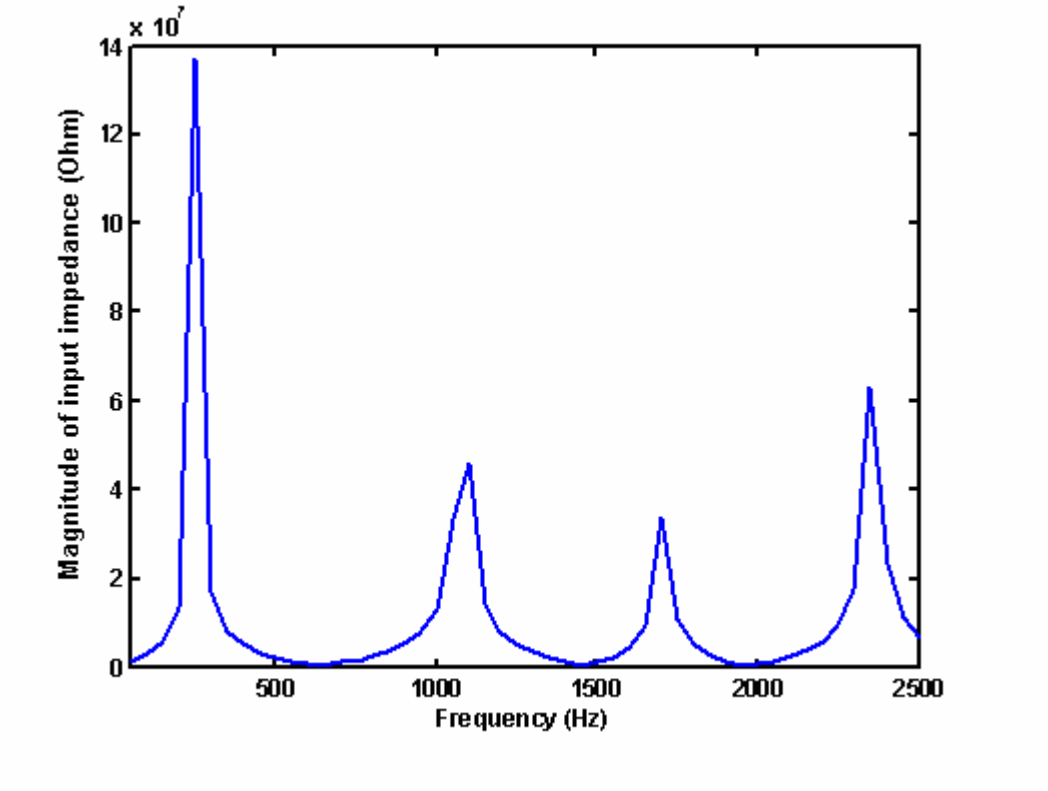

Figure 3-11: Magnitude of the input impedance of a stepped tube

Chapter 4

Investigating a Single Leak in a Cylindrical Duct using Analytical Methods

In this chapter, a method for predicting the radius of a single leak in the side wall of a cylindrical object is discussed. This method was proposed by Sharp [1]. The basic procedure involves experimentally determining the input impedance of the tube under investigation by means of the pulse reflectometry method discussed in Chapter 3. By inverting the theoretical expression for the input impedance of a cylindrical tube with a side hole presented in Chapter 2, the impedance of the leak in the tube can be calculated assuming the geometry of the tube is known. Appropriate theories presented in this chapter can then be used to predict the size of the leak in the side wall of the cylindrical tube from the calculated impedance of the hole.

Leak radius predictions are presented for holes of various sizes drilled in the side walls of two different cylindrical pipes. The first cylindrical pipe, with a slightly thicker wall, had holes of larger radius drilled in the side wall. Meanwhile, the second cylindrical pipe had a thinner wall enabling smaller holes to be drilled in the side wall.

The method for predicting the size of the leak requires that the position of the leak is known. Thus, the chapter begins with a description of the detection and location of a single leak in the side wall of a cylindrical pipe using the technique of acoustic pulse reflectometry.

4.1 Locating the Position of a Leak

Using the technique of pulse reflectometry discussed in Chapter 3, it is possible to detect the presence of a leak in cylindrical duct and find its location by examining the resulting bore reconstruction.

Being able to use the technique of pulse reflectometry for locating the position of a leak arises from the fact that a small leak in the cylindrical tube behaves as a side branch of complex impedance. From [30], the side branch is known to cause a reduction in the magnitude of the impedance experienced by the pulse travelling in a duct. When the pulse encounters this reduction in impedance, it is partially reflected (in a similar manner to the partial reflection at a widening of the bore). As a result, when the reflections from a duct containing a leak are used to calculate the input impulse response and then fed into the layer peeling algorithm, an expansion occurs in the bore reconstruction at the position of the leak.

Therefore, when reflections from a pulse travelling within a duct containing a leak in the side wall are fed into a reconstruction algorithm, the calculated bore profile should be correct up to the position of the leak. Thereafter, there will be an expansion in the bore reconstruction whose extent will depend on the size of the leak.

Using acoustic pulse reflectometry, a measurement was made of the input impulse response of a straight cylindrical pipe of length 0.508 m and wall thickness 1 mm. The pipe had a 1 mm diameter hole drilled at a distance of 0.31 m along its length. Figure 4-1 shows the bore reconstruction that results when the layer peeling algorithm is applied to the input impulse response measurement.

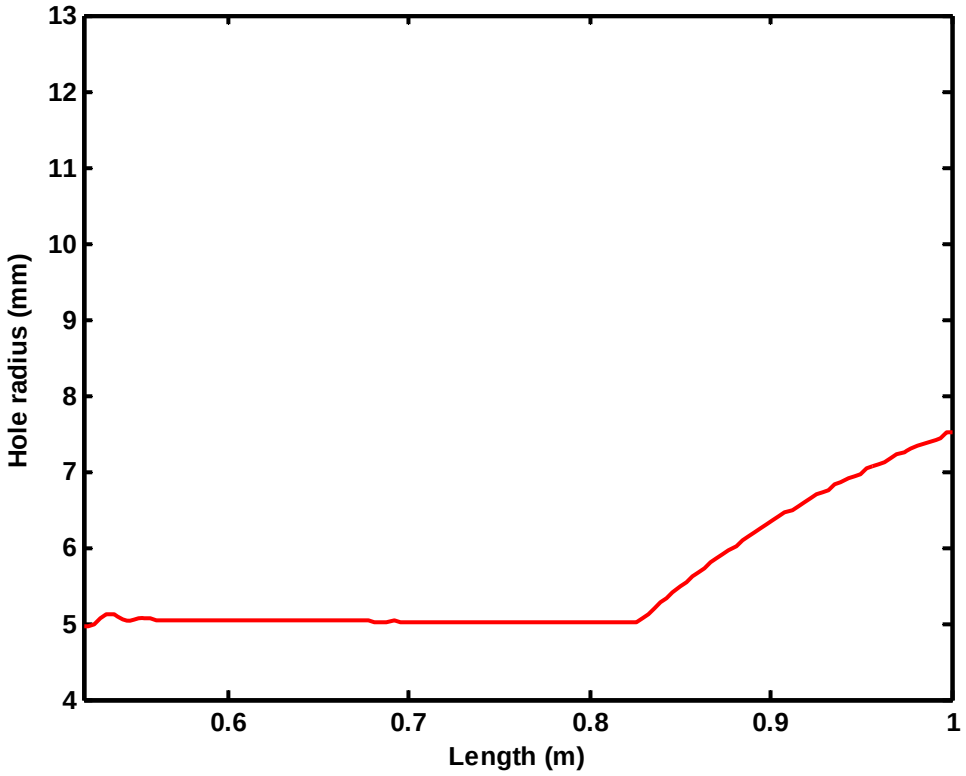

Figure 4-1: Bore reconstruction of a cylindrical pipe with a 1 mm diameter leak leak

The first part of the bore reconstruction of Figure 4-1 shows the DC tube – a cylindrical tube employed during an acoustic pulse reflectometry measurement for DC offset calibration [1]. From 0.51 m, the reconstruction shows the leaking pipe under investigation. The radius of this pipe is predicted accurately up to the position of the leak at 0.82 m on the graph. Thereafter, a spurious expansion in the reconstructed bore profile can be clearly seen. Since, the reconstruction of the leaking cylindrical pipe starts from 0.51 m, the distance to the position of the leak is simply a subtraction of the start of the pipe reconstruction from the distance to the point where the reconstruction deviates from the correct profile. In this way the location of the leak using the bore reconstruction is found to be approximately 0.31 m from the beginning of the cylindrical pipe. This is consistent with the measured location of the leak discussed earlier on.

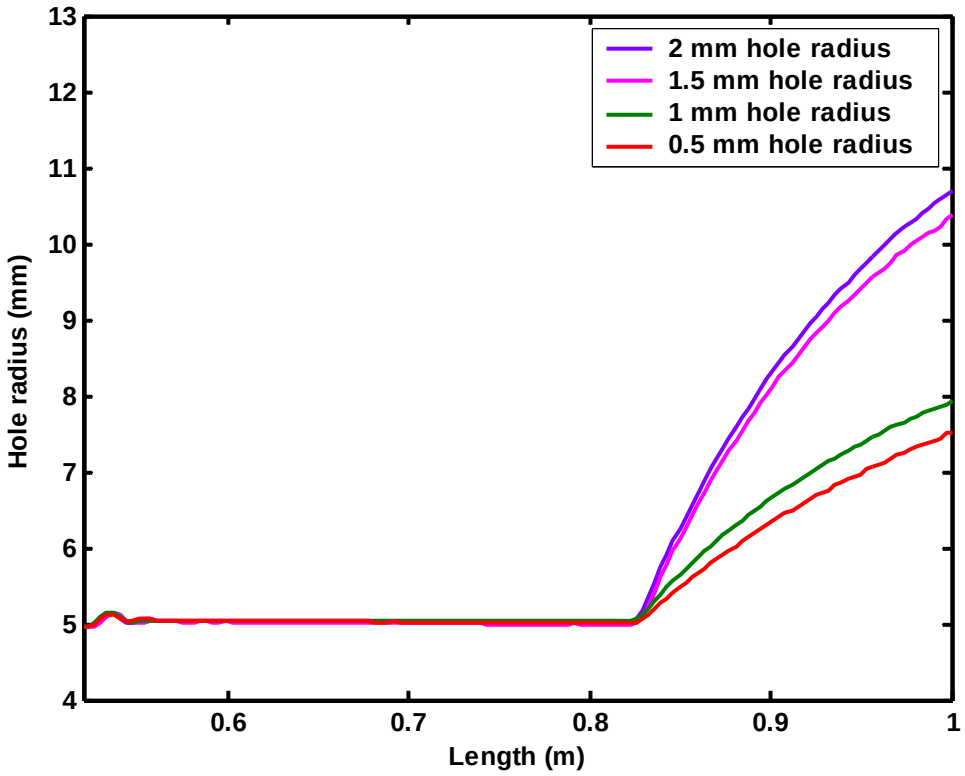

Figure 4-2: Bore reconstructions of cylindrical pipe with four different leak sizes

To further study the effect that a leak has on the bore reconstruction, three more holes of diameter 2 mm, 3 mm and 4 mm were drilled in the cylindrical pipe. The four holes were then sealed. Unsealing each hole one at a time, acoustic pulse reflectomtery measurements were made of the cylindrical pipe with a 2 mm diameter leak, with a 3 mm diameter leak and with a 4 mm diameter leak. Figure 4-2 shows the resultant bore reconstructions along with the reconstruction for the 1mm diameter leak shown previously in Figure 4-1.

It can be seen clearly that the lowest rate of expansion in the reconstruction from the position of the leak occurs for the pipe containing the 1 mm diameter leak. The greatest rate of expansion is observed in the reconstruction of the pipe containing the 4 mm diameter leak. It can therefore be concluded that the larger the hole, the greater the rate of expansion in the reconstruction. This is due to the fact that there is a greater reduction in the impedance magnitude seen by the incoming pulse.

4.2 Input Impedance of a Duct Containing a Single Leak

4.2.1 Experimental Measurements

As discussed in Chapter 3, by applying Equation 3.39 to a reflectometry measurement of the input impulse response of a duct, the input impedance can be determined.

In order to verify this approach, experimental input impedance curves were determined for the cylindrical pipe with a 1 mm, 2 mm, 3 mm and 4 mm diameter hole from the reflectometry measurements discussed in the previous section. Figure 4-3 shows the experimentally determined impedance curve for the pipe with the 1 mm diameter hole drilled in the wall.

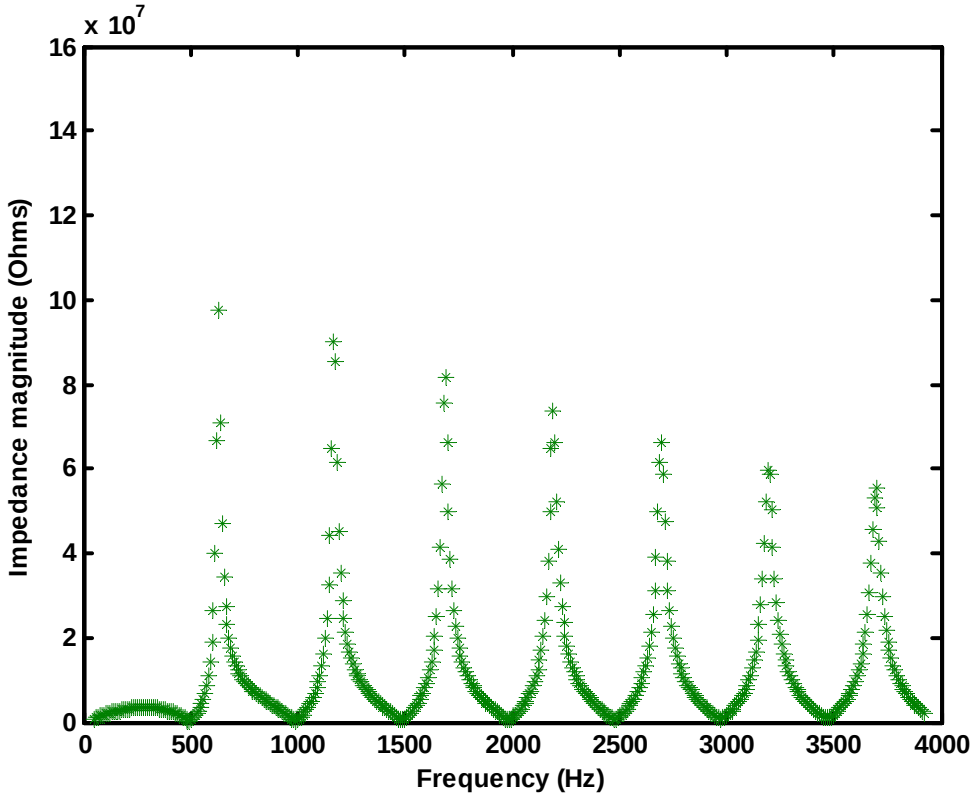

Figure 4-3: Experimental input impedance curve for cylindrical pipe with 1 mm diameter leak

4.2.2 Theoretical Impedance Curves

A theoretical expression for the complex impedance of a side hole can be derived by considering the side hole as a side branch [30]. The full expression involves Bessel functions, which makes it difficult to investigate terms such as the radius of the hole given the value of its impedance. However, for the situation where the boundary layer thickness is much smaller than the hole radius, Sharp [1, 10] used the expression for calculating the input impedance of a hole given in Equation (4.1):

$$Z_h = \frac{\rho\omega k}{4\pi} + j\frac{\rho\omega(l_h + Er_h)}{\pi r_h^2} \tag{4.1}$$

where l_h is the depth, r_h is the radius and $E = 1.595 - 0.58\left(\frac{r_h}{r}\right)^2$ is the sum of the inner and outer end corrections for a hole set flush with the cylinder wall and k is taken as the real part of the complex propagation constant. Hence, the attenuation is dependent on the hole radius r_h, not the cylinder radius r.

By substituting the theoretical expression for the impedance of a side hole (Equation 4.1) into the input impedance equations (Equations (2.29) to (2.32)) presented in Chapter 2, the theoretical input impedance of a cylindrical pipe with a single hole drilled in the wall can be calculated.

In this way, theoretical input impedance curves were calculated for the cylindrical pipe with the four different leak sizes introduced in Section 4.1. The parameters used in the model were l_1 = 0.31 m, l_2 = 0.198 m, l_h = 0.001 m and r = 0.005 m, which match the measured parameters of the actual pipe. To represent the four different leak sizes, r_h was set equal to 0.5 mm, 1 mm, 1.5 mm and 2 mm in turn. Figure 4-4 shows the theoretically calculated impedance curve for the pipe with the 1 mm diameter hole drilled in the wall.

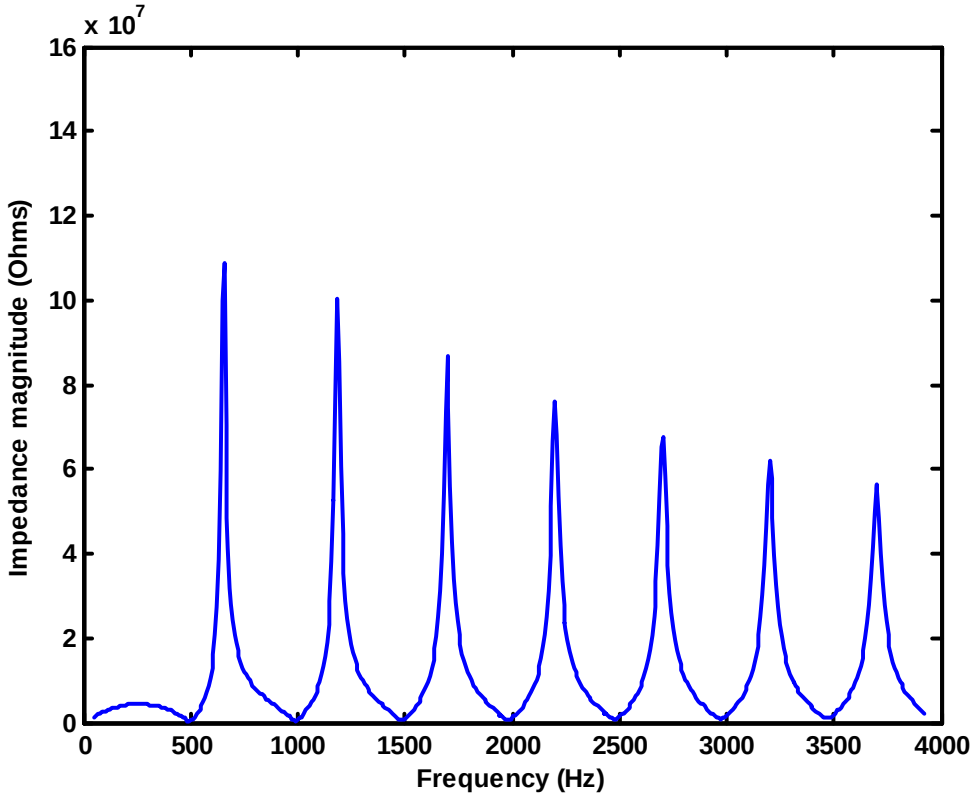

Figure 4-4: Theoretical input impedance curve for cylindrical pipe with 1 mm diameter leak

4.2.3 Comparison between the Experimental and Theoretical Impedance Curves

In order to establish the suitability of the acoustic pulse reflectometry technique for measuring input impedance, the experimental input impedance curves measured in Section 4.2.1 were compared with the theoretically determined curves of Section 4.2.2. For each leak size, a good match was found between the experimental and theoretical curves. Figure 4-5 shows one such match for the cylindrical pipe with a 1 mm leak in the side wall. The graph shows the two data sets of Figure 4-3 and Figure 4-4. It is clear that there is a good agreement between the impedance curve measured using the reflectometer and the theoretical curve.

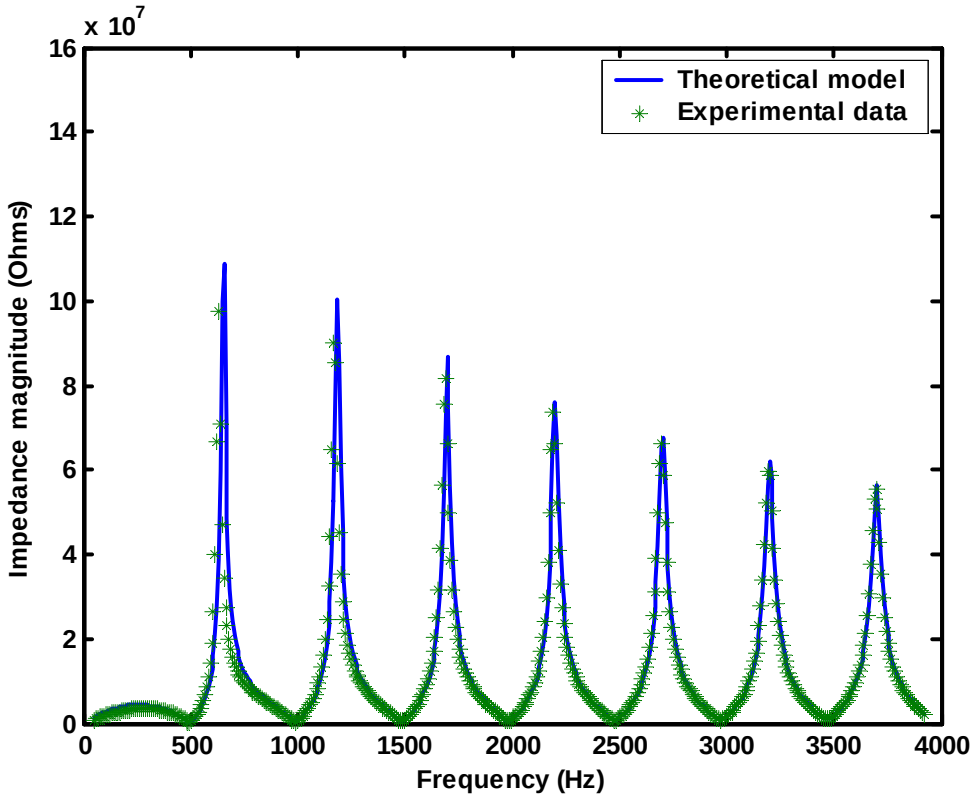

Figure 4-5: Comparison between the theoretical and experimental input impedance curves for the cylindrical pipe with a 1 mm diameter leak

4.3 Predicting the Leak Size from Experimental Measurements

4.3.1 Determining the Hole Impedance Experimentally

A theoretical expression for calculating the impedance of a hole was presented in Section 4.2.2. An alternative expression for calculating the impedance of a side hole in a duct from the duct's input impedance can be found by inverting the theoretical input impedance equations presented in Chapter 2.

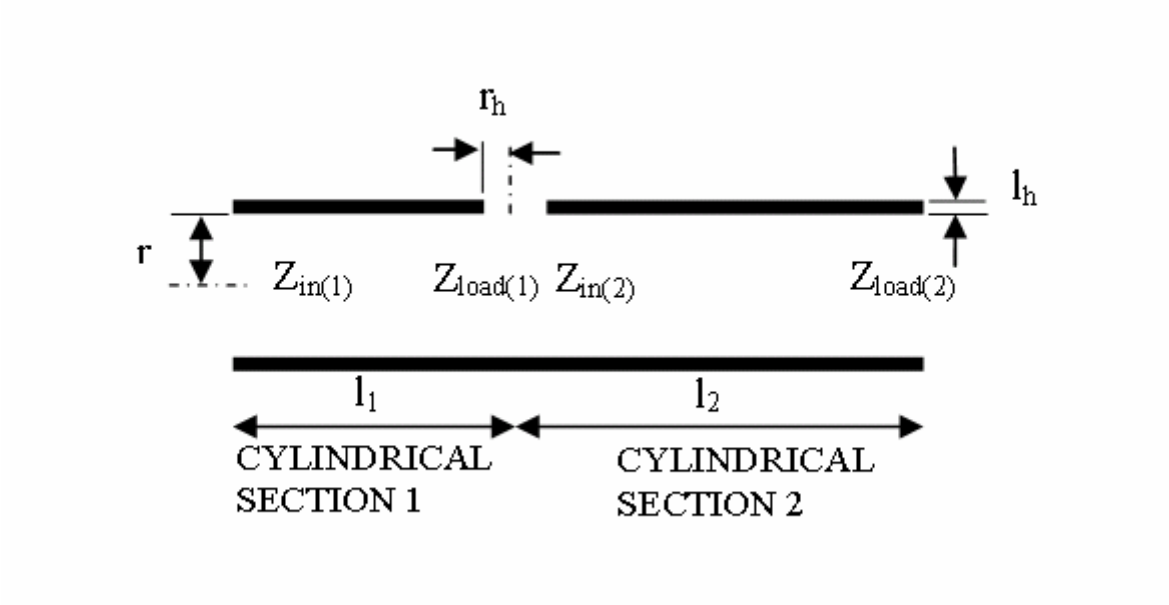

Figure 4-6: Schematic representation of cylindrical pipe 1 containing a single leak

A cylindrical pipe containing multiple leaks was shown in Figure 2-4. As an aid in illustrating the derivation of the impedance of a single hole in the wall of a cylindrical pipe, the pipe is redrawn in Figure 4-6 containing only one leak. The leaking pipe can be thought of as consisting of two non-leaking cylinders of lengths l_1 and l_2, one before the hole and one after. These are represented in Figure 4-6 as cylindrical section 1 and cylindrical section 2. From this model, an expression can be found for the impedance of the hole Z_h in terms of the input impedance of the leaking pipe $Z_{in(1)}$.

The load impedance at the end of the first cylindrical section, $Z_{load(1)}$, is made up of contributions from the input impedance of the second cylindrical section, $Z_{in(2)}$, and the impedance of the hole, Z_h. As $Z_{in(2)}$ and Z_h form a parallel acoustic circuit, the impedance of the hole can be expressed in terms of the impedances $Z_{load(1)}$ and $Z_{in(2)}$:

$$\frac{1}{Z_h} = \frac{1}{Z_{load(1)}} - \frac{1}{Z_{in(2)}} = \frac{Z_{in(2)} - Z_{load(1)}}{Z_{in(2)} Z_{load(1)}} \tag{4.2}$$

Thus

$$Z_h = \frac{Z_{load(1)} Z_{in(2)}}{Z_{in(2)} - Z_{load(1)}} \tag{4.3}$$

Equation (2.23) gives the input impedance of a non-leaking cylinder with a load impedance at its end. The first cylindrical section of length l_1 is such a cylinder, with an input impedance $Z_{in(1)}$ and a load impedance $Z_{load(1)}$. By rearranging Equation (2.23), an expression is obtained for the load impedance $Z_{load(1)}$ (i.e. the impedance at the end of the first cylindrical section) in terms of the input impedance of the leaking pipe, $Z_{in(1)}$:

$$Z_{load(1)} = \frac{Z_{in(1)} - j\frac{\rho c}{S}\tan \underline{k} l_1}{1 - j\frac{Z_{in(1)} S}{\rho c}\tan \underline{k} l_1} \tag{4.4}$$

where $\underline{k}$ is the complex propagation constant described in Section 2.4.1.

Equation (2.27) gives the input impedance of an open-ended non-leaking cylinder. The second cylindrical section of length l_2 is such a cylinder, with an input impedance $Z_{in(2)}$. Rewriting Equation (2.27) gives:

$$Z_{in(2)} = \frac{\rho c}{S}\left(\frac{0.25\underline{k}^2 r^2 + j(0.6\underline{k} r + \tan \underline{k} l_2)}{(1 - 0.6\underline{k} r + \tan \underline{k} l_2) + j0.25\underline{k}^2 r^2 \tan \underline{k} l_2} \right) \tag{4.5}$$

Substituting Equations (4.4) and (4.5) into Equation (4.3) gives the complex impedance of the hole, Z_h, in terms of the complex experimental input impedance of the leaking pipe, $Z_{in(1)}$.

Assuming that the length and radius of the pipe are known, and the axial position of the leak has been established by the method described in Section 4.1, the hole impedance can therefore be found from an experimental measurement of the input impedance of the duct.

4.3.2 Calculating Leak Size from Hole Impedance

Once the complex impedance of the side hole, Z_h, has been determined from a reflectometry measurement of the duct's input impedance, it is then possible to evaluate the radius of the hole. This is achieved by inverting the expression for the complex impedance of a side hole given in Equation (4.1).

Expanding Equation 4.1 gives:

$$Z_h = \frac{\rho\omega k}{4\pi} + j\frac{\rho\omega}{\pi r_h^2}\left(l_h + 1.595 r_h - 0.58\frac{r_h^3}{r^2}\right) \tag{4.6}$$

Considering only the imaginary part of Equation (4.6):

$$z_{himag} = \frac{\rho\omega l_h}{\pi r_h^2} + \frac{1.595\rho\omega}{\pi r_h} - \frac{0.58\rho\omega r_h}{\pi r^2} \tag{4.7}$$

Rearranging gives a cubic equation for r_h:

$$r_h^3 + \left[\frac{1.724\pi r^2 z_{himag}}{\rho\omega}\right] r_h^2 - 2.75 r^2 r_h - \left[1.724 l_h r^2\right] = 0 \tag{4.8}$$

By substituting the imaginary part of the hole impedance (determined experimentally as described previously) into Equation (4.8) and solving the cubic expression, a prediction of the hole radius is obtained.

4.3.3 Radius Prediction Results for Cylindrical Pipe 1

The method described over the past two sections was applied to the acoustic pulse reflectometry input impedance measurements of the cylindrical pipe with 1 mm, 2 mm, 3 mm and 4 mm diameter leaks. The results are shown in Figure 4-7.

Examination of Figure 4-7 reveals that for the 1 mm, 2 mm, 3 mm and 4 mm diameter holes, between 100 Hz and 2500 Hz, the hole radius predictions are generally in good agreement with the measured sizes. The divergences of the predictions at integer multiples of approximately 850 Hz are due to the hole being in the vicinity of a pressure node at these frequencies. For the 1 mm hole diameter, the predictions become very poor after the first divergence (i.e. above 850 Hz).

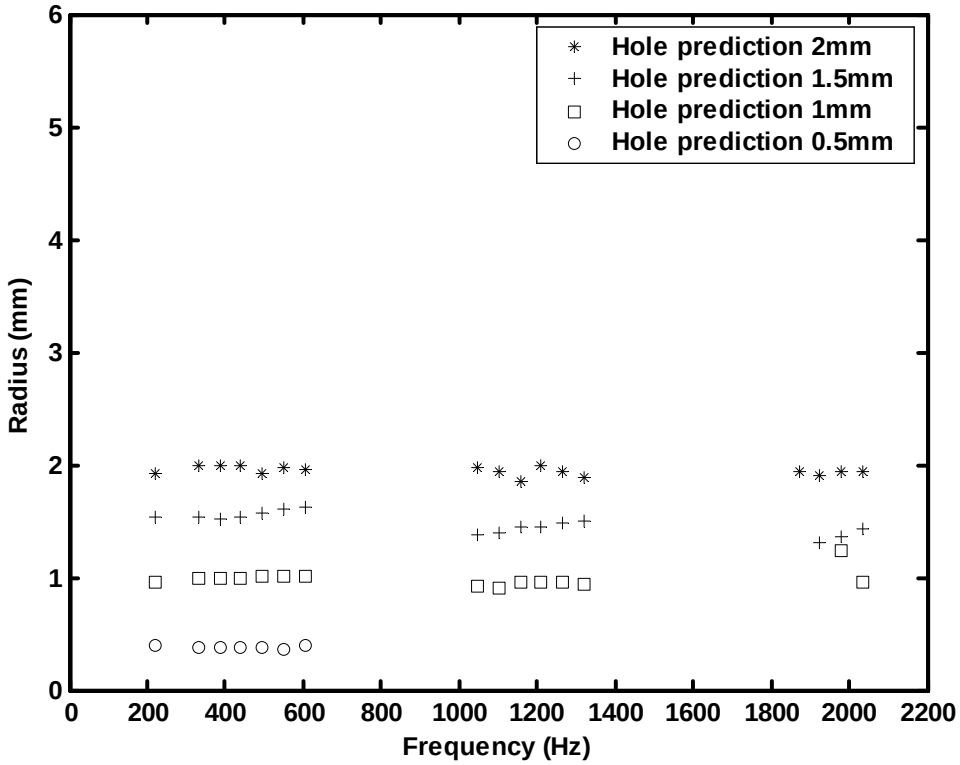

Figure 4-7: Hole size predictions for cylindrical pipe 1 containing 1 mm, 2 mm, 3 mm and 4 mm diameter leaks

The radius predictions over the frequency ranges 221-606 Hz, 1046-1321 Hz and 1871-2036 Hz were averaged and their means, variances from means and percentage differences tabulated (see Table 4-1). The radius predictions for the radii 2 mm and 1.5 mm were found to agree with the physically measured values to within 10% in all the calculated frequency ranges. The radius predictions for the 2 mm diameter hole were found to agree to within 10% up to the frequency bandwidth of 1046-1321 Hz. The agreement between the predicted and measured radii for the 1 mm diameter hole was found to be much worse in all the calculated frequency ranges. These results suggest that the proposed method is able to successfully predict the sizes of larger leaks but breaks down when the holes become smaller than 1 mm in diameter.

Frequency range (Hz)	Measured radius (mm)	Average prediction (mm)	Variance	Percentage difference (%)
221-606	2.00	1.96	0.04	2
	1.50	1.56	0.06	4
	1.00	0.99	0.01	1
	0.50	0.37	0.13	26
1046-1321	2.00	1.90	0.1	5
	1.50	1.40	0.1	6.7
	1.00	0.93	0.07	7
	0.50	33.5	33	6600
1871-2036	2.00	1.92	0.08	4
	1.50	1.36	0.14	9.3
	1.00	5.44	4.44	444
	0.50	11.5	11	2200

Table 4-1: Hole size predictions with associated accuracies for cylindrical pipe 1 containing 1 mm, 2 mm, 3 mm and 4 mm diameter leaks

4.3.4 Radius Prediction Results for Cylindrical Pipe 2

To investigate this hypothesis, a second cylindrical pipe was used. This 0.677 m long pipe was made from aluminium and had a thinner wall thickness of 0.2 mm, enabling smaller hole sizes to be drilled. The internal radius of the pipe was 7.5 mm so it was necessary to use an adapter to connect it to the source tube. The adapter had a radius r_a = 5 mm and a length l_a = 0.013 m. Figure 4-8 shows a schematic diagram of the second cylindrical pipe with the adapter at the input.

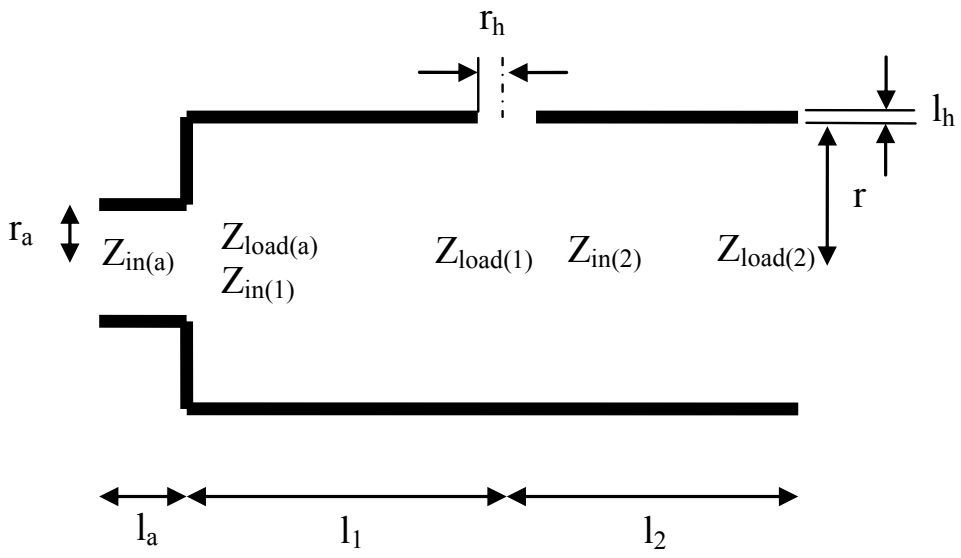

Figure 4-8: Schematic representation of cylindrical pipe 2 with a single leak and input adapter

Two holes, of 0.2 mm and 0.3 mm diameter, were drilled at a distance l_1 = 0.3695 m from the pipe input. The two holes were sealed then, unsealing each in turn, two acoustic pulse reflectometry measurements were made to find the input impulse responses (and consequently the input impedances) of the adapter/pipe combination with a 0.2 mm and a 0.3 mm diameter side hole. Figure 4-9 shows the experimentally measured input impedance curve for the adapter/pipe combination with 0.3 mm diameter side hole.

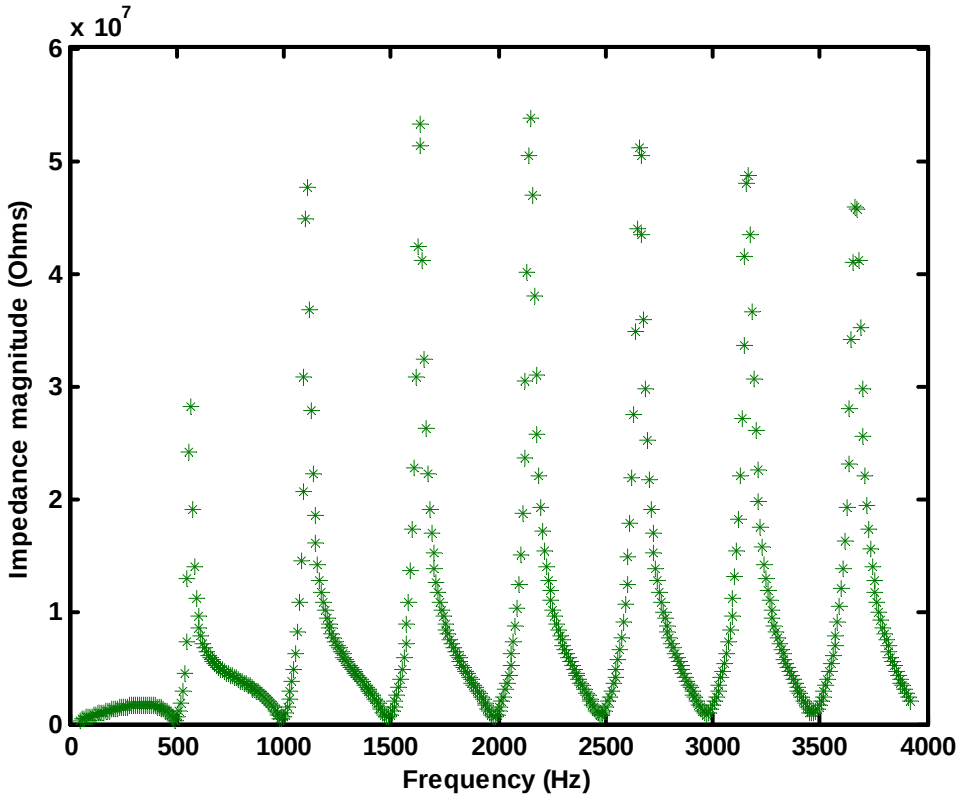

Figure 4-9: Experimentally measured input impedance for adapter/pipe combination with 0.3 mm diameter side hole

In order to make radius predictions it is first necessary to determine the input impedance of the cylindrical pipe alone (i.e. to remove the effect of the presence of the adapter). Noting that the input impedance of the cylindrical pipe is equal to the load impedance of the adapter, in a similar manner to that shown in Equation (4.4) it is possible to express the input impedance of the cylindrical pipe in terms of the input impedance of the adapter/pipe combination:

$$Z_{in(1)} = Z_{load(a)} = \frac{Z_{in(a)} - j\frac{\rho c}{S}\tan \underline{k}l_a}{1 - j\frac{Z_{in(a)}S}{\rho c}\tan \underline{k}l_a} \tag{4.9}$$

Using Equation (4.9), the input impedances of the second cylindrical pipe with side holes of 0.2 mm and 0.3 mm diameter were determined from the experimental measurements of the adapter/pipe combinations. The procedures outlined in Sections 4.3.1 and 4.3.2 were then applied to these input impedances to give predictions of the radii of the two holes. The results can be seen in Figure 4-10.

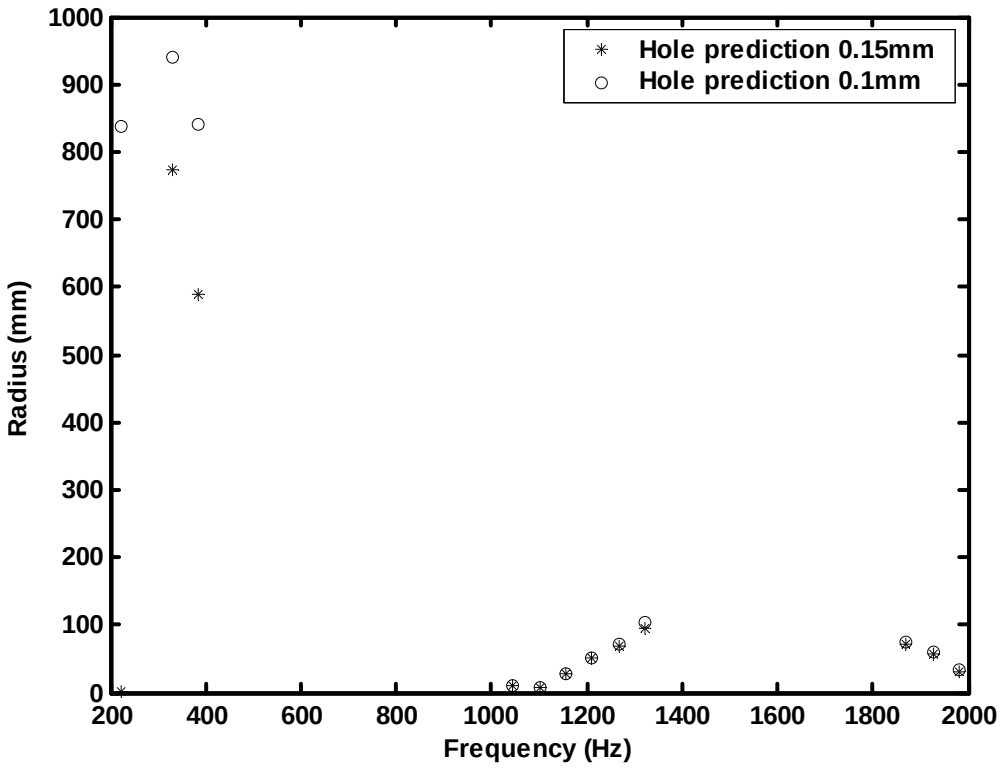

Figure 4-10: Hole size predictions for cylindrical pipe 2 containing 0.2 mm and 0.3 mm diameter leaks

Examination of Figure 4-10 shows that there is a breakdown in the radius predictions for the 0.2 mm and 0.3 mm diameter holes. This further confirms the trend that was observed

in Figure 4-7 and Table 4-1 that the method gives poor predictions of the sizes of smaller holes.

4.4 Extending Theory to Small Radius Holes

The theory on which the hole size prediction method described in Section 4.3 was based assumed that the boundary layer thickness was much smaller than the hole under investigation. For smaller holes, this assumption becomes increasingly invalid. In this section, an adaptation of the theory is presented in which it is assumed that the boundary layer thickness is comparable to the size of the hole under test. Using this adapted theory, the hole size prediction method is again tested on smaller radius holes and the results are presented.

4.4.1 Hole Impedance Theory for Small Holes

In a paper of 1975, Backus [34] took the full expression for the complex impedance of a side hole in a cylindrical pipe and, by assuming that the boundary layer thickness was comparable to the hole radius, produced a simplified equation for smaller holes. In this simplified expression, the Bessel functions of the full expression are approximated by a truncated power series.

Backus developed his theory by expressing the input impedance of the hole as:

$$Z_h = Z_c \sinh(\Gamma l_h) \tag{4.11}$$

where Z_c is the characteristic impedance, Γ is the propagation constant and l_h is the length of the hole.

For a sufficiently short hole, the product of the propagation constant and the hole length is much less than unity and the hyperbolic sine may be eliminated. In such cases, Backus gave the expression for the hole impedance as:

$$Z_h = Z_s \times l_h \tag{4.11}$$

where Z_s is the series impedance. Backus provided simplified equations for calculating the series impedance which eliminated the use of Bessel functions. The simplified expression for calculating Z_s was given as:

$$Z_s = \frac{8\eta}{\pi r_h^{\,4}} + \left(\frac{3}{4} j\omega \frac{\rho}{\pi r_h^{\,2}} \right) \tag{4.12}$$

By substituting Equation (4.12) into Equation (4.11), the hole impedance can be calculated as follows:

$$Z_h = \frac{8\eta}{\pi r_h^{\,4}} + \left(\frac{3}{4} j\omega \frac{\rho}{\pi r_h^{\,2}} \right) \times l_h \tag{4.13}$$

4.4.2 Radius Prediction Results for Cylindrical Pipe 1

In order to investigate the effectiveness of the adapted small radius theory, the methodology outlined in Section 4.3.1 was again applied to the experimental measurements of the input impedance of the first cylindrical pipe with 1 mm, 2 mm, 3 mm and 4 mm diameter leaks. In this way, the impedances of the four different side holes were established. However, rather than applying Equation (4.8) to obtain predictions of the hole radii, the following rearranged version of Equation (4.11) was used:

$$r_h = \sqrt{\frac{3\rho\omega l_h}{4\pi Z_{himag}}} \tag{4.14}$$

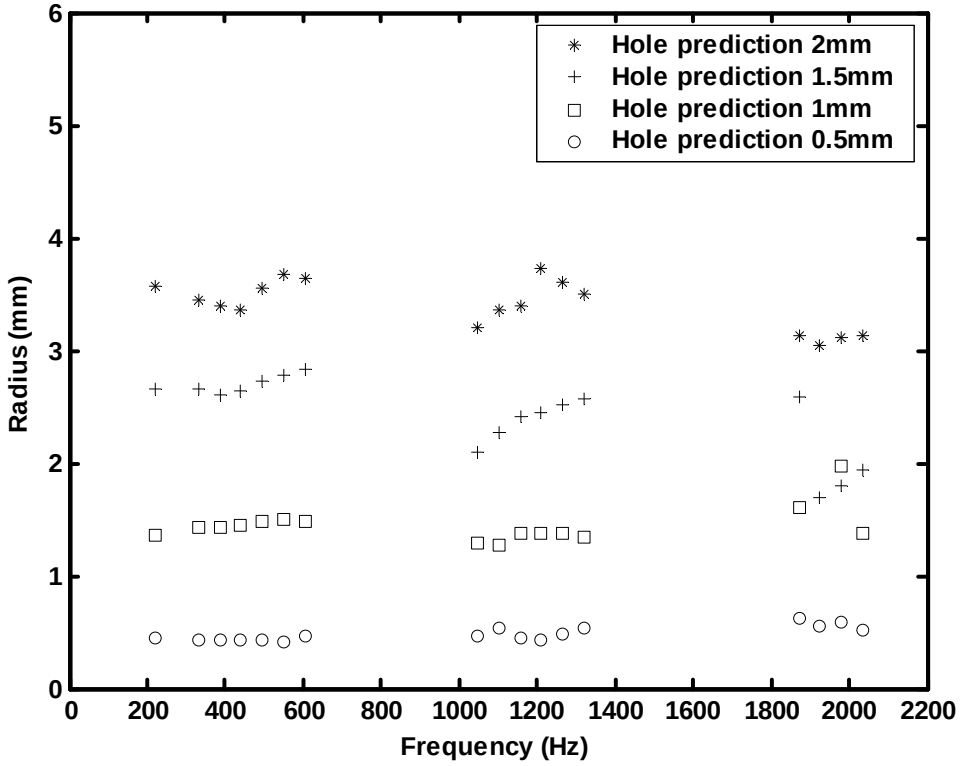

Figure 4-11: Hole size predictions for cylindrical pipe 1 containing 1 mm, 2 mm, 3 mm and 4 mm diameter leaks using the adapted small radius theory

Figure 4-11 compares the predictions of the hole radii with their actual values. It is clear that for the 1 mm diameter hole, the predicted value for the radius is generally in good agreement with the actual value over all the frequencies tested. For the 2 mm, 3 mm and 4 mm hole diameters, however, the predictions become steadily worse.

The radius predictions over the frequency ranges 221-606 Hz, 1046-1321 Hz and 1871-2036 Hz were averaged and their means, variances from means and percentage differences tabulated (see Table 4-2). The radius predictions for the 1 mm diameter hole were found to agree with the physically measured value to within 10% for the frequency ranges of 1046-1321 Hz and 1871-2036 Hz. Over the frequency range of 221-606 Hz, the predictions for the 1 mm radius hole agreed with the physical measurement to within 15%. The radius predictions for the 2 mm, 3 mm and 4 mm radius holes were generally very poor. These results suggest that, with the adapted "small radius" theory incorporated, the hole size prediction method is able to successfully predict the sizes of smaller leaks but breaks down when the holes become larger than 1 mm in diameter.

Frequency range	Measured radius (mm)	Average prediction	Variance	Percentage difference (%)
221-606	2.00	3.51	1.51	76
	1.50	2.70	1.20	180
	1.00	1.44	0.44	44.00
	0.50	0.43	0. 07	14.00
1046-1321	2.00	3.46	1.46	73
	1.50	2.38	0.88	59
	1.00	1.33	0.33	33
	0.50	0.48	0.02	3.27
1871-2036	2.00	3.09	1.09	55
	1.50	1.81	0.31	21
	1.00	7.37	6.37	637
	0.50	0.54	0.04	8

Table 4-2: Hole size predictions with associated accuracies for cylindrical pipe 1 containing 1 mm, 2 mm, 3 mm and 4 mm diameter leaks using the adapted small radius theory

4.4.3 Radius Prediction Results for Cylindrical Pipe 2

To confirm the effectiveness of the adapted "small radius" theory in predicting the sizes of smaller holes, the method was applied to the input impedance measurements of cylindrical pipe 2 with 0.2 mm and 0.3 mm diameter leaks that were determined in Section 4.3.4 (after removing the effects of the adapter).

Figure 4-12 compares the predictions of the hole radii with their actual values. It is clear that the radius of the 0.2 mm diameter leak has generally been predicted well over the entire plotted frequency range. The radius of the 0.3 mm diameter leak has been well predicted over most of the frequency range with a reduction in the accuracy of the predictions between 500 Hz and 1000 Hz.

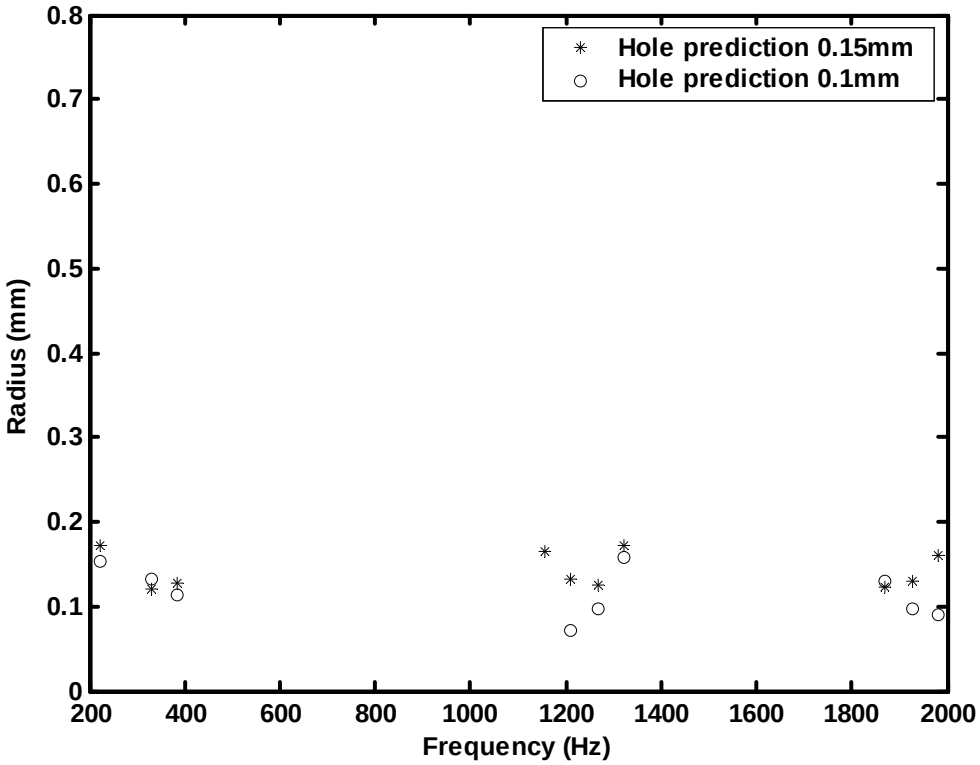

Figure 4-12: Hole size predictions for cylindrical pipe 2 containing 0.2 mm and 0.3 mm diameter leaks using the adapted small radius theory

The radius predictions over the frequency ranges 221-386 Hz, 1211-1321 Hz and 1871-1981 Hz were averaged and their means, variances from means and percentage differences tabulated (see Table 4-4). The radius predictions for both holes were found to agree with the physically measured values to within 10% over the three frequency ranges calculated. These results confirm that when the adapted "small radius" theory is incorporated into the methodology of Section 4.3.1, the sizes of smaller leaks can be successfully predicted.

Frequency range (Hz)	Measured radius (mm)	Average prediction (mm)	Variance (mm)	Percentage difference %
221-386	0.15	0.14	0.01	6.7
	0.10	0.11	0.01	10
1211-1321	0.15	0.14	0.01	6.7
	0.10	0.11	0.01	10
1871-1981	0.15	0.14	0.01	6.7
	0.10	0.11	0.01	10

Table 4-3: Hole size predictions with associated accuracies for cylindrical pipe 2 containing 0.2 mm and 0.3 mm diameter leaks using the adapted small radius theory

4.5 Extending Theory to multiple leaks

The analytical methods described in this chapter cannot be easily extended to the case of investigating multiple leaks. This is due to an increased number of unknown variables resulting in the need for complex mathematical formulations to find the solution. The case of extending to multiple leaks can be illustrated by applying the procedure described in Section 4.3 to Figure 4-13, which shows a cylindrical pipe with two leaks in the side wall.

It is possible to calculate the load impedance, $Z_{load(3)}$, from the expression for the radiation impedance given by Equation (2.26). From this the value of $Z_{load(3)}$, the input impedance, $Z_{in(3)}$, of the third cylindrical duct can be calculated using Equation (2.23). Meanwhile, the input impedance, $Z_{in(1)}$, of the first cylindrical section is known as it is equal to the measured experimental input impedance of the cylindrical pipe. Using this value of $Z_{in(1),}$ the load impedance, $Z_{load(1),}$ can be calculated from the inversion of the theoretical input

impedance equation given by Equation (4.4). However, despite having calculated $Z_{load(3)}$, $Z_{in(3)}$, $Z_{in(1)}$ and $Z_{load(1),}$ it is still not possible to calculate the hole impedances, $Z_{h(1)}$ and $Z_{h(2),}$ as the values of $Z_{load(2)}$ and $Z_{in(2)}$ remain unknown. It is worth noting that the number of unknown hole impedances will increase with the number of leaks present in the side wall of the cylindrical pipe. This makes the sizing of multiple leaks using analytical equations a non trivial problem.

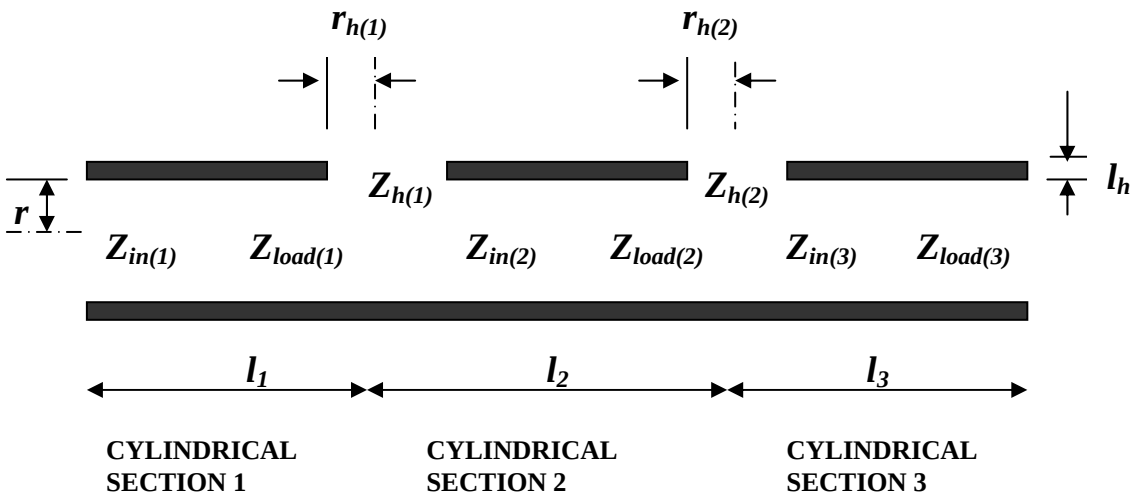

Figure 4-13: Schematic representation of a cylindrical pipe with two leaks

4.6 Concluding Remarks

It has been demonstrated in this chapter that by modelling a leak in a cylindrical pipe as a side branch, and providing the appropriate theoretical approximations are made, analytical methods can be used to predict the size of a single hole in the side of a pipe. However, extending this analytical approach to multiple leaks is non–trivial as the resulting expressions tend to have too many unknown parameters.

The remainder of this thesis concentrates on using numerical optimisation techniques to investigate cases where more than one leak is present in the side wall of a cylindrical pipe.

$Z_{load(3)}$

Chapter 5

Optimisation Theory

A major limitation was discovered in Chapter 4 when applying an analytical approach to the problem of leak detection as discussed in Section 4.5. The limitation was that extending the analytical methods to the investigation of more than one leak proved impossible, with the expression becoming extremely complicated.

For this reason, it was decided to explore the potential of a numerical optimisation approach in the investigation of both single and multiple leaks in ducts. In this chapter, the theory and algorithms underpinning various numerical optimisation methods are described.

Numerical optimisation involves finding the optimal solution to a function which is dependent on one or more variables. The function being optimised is in many cases a theoretical model developed after studying both the problem and solution being sought. Finding the solution to the function therefore leads to the solution of the physical problem that is represented by the function. The methodology of finding the optimal solution of the function is the minimisation or maximisation of a related "objective" function. It has been found that most real world problems are solved by minimisation of the objective function. This is indeed the case for the input impedance equations describing a leaky duct. However, it is important to note that there is no loss of generality in describing a function just on the basis of minimisation. The maximisation solution if required can simply be found by inversing the sign of the minimisation expression.

In Chapters 6 and 7, the application of single variable, two variable and multiple variable optimisation methods to the problem of detecting, locating and finding the size of one or more leaks in a cylindrical pipe will be discussed. To begin with though, it is necessary to understand how the various optimisation methods work. In this chapter, the different optimisation methods are described and explained.

5.1 Definition of Numerical Optimisation

Numerical optimisation is a type of mathematical problem where it is required to minimize or maximise a non-linear function *f(x)* on an *n*-vector with variables *x* defined in a closed connected set *X* having a set of non-linear or linear constraints [40]. Hence a typical numerical optimisation problem is usually formulated as follows:

Minimise *f(x)* under the conditions $x \in X \subset R$ and $g_i(x) \leq 0$ for $i = 1,2,3\ldots..,m$, where $g_i(x)$ are the constraints, *R* is the set of real numbers and *m* the number of iterations in each search direction.

It is common to replace the constraints $g_i(x)$ by simple boundaries in which case the numerical optimisation is referred to as unconstrained optimisation. When conditions are imposed, the specific name of constrained optimisation is used. All the optimisation methods considered in this work employ unconstrained optimisation. The common feature of constrained and unconstrained optimisation is that they are both based on iterative methods.

An iterative method in the context of numerical optimisation is defined as a dynamic process that generates a sequence of approximations converging to the exact solution. At

each step of the iteration, an improved approximation is obtained from the previous one. The accuracy of the solution depends on the number of iterations performed. Most iterative methods retain the coefficients matrix in its original form throughout the process and have the advantage of requiring minimal memory.

5.1.1 Comparison of Optimisation and Analytical Methods

By definition, optimisation can be used to solve any function representing a modelled problem as long as the function has been correctly described mathematically. By adjusting the unknown function parameters in an iterative process, the optimum solution of the function is eventually found. As the function has to be calculated over and over again at each iteration stage, optimisation solutions are computer intensive. However, with the advent of faster computer processing powers this is becoming less of a limitation.

The main limitation of optimisation methods is that there are several things which can go wrong during the process of optimisation, even if a function is properly described mathematically. Errors can arise due to the problem of local minima, parameter values that are out of reasonable limits, lack of convergence of the function and unnecessarily long computations due to wrong choice of the sensitivity levels. Most of these can be overcome by carefully testing the function and offering the optimisation added information such as simple bounds of parameters. However, this is an additional task which is not encountered in analytical solutions.

On the contrary no iteration is required in an analytical method for finding a solution to a problem. Analytical methods therefore tend to be less computer intensive and are generally more efficient mathematically as they require less calculations of the function. Once a solution is feasible from the analytical function, its application is guaranteed. This is not

the case with optimisation solutions where added information such as simple parameter bounds may be required to offer guidance to the optimisation routine.

The greatest limitation of analytical methods, as discovered in Chapter 4, is that a solution is not always available. This is as a result of too many unknown parameters or the difficulty of finding a mathematical expression if the problem is too complex.

5.1.2 Summary of Numerical Optimisation Terms Used

Several commonly used terms in numerical optimisation are employed in this thesis. Detailed definitions of the terms are given throughout this chapter. However for clarity, a summary of the definitions is given here.

(1) Target function; this is a function with known values, often determined experimentally. The known values are used as a guide to the optimisation. Details of how this is done are discussed in the sections on individual optimisation methods (Sections 5.2, 5.3 and 5.4).

(2) The function being optimised is a theoretical model with similar characteristics or variable types as the target function. Some or all of the variables of this function are adjusted during optimisation to find a match with specified values of the target function.

(3) Objective function f or $f(x)$; this is a combination of the target function and the function being optimised, designed to yield a minimum value representing the optimal function solution.

(4) Local minimum k; this is the minimum value of the function within a certain bound which is a subset of the possible function parameter values. Usually there are several local minima of a function during optimisation. A more detailed definition of local minimum is given in the discussions on the individual optimisation methods.

(5) Global minimum $\bar{k}$; this is the actual minimum value of the function f. It can also be referred to as the smallest of all the local minima.

(6) Local minimiser; this is the line or position vector on which function f is dependent. Minimisation of this line, leads to a subsequent reduction in the value of function f.

(7) Global minimiser; this is the line or position vector containing the global minimum of function f.

5.2 Optimisation of a One Variable Function

Consider the case where the function f has a single variable x. Optimisation enables the value or values of x (for $x \in \Re$) for which f is a minimum to be found. In most cases the problem may actually only require values which satisfy simple bounds, such that

$$x \geq h \text{ or } x \leq g \qquad (5.1)$$

All values of x which do not satisfy the condition specified in Equation 5.1 are rejected as they are values known to be beyond the limits of the required solution. The requirement specified in Equation (5.1) can also be expressed as

$$x \in [h, \infty), x \in (-\infty, g] \text{ or } x \in [h, g] \tag{5.2}$$

In optimisation terms, when finding the minimum of a function with one variable, care must be taken to ensure that the minimum value found does not belong to a dip in the function curve such that another lower dip lies elsewhere in the curve. In fact the minimum value of the function found must represent the lowest dip in the curve of the function. This value is called the global minimum, $\bar{k}$, of function f and is expressed in mathematical terms as a value in a closed interval $\Re$ of a function domain, with the global minimum $\bar{k} \in \Re$ being present if $f(x) \geq f(\bar{k})$ for all $x \in \Re$. The point $\bar{k}$ is called a global minimiser for f on $\Re$.

The several minimum values of the function found during the process of optimisation resulting from the existing dips in the function curve are called local minimum function values in contrast to the global minimum value. Therefore, a function with one variable has a local minimum on a closed interval $\Re$ in its domain, at $k \in \Re$, if there is some $\delta > 0$ such that $f(x) \geq f(k)$ whenever $|x - k| < \delta$ and $k \in \Re$. The point k is called a local minimiser for f on $\Re$. The meaning of this mathematical expression is that $f(x) \geq f(k)$ for all x sufficiently close to k.

The other way of defining local minimisers is in terms of calculus notation. This is because differentiation of the function f can be used to find out if the function is being optimised near to the local minimum value or away from the local minimum value. Differentiating a function can also be used to indicate if the function local minimum has been calculated. A local function minimum occurs when the derivative of function f is equal to zero, $f'(k) = 0$, which in differentiation terms indicates that the slope of the function at that point is horizontal. Since a function derivative of zero also occurs at the

maximum function value, further tests are carried out to confirm that the function value is a local minimum. This can be done by considering the value of $f'(k)$ near its root as x is increased. If $f'(k)$ changes from negative to positive then the function value at $f'(k) = 0$ is a local minimum. Alternatively, if the second derivative of $f(k)$ is greater than zero, $f''(k) > 0$, then the function value is a local minimum.

The procedure for determining the function local minimum using the function derivatives can be written as follows:

(a) If $f'(x) \neq 0$ for x near k (excluding $x = k$), then:

(i) f has a local minimum at k if $f'(x)$ changes sign from negative to positive as x increases through k;

(ii) f has a local maximum at k if $f'(x)$ changes sign from positive to negative as x increases through k;

(iii) f has a point of inflection at k if $f'(x)$ does not change sign as x increases through k.

(b) If $f''(k) \neq 0$ then:

(i) f has a local minimum at k if $f''(k) > 0$;

(ii) f has a local maximum at k if $f''(k) < 0$;

If $f''(k) = 0$ but $f'''(k) \neq 0$ then k is a point of inflection.

To find the minimum function value involves finding the local minimum function values from which it is possible to determine the global minimum function value.

5.3 Methods for Optimising One Variable Functions

5.3.1 Newton-Raphson Method

The Newton-Raphson method has previously been used to successfully find the local minimiser for a function with one variable [41-44]. Optimisation using the Newton-Raphson method involves finding the function root at $f'(x) = 0$ using Equation (5.3).

$$x^{r+1} = x^r - \frac{f'(x^r)}{f''(x^r)} \tag{5.3}$$

where x^r is the minimiser being incremented at the current position of the function, x^{r+1} is the incremented position, $f'(x^r)$ is the first derivative of the function at the current position and $f''(x^r)$ is the second derivative of the function at the current position.

The process of optimisation starts by specifying a current position for the minimiser, x^r. The next position of the minimiser is calculated by substituting the current position into Equation (5.3). The iterative process is repeated until the minimum function value is calculated.

As discussed previously, a test is built into the method to determine whether the optimisation is iterating towards a local minimum or towards some other type of stationary point. To approach a local minimum at each iteration step of $f(x)$, either $f'(x^r) > 0$ and $x^{r+1} < x^r$ or $f'(x^r) < 0$ and $x^{r+1} > x^r$ should hold. These two conditions can be combined into a single test condition as follows:

$$(x^{r+1} - x^r) f'(x^r) < 0 \tag{5.4}$$

Therefore, Equation (5.3) can be rewritten to incorporate the single test condition as follows:

$$(x^{r+1} - x^r) f'(x^r) = \frac{(f'(x^r))^2}{f''(x^r)} \tag{5.5}$$

Examination of Equation (5.5) shows that a division by $f'(x^r)$ would bring the equation back to Equation (5.3). Therefore Equation (5.3) and (5.5) are proportionate and can work in a similar way during the optimisation though Equation (5.5) gives an added advantage of incorporating a test condition in each iteration step.

5.3.2 Interval Reduction Method

The Interval Reduction method uses function values to carry out the iterations with the aim of progressively reducing the interval between the function values during the process of optimisation [45]. The reduction of the interval between the function values at each step of the optimisation then leads to finding the function minimum. Thus, contrary to the Newton-Raphson method, in the Interval Reduction method it is assumed that nothing is known about the derivatives of f .

One disadvantage of the Interval Reduction method is that it is possible to have several local minimum values of the function in an interval such that the reduction process fails to pick out all the function minimum values in the current interval. This happens because the method reduces the interval between two function values without examining all the

possible function values in that interval. To overcome this limitation it is necessary to provide a check to determine that there is only one local minimum in the interval where the reduction process is happening. The condition of a function variable having only one minimum value in a given interval is known as unimodality.

5.3.3 Grid Search Method

The Grid Search method is a variation of the Interval Reduction method which works by defining extra interior points within the interval that is being reduced. For example, choosing three interior points in an interval creates four subdivisions in the interval, any of which can contain the minimum value of the function. The method then provides a check to determine which of the subdivisions contains the local minimum and should be selected for use in the next interval reduction phase.

One common check that is used to select which of the subdivisions to use in the next iteration stage is to compare the function values on the current interior points and boundary points. Suppose the interval is (x_0,x_4) and the points of subdivision are x_1, x_2 and x_3, where $x_0 < x_1 < x_2 < x_3 < x_4$ and $x_1 - x_0 = x_2 - x_1 = x_3 - x_2 = x_4 - x_3$. Assuming unimodality, only the following possibilities can arise:

$f(x_1) \le f(x_2) < f(x_3)$, in which case the minimiser lies in (x_0, x_2);

$f(x_1) > f(x_2) < f(x_3)$, in which case the minimiser lies in (x_1, x_3);

$f(x_1) > f(x_2) \ge f(x_3)$, in which case the minimiser lies in (x_2, x_4);

Thus we should take as the next interval the subinterval - either (x_0, x_2), (x_1, x_3) or (x_2, x_4) - that has the lowest calculated value of f at the midpoint.

To obtain a minimum to *n* decimal places, the iteration is stopped after an interval of length less than or equal to 10^{-n} is obtained which contains the local minimum. The midpoint of that interval then gives the local minimum with an error bound of $5\times10^{-(n+1)}$, i.e. it gives the local minimum to *n* decimal places. Since each iteration halves the interval length, an interval *(a,b)* is reduced to a length of at most 10^{-n} when *k* is the smallest integer that satisfies

5.3.4 Golden Section Search Method

An improvement to the Grid Search method can be made by relaxing the rule that the subdivisions within the interval being reduced should be equal. The Golden Section Search method, therefore, works by relaxing the requirement for equal subdivisions and uses only two interior points and one new function evaluation for each iteration [44, 46]. The condition of unimodality is still assumed for the Golden Section Search method.

The process of finding the minimum function value starts by calculating the function values of the four initial points chosen, (x_0, x_1, x_2, x_3), where x_0 and x_3 are the boundary points and x_1 and x_2 are the two interior points. The condition of the Golden Section Search method is that the distance between x_0 and x_1 and x_2 and x_3 should be equal.

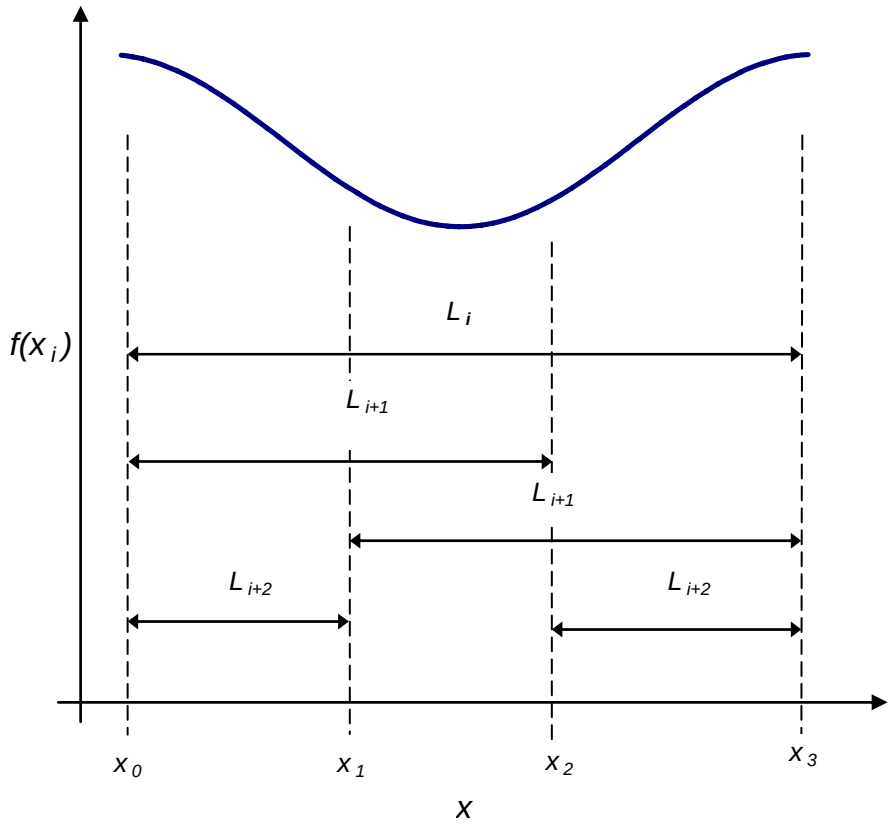

Figure 5-1: Subdivisions using the Golden Section Search method

During iteration the current length is denoted by L_i, and its end points by x_0 and x_3 such that $L_i = x_3 - x_0$. The points of subdivision, x_1 and x_2, are such that the subintervals (x_0, x_1) and (x_2, x_3) are of equal length, but not the same length as (x_1, x_2). This makes it possible to choose the interval length for the next iteration, L_{i+1} to be equal to both $x_2 - x_0$ and $x_3 - x_1$. The function evaluations can then be reduced by choosing the positions of x_1 and x_2 so that they are points of subdivision, not just of the current iteration but potentially the next iteration. Therefore, if the next interval is (x_0, x_2), then x_1 should be the next subdivision of it nearer x_2; while if the next interval is (x_1, x_3) then x_2 should be the next subdivision of it nearer x_1. Examination of Figure 5-1 shows that if the

subdivision (x_0, x_2) is chosen, the length of the interval in the iteration L_{i+2} is equal to $x_1 - x_0$. Meanwhile, if the next subdivision chosen is (x_1, x_3), L_{i+2} equals $x_3 - x_2$.

The logic of choosing intervals as described above makes it possible to calculate a fraction σ so that L_{i+1} is written as:

$$L_{i+1} = \sigma L_i \tag{5.6}$$

where $0<\sigma<1$. Therefore L_{i+2} can be written as:

$$L_{i+2} = \sigma^2 L_i \tag{5.7}$$

By examination of Figure 5-1, L_i can be expressed as:

$$L_i = L_{i+1} + L_{i+2} \tag{5.8}$$

where L_{i+1} is equal to $x_2 - x_0$ or $x_3 - x_1$ and L_{i+2} is equal to $x_1 - x_0$ or $x_3 - x_2$.

Substituting Equations (5.6) and (5.7) into Equation (5.8) leads to:

$$L_i = \sigma L_i + \sigma^2 L_i \tag{5.9}$$

From Equation (5.9) a quadratic equation can be written as shown in Equation (5.10).

$$\sigma^2 + \sigma - 1 = 0 \tag{5.10}$$

The roots of Equation (5.10) are $\frac{1}{2}\left(-1-\sqrt{5}\right)$ and $\frac{1}{2}\left(-1+\sqrt{5}\right)$. Thus, since $0<\sigma<1$, we have $\sigma = \frac{1}{2}\left(-1+\sqrt{5}\right) = 0.618034$.

Therefore, given the length of the initial interval, the length of all subsequent intervals and the positions of subdivisions can be determined. If the local minimiser lies in the interval (x_0, x_3) at a particular stage, then the points of subdivision x_1 and x_2 are obtained as follows: $x_3 - x_1 = x_2 - x_0 = \sigma(x_3 - x_0)$.

5.4 Optimisation of a Two Variable Function

In this section, optimisation methods for functions involving two variables are developed using many of the ideas used in the optimisation of functions with one variable. Detailed descriptions of the numerical optimisation methods involving two variables are given by [46]. In the same way that the optimisation of a function with one variable can be represented through a two dimensional plot, two variable optimisation methods are represented using three dimensional plots. For example, Figure 5-2 shows the three-dimensional plot of a smooth two variable function, $z = f(x_1, x_2) = 1000x_1^2 - x_1x_2 + 1000x_2^2 - x_1$. When a two variable function is depicted in a three dimensional plot, it is possible to draw key information about the behaviour of the function during optimisation.

A two variable function can also be represented in a two dimensional form as a contour plot. Figure 5-3 shows a contour plot of the function $z = f(x_1, x_2) = 1000x_1^2 - x_1x_2 + 1000x_2^2 - x_2$, represented three dimensionally in Figure 5-2.

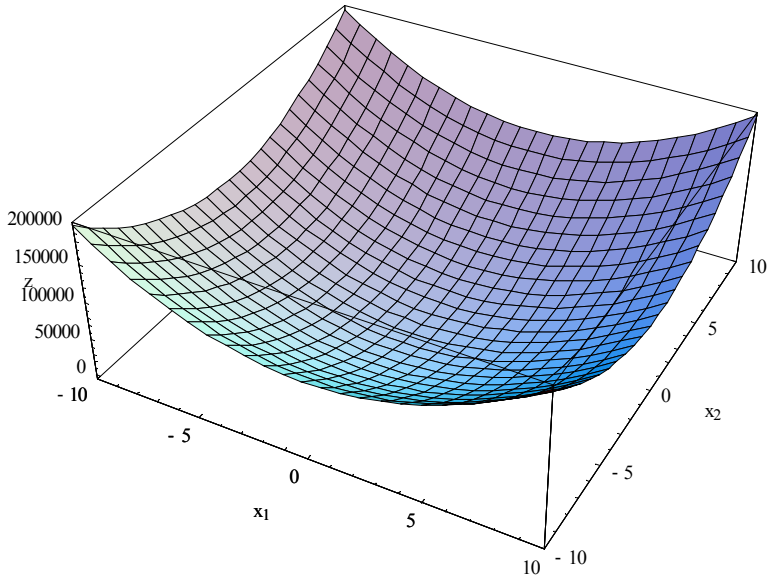

Figure 5-2: Three dimensional plot of a two variable function

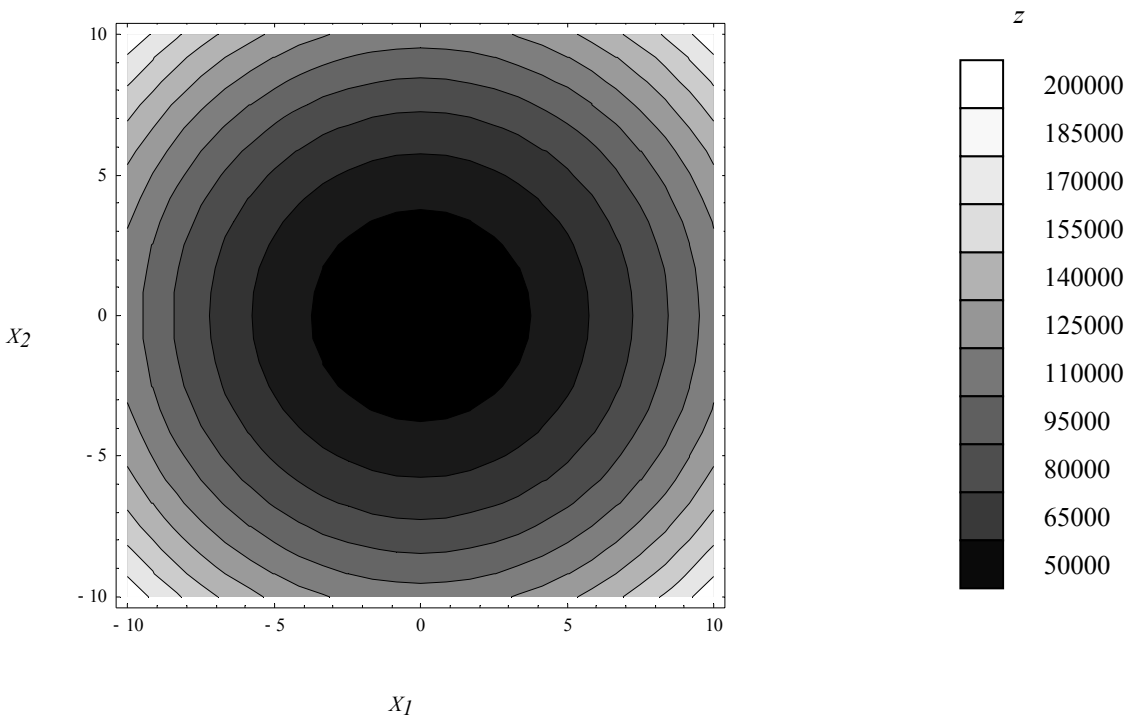

Figure 5-3: Contour plot of two variable function

In Figure 5-3, the x_1 and x_2 axes show the possible values that the function variables can have during the optimisation. The grey shading represents the z values which are the possible function values during optimisation.

The basic process of optimising a two variable function involves finding the function minimum in terms of both x_1 and x_2 at each optimisation step. After initiating the optimisation with values of x_1 and x_2, the next step is to find a minimum value along one axis. If a minimum value of the function is found, the optimisation using that variable is stopped. The next step is to find the minimum function value using the other variable. Once the minimum function value is found using the second variable, the optimisation is stopped again. The process is then repeated starting with the first variable. This optimisation procedure can be described in terms of perpendicular steps as shown in Figure 5-4. The details of various different optimisation methods will be discussed in the following sections, which include an explanation of how the variable values are retained or discarded at each optimisation stage and a discussion of the various techniques for determining the step sizes and the direction of the optimisation.

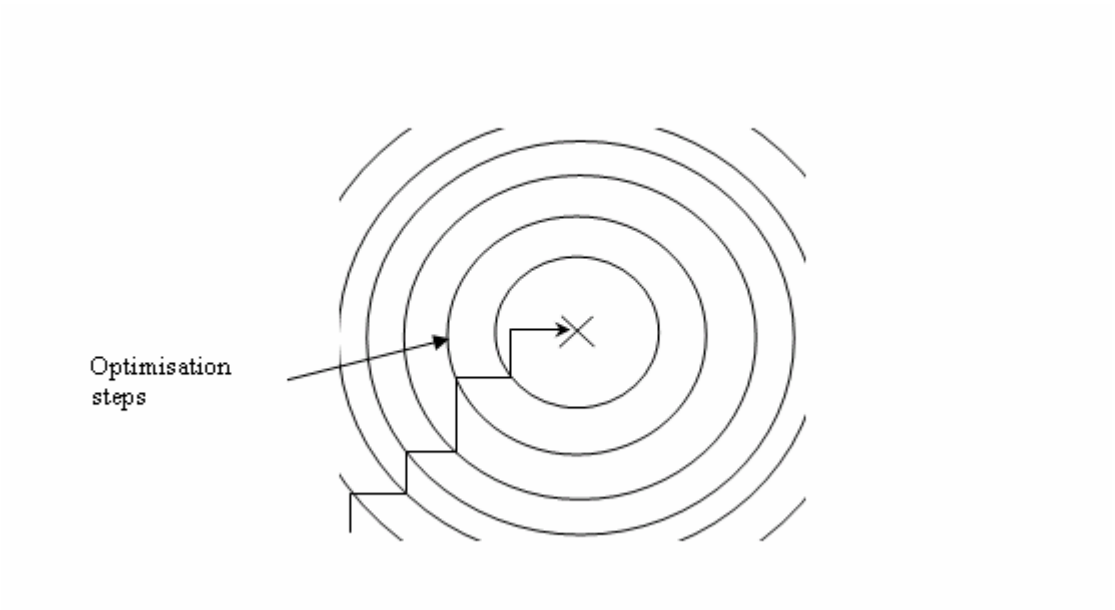

Figure 5-4: Perpendicular steps during optimisation to find the function minimum

Optimising in each of the step directions shown in Figure 5-4 is very similar to the optimisation of a one variable function. As in the one dimensional case, local minima can occur at boundary points or interior points of $\Re$. In one dimension, the points where the tangent to a graph is horizontal are called stationary points. Similarly, in two dimensions, a stationary point of a smooth function $f(x_1, x_2)$ is a point where the tangent plane to the graph of *f* is horizontal. Furthermore, in one dimension, a point *k* is a stationary point of a smooth function *f(x)* if $f'(k) = 0$. There is a similar equivalence in two dimensions, namely that a point (k_1, k_2) is a stationary point of a smooth function $f(x_1, x_2)$ if

$$\frac{\partial f}{\partial x_1}(k_1, k_2) = 0 \text{ and } \frac{\partial f}{\partial x_2}(k_1, k_2) = 0. \tag{5.11}$$

By extending the definition of a local minimum and global minimum given in Section 5.2 to the two dimensional case, it can be stated that a function of two variables, on some region $\Re$, has a local minimum $f(k_1, k_2)$ at $(k_1, k_2) \in \Re$ if $f(x_1, x_2) \geq f(k_1, k_2)$ for all $(x_1, x_2) \in \Re$ sufficiently close to (k_1, k_2). The point (k_1, k_2) is called a local minimiser for *f* on $\Re$. Similarly, the function has a global minimum on a closed interval $\Re$ in its domain, at $(\bar{k}_1, \bar{k}_2) \in \Re$, if $f(x_1, x_2) \geq f(\bar{k}_1, \bar{k}_2)$ for all $(x_1, x_2) \in \Re$. The point $(\bar{k}_1, \bar{k}_2)$ is called a global minimiser for *f* on $\Re$.

For a two variable function, planes cutting through the three dimensional space of the function, either along the variable x_1 or x_2, are called the section functions of *f*. They are functions of one variable, obtained from *f* by fixing the value of x_1 or x_2 while varying the other parameter.

The lines of intersection between the section functions and the shape of the function *f* represent possible lines of optimisation where a minimum can be sought, such that the local minima at the interior points of a smooth function $f(x_1, x_2)$ occur where the tangent plane to the graph of *f* is horizontal. The tangent plane by definition is a plane in (x_1, x_2, z) space that just touches the graph describing the two variable function *f*.

One dimensional graphs of the section functions can be obtained by slicing through the surface $z = f(x_1, x_2)$ with vertical planes. The section function f_1 is calculated by slicing a vertical plane defined by giving x_2 a constant value while varying x_1 such that the vertical plane is parallel to the x_1 -axis. The section function f_2 is calculated by slicing a vertical plane defined by giving x_1 a constant value while varying x_2 such that the vertical plane is parallel to the x_2 -axis. In this way the (x_1, x_2) coordinates of any minimum on the $f(x_1, x_2)$ surface can be defined by finding the minimum values on both the section function f_1 and section function f_2. The surface of function *f* has a local minimum if every vertical plane slicing through a particular point shows a minimum at that point. Therefore, the surface of function *f* has a horizontal tangent if every vertical plane slicing through a particular point shows a horizontal tangent at that point. Similarly the surface has a stationary point if every vertical plane slicing through a particular point shows a stationary point at that point

Instead of the vertical planes being parallel to either the x_1 –axis or x_2 –axis, a plane orientated in the direction of a minimum can be specified by defining a straight line in the (x_1, x_2) - plane in the parametric form as

$$\begin{aligned} x_1(m) &= k_1 + mq_1, \\ x_2(m) &= k_2 + mq_2, \end{aligned} \tag{5.12}$$

where *m* is the parameter determining the angle of the plane (x_1, x_2) in (x_1, x_2, z) space, (k_1, k_2) is a point on the line, and q_1 and q_2 are constants.

Thus, any function whose graph is the curve of intersection of a surface $z = f(x_1, x_2)$ and a vertical plane can be written as $F(m) = f(x_1(m), x_2(m))$. Showing that the surface has a stationary point at (k_1, k_2) is equivalent to showing that the graph of every function *F(m)* through that point has a stationary point at that point. It follows that if the section functions through (k_1, k_2) have stationary points (k_1, k_2), the intersection functions *F(m)* through (k_1, k_2) have stationary points.

It can be shown that *F* has a stationary point at $m = 0$, for all such functions *F* for every choice of q_1 and q_2. The first step is to define equations for the section functions:

$$\frac{\partial f}{\partial x_1}(k_1, k_2) = f_1'(k_1) \tag{5.13}$$

$$\frac{\partial f}{\partial x_2}(k_1, k_2) = f_2'(k_2) \tag{5.14}$$

where f_1 and f_2 are the section functions through k_1, k_2, and have stationary points at k_1, k_2 if $f_1'(k_1) = 0$ and $f_2'(k_2) = 0$. The derivative of *F* can be found by the chain rule for the function of two derivatives:

$$\frac{dF}{dm} = \frac{\partial f}{\partial x_1}\frac{dx_1}{dm} + \frac{\partial f}{\partial x_2}\frac{dx_2}{dm}. \tag{5.15}$$

also,

$$\frac{dx_1}{dm} = q_1 \tag{5.16}$$

and

$$\frac{dx_2}{dm} = q_2 \tag{5.17}$$

Therefore,

$$\frac{dF}{dm}(0) = q_1 \frac{\partial f}{\partial x_1}(k_1, k_2) + q_2 \frac{\partial f}{\partial x_2}(k_1, k_2) \tag{5.18}$$

$\frac{dF}{dm}(0)$ is zero when the partial derivatives of f vanish at (k_1, k_2), whatever the values of q_1 and q_2.

5.4.1 Basic Optimisation Procedure

The local minimisers of a two variable function can be determined by finding the stationary points through Equation (5.18). Since a stationary point can either be a maximum or minimum point, an extra check is needed which can be developed by defining a Taylor polynomial for any function value $a(x_1, x_2)$ near the minimum $f(k_1, k_2)$.

$$\begin{aligned} a(x_1, x_2) = f(k_1, k_2) &+ \frac{\partial f}{\partial x_1}(k_1, k_2)(x_1 - k_1) + \frac{\partial f}{\partial x_2}(k_1, k_2)(x_2 - k_2) \\ &+ \frac{1}{2}\frac{\partial^2 f}{\partial x_1^2}(k_1, k_2)(x_1 - k_1)^2 + \frac{\partial^2 f}{\partial x_1 \partial x_2}(k_1, k_2)(x_1 - k_1)(x_2 - k_2) \\ &+ \frac{1}{2}\frac{\partial^2 f}{\partial x_2^2}(k_1, k_2)(x_2 - k_2)^2. \end{aligned} \tag{5.19}$$

The vectors for X and K can be written as $X = \begin{bmatrix} x_1 \\ x_2 \end{bmatrix}$ and $K = \begin{bmatrix} k_1 \\ k_2 \end{bmatrix}$. A vector h can also be defined as:

$$h = X - K \tag{5.20}$$

Therefore

$$h = \begin{bmatrix} h_1 \\ h_2 \end{bmatrix} = \begin{bmatrix} x_1 - k_1 \\ x_2 - k_2 \end{bmatrix} \tag{5.21}$$

The gradient vector of function f can be written as:

$$\nabla f(x) = \begin{bmatrix} \frac{\partial f}{\partial x_1}(x) \\ \frac{\partial f}{\partial x_2}(x) \end{bmatrix} \tag{5.22}$$

The Hessian matrix $G(x)$ is given by

$$G(x) = \begin{bmatrix} \frac{\partial^2 f}{\partial x_1^2} & \frac{\partial^2 f}{\partial x_1 \partial x_2} \\ \frac{\partial^2 f}{\partial x_2 \partial x_1} & \frac{\partial^2 f}{\partial x_2^2} \end{bmatrix}. \tag{5.23}$$

For a smooth function, $\frac{\partial^2 f}{\partial x_2 \partial x_1} = \frac{\partial^2 f}{\partial x_1 \partial x_2}$ and the Hessian matrix is symmetric. Therefore, Equation (5.19) can be written as

$$a = a(K+h) = f(K) + h^T \nabla f(K) + \frac{1}{2} h^T G(K) h. \tag{5.24}$$

At the minimum $\nabla f(K) = 0$ and Equation (5.24) simplifies to

$$a = a(K+h) = f(K) + \frac{1}{2} h^T G(K) h. \tag{5.25}$$

To check if the stationary point is a minimum, $\nabla f(K)$ and $G(K)$ are used in a similar manner to when the stationary points were checked using $f'(k)$ and $f''(k)$. That is, if $G(K) > 0$ and $\nabla f(K) = 0$ then the stationary point found through Equation (5.25) is a local minimiser of *f*.

5.5 Methods for Optimising Two Variable Functions

Methods of optimising a function with two variables use a similar search strategy which follows a three step process. The methods are extensively covered by [42, 47-49]. The process starts by making an initial approximation and proceeds as follows:

(a) A search direction is selected

(b) A local minimiser is calculated in the search direction

(c) The optimisation proceeds to the new point.

The three steps are repeated until either the desired accuracy is achieved or the algorithm is deemed to have failed. The method of choosing a search direction is known as a line search method.

5.5.1 Alternating Variables Method

The search direction alternates between the variables, so that the first search is along a line parallel to the x_1 -axis, the second search is along a line parallel to the x_2 -axis, the third search is along a line parallel to the x_1 -axis, and so on. That is, the search directions are:

$q^0 = [1,0],\ q^1 = [0,1],\ q^2 = [1,0],\ q^3 = [0,1],\ \ldots\ldots$

The procedure for finding a two variable function minimum using the Alternating Variables method therefore works as follows:

(a) A search direction is chosen to be parallel to each of the axes in turn

$$q^r = \begin{cases} [0,1]^T & for \quad r \quad even \\ [1,0]^T & for \quad r \quad odd \end{cases}$$

(b) Starting from x^r determine a line minimiser for the function along the line $X^r + mq^r$ using one of the methods for finding the local minimiser for a one dimensional function, such as the Interval Reduction method. In this way a value for *m* will be found that minimises $f(X^r + mq^r)$.

(c) The next stage of the optimisation is continued by moving to the new point $X^{r+1} = X^r + mq^r$

(d) The optimisation is stopped if the required accuracy is reached or the iteration limit has been reached, otherwise the procedure is repeated from step (a) with *r* replaced by *r+1*.

5.5.2 Steepest Descent Method

The major deficiency in the Alternating Variables method is that no use is made of the function *f* properties in arriving at the search direction. The Alternating Variables method only follows a predetermined sequence of search directions. The Steepest Descent method on the contrary makes use of the properties of the function *f* to generate a new search direction at each iteration, along which *f* is guaranteed to be reduced in value [49]. In the Steepest Descent method, the search direction used at each iteration is the direction in which *f* is currently decreasing most rapidly.

The direction in which *f* is decreasing most rapidly is determined by finding the most negative value of the gradient of *f* at the current point. This is determined by calculating the rate of change of a function with two variables, at a point *x*, in the direction of a unit vector *q*. This is the same as the rate of change of *f* along the line $x(m) = x + mq$ at $m = 0$.

$$\frac{d}{dm} f(x + mq) \tag{5.26}$$

5.6 Optimisation of a Multiple Variable Function

The practicality of implementing optimisation methods by searching in a particular direction and then minimising the function in that direction by means of a line search are largely utilised in optimisation techniques involving multiple variables [43], [50] and [51]. The Newton-Raphson method, Broyden-Fletcher-Goldfarb-Shanno (BFGS) method and the Fletcher-Reeves method can all be fitted into this framework. These methods are

widely used for solving a variety of constrained and unconstrained non-linear optimisation problems.

Unconstrained optimisation of a function of *n* variables is achieved by generalising the techniques used in optimising two function variables from the two-dimensional to the *n*-dimensional case, where *n* >2 is the number of variables in the function *f*.

The definitions of the local and global minimisers discussed in Section 5.2 and Section 5.4 can be extended to the *n*-dimensional case. Therefore, it can be stated that a function of *n* variables, on some region $\Re$, has a local minimum $f(K)$ at $(K) \in \Re$ if $f(X) \geq f(K)$ for all $(X) \in \Re$ sufficiently close to K, where $K = [k_1, k_2, ..., k_n]$ and $X = [x_1, x_2, ..., x_n]$. The point K is called a local minimiser for *f* on $\Re$. The function has a global minimum on a closed interval $\Re$ in its domain, at $(\overline{K}) \in \Re$, if $f(X) \geq f(\overline{K})$ for all $(X) \in \Re$. The point $\overline{K}$ is called a global minimiser for *f* on $\Re$ where *f* is a function with *n* variables.

The location of local minimisers can also be extended to the *n*-dimensional case. Therefore to obtain the first partial derivative, the function *f* is differentiated with respect to the i^{th} variable x_i, treating all the other variables as constant. The result can be differentiated again with respect to *j* to give the second partial derivatives.

$$\frac{\partial}{\partial x_j}\left(\frac{\partial f}{\partial x_i}\right) = \frac{\partial^2 f}{\partial x_j \partial x_i} \tag{5.27}$$

Assuming that all the second partial derivatives of *f*, regarded as functions of the variables x_i, are continuous, the symmetric relationship can be written as:

$$\frac{\partial^2 f}{\partial x_j \partial x_i}(X) = \frac{\partial^2 f}{\partial x_i \partial x_j}(X) \tag{5.28}$$

The gradient vector can be generalised as

$$\nabla f(X) = \left[\frac{\partial f}{\partial x_1}(X), \frac{\partial f}{\partial x_2}(X), \cdots, \frac{\partial f}{\partial x_n}(X) \right]^T \tag{5.29}$$

As in the two dimensional case, the point at which $\nabla f(K)$=0 is called the stationary point.

The Hessian matrix *G(X)* of *f* in the *n*-dimensional case, is the *n* matrix whose elements *i,j* are given by ,

$$G_{i,j}(X) = \frac{\partial^2 f}{\partial x_i \partial x_j}(X) \tag{5.30}$$

so that

$$G(X) = \begin{bmatrix} \frac{\partial^2 f}{\partial x_1^2}(X) & \frac{\partial^2 f}{\partial x_1 \partial x_2}(X) & \cdots & \frac{\partial^2 f}{\partial x_1 \partial x_n}(X) \\ \frac{\partial^2 f}{\partial x_2 \partial x_1}(X) & \frac{\partial^2 f}{\partial x_2^2}(X) & \cdots & \frac{\partial^2 f}{\partial x_2 \partial x_n}(X) \\ \vdots & \vdots & \ddots & \vdots \\ \frac{\partial^2 f}{\partial x_n \partial x_1}(X) & \frac{\partial^2 f}{\partial x_n \partial x_2}(X) & \cdots & \frac{\partial^2 f}{\partial x_n^2}(X) \end{bmatrix} \tag{5.31}$$

The second-order Taylor polynomial approximating *f* about a point can be written in a generalised way:

$$f(K) = f(K+h) \approx f(K) + h^T \nabla f(K) + \frac{1}{2} h^T G(K) h \qquad (5.32)$$

It follows that the sufficient conditions for a local minimiser of a function with *n* variables are that:

(a) $\nabla f(K) = 0$

(b) $G(K)$ is positive definite.

One way to check for the positive definiteness of the Hessian matrix $G(K)$ is to calculate its eigenvalues. If all the calculated eigenvalues are positive then the Hessian matrix $G(K)$ is regarded as positive definite.

Another method for checking that the Hessian matrix $G(K)$ is positive definite utilises the properties of matrices and has an advantage of avoiding the computationally intensive calculation of eigenvalues. Any positive definite symmetric matrix *A* can be written as

$$A = LDL^T \qquad (5.33)$$

where *L* is a real lower triangular matrix with ones along the diagonal and *D* is the diagonal matrix with positive diagonal elements. The LDL^T decomposition gives a straightforward way of determining whether a symmetric matrix is positive definite. In the case of the Newton-Raphson method, the decomposition strategy is even more useful. The Newton-Raphson method requires solution of a linear equation of the form $Ax = b$, where a check is necessary to ensure matrix *A* is positive definite. Using the LDL^T decomposition enables the check for positive definiteness and the determination of the solutions to be carried out simultaneously.

5.7 Methods of Optimising Multiple Variable Functions

5.7.1 Newton-Raphson Method

The Newton-Raphson method for optimising a function with multiple variables uses the Jacobian matrix to solve a system of linear equations in an iterative process [46]. The equation for solving the minimiser is written as:

$$X^{r+1} = X^r - J(X^r)^{-1} h(X^r) \tag{5.34}$$

where J is the Jacobian matrix and is an n by n matrix whose i,j element $J_{ij} = \frac{\partial h_i}{\partial x_j}$.

$h = \nabla f$ which is the same as $h_i = \frac{\partial f}{\partial x_i}$ so that the Jacobian matrix is written:

$$J_{ij} = \frac{\partial}{\partial x_j}\left(\frac{\partial f}{\partial x_i}\right) = \frac{\partial^2 f}{\partial x_j \partial x_i} \tag{5.35}$$

Therefore the Jacobian matrix of $h = \nabla f$ is the Hessian matrix G of f and Equation (5.34) becomes:

$$X^{r+1} = X^r - G(X^r)^{-1} \nabla f(X^r) \tag{5.36}$$

Equation (5.36) is the Newton-Raphson iteration formula for solving $\nabla f = 0$. The equation is an extension of Equation (5.3) which was used for solving the problem in one dimension.

Equation (5.36) can be written as:

$$G(X^r)\Delta^r = -\nabla f(X^r) \tag{5.37}$$

where $\Delta^r = X^{r+1} - X^r$, is a displacement vector which is added to the current position vector to determine the next position vector. Therefore, rather than use Equation (5.36) directly, which involves solving the inverse of the matrix $G(X^r)$, Equation (5.37) can be used such that a system of linear equations are solved to find the displacement vector and calculate the next position using

$$X^{r+1} = X^r + \Delta^r \tag{5.38}$$

Similar to the two-dimensional case, it necessary to check for $G(X^r)$ positive definiteness in order to check whether the stationary point is a minimum of function *f*. In the case of the Newton-Raphson method the LDL^T decomposition of $G(X^r)$ can be used both to check for positive definiteness and to solve Equation (5.36).

While the Newton-Raphson method converges rapidly to local minimiser *K* once the iterations are sufficiently close to *K*, the method can behave rather badly if X^0 is not close to *K*. The solution to this difficulty is to combine the Newton-Raphson method with line searching.

Therefore, the process of optimisation starts with a line search using Equation (5.12). The search direction using the Newton-Raphson method is given by

$$q^r = -G(X^r)^{-1}\nabla f(X^r) \tag{5.39}$$

Equation (5.39) is equivalent to the difference vector of the Newton-Raphson method as can be seen by rearranging Equation (5.37). Therefore the method of defining the line direction given in Equation (5.39) is called the Newton-Raphson search direction. Once the search direction q^r has been found the next step is to find the derivative of the function f with the variables replaced by the search direction in terms of a single variable m. The search direction q^r and single variable m are used for finding the next minimiser values by substitution into the parametric form of the equation shown in Equation (5.12).

The number of function evaluations required at each iteration to determine the search direction is the same as the number of function evaluations needed for each step in the Newton-Raphson method without incorporating the search direction.

The Newton-Raphson method with line searches is an example of a descent method, provided $G(X^r)$ is positive definite. The descent method signifies that each step taken brings about a reduction in the function f value calculated at the current position when compared to the previous position.

Also, the first-order Taylor polynomial approximation for f about $X \neq K$ can be written as

$$f\left(X^r + \varepsilon q^{r^T}\right) \approx f(X) + \varepsilon q^{r^T} \nabla f(X) \tag{5.40}$$

From Equation 5.40 it can be seen that q is a descent direction if $\varepsilon q^{r^T} \nabla f(X)$ is less than zero. It can be noted by comparison of Equation (5.39) and Equation (5.40) that $\varepsilon q^{r^T} \nabla f(X) = -q^{r^T} G\left(X^r\right) q^r$ and that when $G(X^r)$ is positive definite $\varepsilon q^{r^T} \nabla f(X)$ is negative. Therefore, as long as $G(X^r)$ is positive definite at each iteration, the Newton-Raphson method with line searches converges to a local minimiser, if one exists.

However, there is no guarantee that $G(X^r)$ will be positive definite at each iteration. If $G(X^r)$ is not positive definite during an iteration stage, the search can be started again for a new vector for which $G(X^r)$ is positive definite. In practice this is rarely done. An alternative is to switch to another method which does give a descent direction, such as the Steepest Descent method, with search direction $q^r = -\nabla f(X^r)$.

The most popular alternative is to use a search direction which is a compromise between the Newton-Raphson search direction and the steepest descent search direction, given implicitly by

$$(G(X^r) + \upsilon I)q^r = -\nabla f(X^r) \tag{5.41}$$

where the value υ is chosen so that $G(X^r) + \upsilon I$ is a positive definite matrix, which ensures that the direction of the search is a descent direction.

The last stage of the Newton-Raphson method is to determine a value of *m* that minimises $q^{rT}\nabla f(X^r + mq^r)$ along the line $X^r + mq^r$. For this, the Interval Reduction method, Grid Search method or the Golden Section Search method discussed in Sections 5.3.2, 5.3.3 and 5.3.4 respectively can be used. Alternatively the roots of $q^{rT}\nabla f(X^r + mq^r) = 0$ can be calculated and then checked to determine whether the stationary point given by *m* is a local minimiser.

Equation (5.3) can be re-written as:

$$m^{r+1} = m^r - \frac{F(m^r)}{F'(m^r)} \tag{5.42}$$

where $F(m^r) = q^{r^T} \nabla f(X^r + mq^r)$ and $F'(m^r) = q^{r^T} G(X^r + mq^r) q^r$. By substituting the expressions for $F(m^r)$ and $F'(m^r)$ into Equation (5.42), the following is obtained:

$$m^{r+1} = m^r - \frac{q^{r^T} \nabla f(X^r + mq^r)}{q^{r^T} G(X^r + mq^r) q^r} \tag{5.43}$$

The limitation of using Equation (5.43) is that it involves recalculating the value of the Hessian matrix in the denominator at each iteration. On the other hand, the Golden Section Search method for finding the local minimiser of $f(X^r + mq^r)$ requires only a single function evaluation at each iteration of the line search. For a given one variable function, it usually takes many more iterations to obtain a local minimiser to a given accuracy using the Golden Section Search method than it does using the Newton-Raphson method. However, the total number of function evaluations required when the Golden Section Search method is used is independent of *n*, the number of variables in the original problem; whereas for the Newton-Raphson method the total number of function evaluations increases rapidly with *n*. It follows that as *n* increases, the Golden Section Search method becomes progressively more efficient than the Newton-Raphson method.

5.7.2 Rank One Method

The Rank One method seeks to improve the Newton-Raphson method by introducing another matrix $H(X^r)$ which is an approximation to the $G(X^r)$ matrix [46, 52]. A numerical procedure is used to determine the matrix $H(X^r)$ which is used instead of

$G(X^r)$ in the equations for calculating the local minimisers. Therefore, instead of calculating the matrix $G(X^r)$ at each iteration as is the case with the Newton-Raphson method, an approximation matrix $H(X^r)$ is used in the place of $G(X^r)$ when optimising function f with the Rank One method.

The procedure followed for the Rank One method is as follows:

(a) The search direction is calculated using Equation (5.44).

$$q_i = -H(X^r)^{-1}\nabla f(X^r) \tag{5.44}$$

where $H(X^r)$ is the numerically determined approximation of the Hessian matrix $G(X^r)$.

(b) A search is made in the direction q^r along the line $X^r + mq^r$ to determine the line minimiser X^{r+1}.

(c) The approximation matrix, $H(X^r)$ is updated to $H(X^{r+1})$.

To ensure that the search direction chosen at each iteration stage is in the direction of descent, the matrix $H(X^r)$ must be positive definite.

In effect, the sequence of the matrices $H(X^r)$ are chosen by an iterative process but it is also necessary to specify the initial values of the matrix $H(X^r)$. The simplest way of specifying the initial values of $H(X^r)$ is to use an identity matrix . While this may be a poor approximation of $G(X^r)$, it does give a descent direction. In fact, with $H(X^0) = I$, $q^0 = -\nabla f(x_{(0)})$ which is the steepest descent direction. Therefore unless there is a better

positive definite symmetric approximation to $G(X^0)^{-1}$ available, $H(X^0) = I$ defines the initial starting values for the approximation matrix.

Since the Hessian matrix $G(X^0)^{-1}$ is positive definite and symmetric, $H(X^r)$ should also be updated to be a symmetric matrix. A straightforward way of updating the matrix $H(X^r)$ to obtain H^{r+1} is to add a correction matrix E^r, so that

$$H^{r+1} = H^r + E^r \tag{5.45}$$

The correction matrix E^r is defined as

$$E^r = auu^T \tag{5.46}$$

where u is a non-zero vector and a is a non-zero scalar.

The vector and scalar values u and a are derived from the first order Taylor polynomial approximation for ∇f about X^r.

$$\nabla f\left(X^r\right) \approx \nabla f\left(X^r\right) + G\left(X^0\right)\left(X^0 - X^r\right) \tag{5.47}$$

when incremented Equation (5.47) can be written as

$$\nabla f\left(X^{r+1}\right) \approx \nabla f\left(X^r\right) + G\left(X^r\right)\left(X^{r+1} - X^r\right) \tag{5.48}$$

The gradient at X^r can be written as

$$\Delta s^r = s^{r+1} - s^r = \nabla f\left(X^{r+1}\right) - \nabla f\left(X^r\right) \tag{5.49}$$

where Δs^r is the gradient at X^r.

The change in X^r can be written as

$$\Delta^r \approx G(X^r)^{-1}\Delta s^r \tag{5.50}$$

also

$$\Delta^r = H^{r+1}\Delta s^r \tag{5.51}$$

Substituting Equation (5.45) into Equation (5.51) gives:

$$\Delta^r = (H^r + E^r)\Delta s^r = H^r\Delta s^r + a(uu^T)\Delta s^r \tag{5.52}$$

Rearranging (5.52) to make *u* the subject of the formula gives

$$u = \frac{\Delta s^r - H^r\Delta s^r}{au^T\Delta s^r} \tag{5.53}$$

Taking *a* as

$$a = \frac{1}{u^T\Delta s^r} \tag{5.54}$$

Equation (5.53) becomes

$$u = \Delta s^r - H^r \Delta s^r \tag{5.55}$$

5.7.3 Broyden-Fletcher-Goldfarb-Shanno (BFGS) Method

The BFGS method relies on adding a correction matrix as in the case of the Rank One method. However, in this case a rank two correction matrix is used [46]. The matrix *E* is required to be symmetric and is written in the form of:

$$\begin{aligned} E^r &= v(av + bw)^T + w(bv + cw)^T \\ &= avv^T + b(vw^T + wv^T) + cww^T \end{aligned} \tag{5.56}$$

where *v* and *w* are linearly independent vectors and *a, b* and *c* are scalars.

Substituting Equation (5.45) and (5.56) into Equation (5.51) gives:

$$\Delta^r - H^r \Delta s^r = ((av + bw)^T \Delta s^r)v + ((bv + cw)^T \Delta s^r)w \tag{5.57}$$

The left side is a linear combination of Δ^r and $H^r \Delta s^r$. The right side is a linear combination of *v* and *w*. Therefore the two vectors can be taken as

$$v = \Delta^r \tag{5.58}$$

$$w = H^r \Delta s^r \tag{5.59}$$

Defining *a* and *b* as shown in Equation (5.60) and (5.61)

$$a = ((\Delta)^T \Delta s^r)^{-1} \tag{5.60}$$

$$b = -((\Delta s^r)^T H^r \Delta s^r)^{-1} \tag{5.61}$$

and setting $c = 0$, Equation (5.57) can be written as

$$\Delta^r - H^{r+1} = H^r + \left(1 + \frac{w^T \Delta s^r}{v^T \Delta s^r}\right)\frac{vv^T}{v^T \Delta s^r} - \frac{vw^T + wv^T}{v^T \Delta s^r}(1 + \frac{w^T \Delta s^r}{v^T \Delta s^r}) \tag{5.62}$$

5.7.4 Fletcher-Reeves Method

The Fletcher-Reeves method uses only the gradient of the function together with a positive definite quadratic function to locate a minimiser in a finite number of iterations and is a type of line search method [53]. It has the property that, when applied to the quadratic function where A is a positive definite symmetric matrix, the successive search directions are conjugate with respect to A.

Using a quadratic function to describe the gradient of f, the derivative of f can be written as

$$\nabla f(X) = AX + a \tag{5.63}$$

For a line search starting in the direction of q the gradient of function f becomes

$$\nabla f(X + mq) = A(X + mq) + a = \nabla f(X) + mAq \tag{5.64}$$

Also

$$q^T \nabla f(X + mq) = A(X + mq) + a = q^T \nabla f(X) + mq^T Aq \tag{5.65}$$

From Equation (5.65), the right side can be reduced to zero by taking *m* as follows

$$m = -\frac{q^T \nabla f(X)}{q^T Aq} \tag{5.66}$$

Substituting Equation (5.66) into Equation (5.65) gives

$$q^T \nabla f(X + mq) = 0 \tag{5.67}$$

Equating *g* to be equal to $q^T \nabla f(X + mq)$, Equation (5.64) can be written as

$$g^{r+1} = g^r + m^r Aq^r \tag{5.68}$$

where *g* is given by Equation (5.67).

$$m = -\frac{q^{r^T} g^r}{q^{r^T} Aq^r} \tag{5.69}$$

Substituting Equation (5.66) into Equation (5.68) gives

$$g^{r+1} = g^r + -\frac{q^{r^T} g^r}{q^{r^T} Aq^r} Aq^r \tag{5.70}$$

The search directions for the Fletcher-Reeves method are specified by applying a scalar quantity u to the steepest search direction $q^{r+1} = -g^{r+1}$. The scalar quantity is added to g^{r+1} in such a way that the successive search directions are conjugate to A.

The search direction therefore can be written as

$$q^{r+1} = -g^{r+1} + u^r q^{r^T} \tag{5.71}$$

where

$$u^r = \frac{g^{r+1^T} A q^r}{q^{r^T} A q^r} \tag{5.72}$$

Therefore, to find a local minimiser for a function f of several variables using the Fletcher-Reeves method, the following is done

(a) the starting vector is x^0 is determined, taking $q^0 = -\nabla f(x^0)$ and $r = 0$.

(b) the value of m which minimises $f(x_i + mq_i)$ along the line $x_i + mq_i$ is calculated. If the sequence of iterations has converged to the desired accuracy, or is clearly not converging, the search is stopped.

(c) the new search directions are computed from Equation (5.71) which can be written as

$$q^{r+1} = -\nabla f\left(X^{r+1}\right) + \frac{\nabla f\left(X^{r+1}\right)^T \nabla f\left(X^{r+1}\right)}{\nabla f\left(X^r\right)^T \nabla f\left(X^r\right)} q^r \tag{5.73}$$

(d) the iteration counter r is set to r+1.

5.7.5 Rosenbrock Algorithm

The Rosenbrock algorithm is a 0^{th} order form of numerical optimisation meaning that no derivatives of the objective function are required in any of the optimisation strategies employed [54]. The optimisation strategies, used in the algorithm iteration cycles, are based on the features of the one variable optimisation methods presented in Section 5.3. The first optimisation strategy incorporated is that the algorithm uses predetermined step sizes similar to the Interval Reduction, Grid Search and Golden Section Search methods discussed in Sections 5.3.2, 5.3.3 and 5.3.4. The next optimisation strategy is that the algorithm uses alternating search steps during the minimisation stage of the objective function, similar to the Alternating Variables method presented in Section 5.5.1. The last optimisation strategy incorporated is that the Rosenbrock algorithm uses orthogonal vectors to determine the new search direction steps when starting a new iteration cycle. In calculating orthogonal vectors, the algorithm takes advantage of the concept of finding the steepest descent direction without having to calculate the objective function derivatives. Thus, the Rosenbrock algorithm, whilst a 0^{th} order optimisation method itself, utilises the benefits of the 1^{st} order optimisation methods.

5.7.5.1 Search Strategy in an Iteration Cycle

The Rosenbrock algorithm uses predetermined step sizes and search directions at the start of an iteration cycle. However, the algorithm has an advantage over the conventional one variable optimisation methods in that the widths of the steps are varied during each search in a given direction.

The concept of alternating the search directions is derived from considering the function variables to be a base of vectors in an N-dimensional coordinate system where N is the number of function variables. The first search is conducted along a line parallel to the x_1-axis, the second search along a line parallel to the x_2-axis, the third search along a line parallel to the x_3-axis until the search along the x_N-axis is made and one search cycle is completed.

The width of the steps in the search direction of a given vector is determined by initially trying a step of arbitrary size. If this succeeds in yielding a lower value of the function, the step width is multiplied by a positive number greater than one. In the case of a failure, the step width is multiplied by a negative number between 0 and 1. Each step made in the direction of the vectors is called a trial.

The alternating searches are repeated from x_1 to x_N until at least one trial has been successful in each direction, and one has failed. A new set of directions for the vectors is then calculated. The set of trials made with one set of directions, and the subsequent change of these directions is known as an iteration cycle.

5.7.5.2 Changing Search Direction Vectors

As discussed in Section 5.7.5.1, a new set of direction vectors is calculated at the end of an iteration cycle. The new set of directional vectors should be orthogonal to the current set of vectors. This ensures the new vectors are in the most likely steepest descent direction.

It is worth noting that derivative based optimisation methods such as the Newton Raphson method calculate the steepest descent direction by finding the objective function derivative.

The Rosenbrock algorithm being an 0^{th} order optimisation method does not use derivatives but instead uses the Gram-Schmidt procedure to orthogonalize the existing set of direction vectors. Using this procedure a new set of direction vectors q_1 to q_N can be found by orthogonalizing the multidimensional vectors x_1 to x_N of the current iteration cycle.

The first step required to find the new set of search direction vectors using the Gram-Schmidt procedure is to normalise vector x_1 using Equation (5.74)

$$q_1 = \frac{1}{\sqrt{x_1^T x_1}} x_1 \tag{5.74}$$

To find q_2, the projection q_1 to x_2 is subtracted from x_2 as shown in Equation (5.75)

$$q_2 = x_2 - \left(x_2^T q_1\right) q_1 \tag{5.75}$$

and then normalised using Equation (5.76)

$$q_2 = \frac{1}{\sqrt{q_2^T q_2}} q_2 \tag{5.76}$$

To find the next orthogonal vector, q_3, the projections q_1 to x_3 and q_2 to x_3 are both subtracted from x_3 as shown in Equation (5.77)

$$q_3 = x_3 - \left(x_3^T q_1\right) q_1 - \left(x_3^T q_2\right) q_2 \tag{5.77}$$

and then normalised using Equation (5.78)

$$q_3 = \frac{1}{\sqrt{q_3^T q_3}} q_3 \tag{5.78}$$

The procedure is carried out in this manner until the Nth orthogonal vector q_N has been calculated.

To illustrate how the Gram-Schmidt algorithm works, the steps for calculating a set of orthogonal vectors q_1 and q_2 from any two basis vectors x_1 and x_2 are shown in Figure 5-5. The two basis vectors x_1 and x_2, from which the orthogonal vector will be calculated, are shown in light green and light blue. First of all, the basis vector x_1 is normalised using Equation (5.74). The resulting vector is the first orthogonal vector q_1 which is shown in red. The projection to the next basis vector, x_2 from the normalised vector q_1 is shown by the dashed red line. Subtracting the projection q_1 to x_2 from x_2 using Equation (5.75) gives the vector indicated by the purple arrow. Normalising this purple vector using Equation (5.76) gives the second orthogonal vector q_2 which is shown in dark blue.

5.8 Conclusion

In this chapter the different optimisation methods for finding the minimum value of a single variable, two variable and multiple variable function have been identified. These methods of optimisation can offer an alternative to the analytical methods discussed in Chapter 4 for investigating the problem of leaks in a duct. The reason for using this alternative approach has been motivated by the need to find solutions to the limitations encountered when applying analytical methods to the problem of investigating leaks in a

duct. The main limitation of the analytical method is the inability to extend the method to the investigation of multiple leaks as suitable mathematical expressions are non existent and complicated.

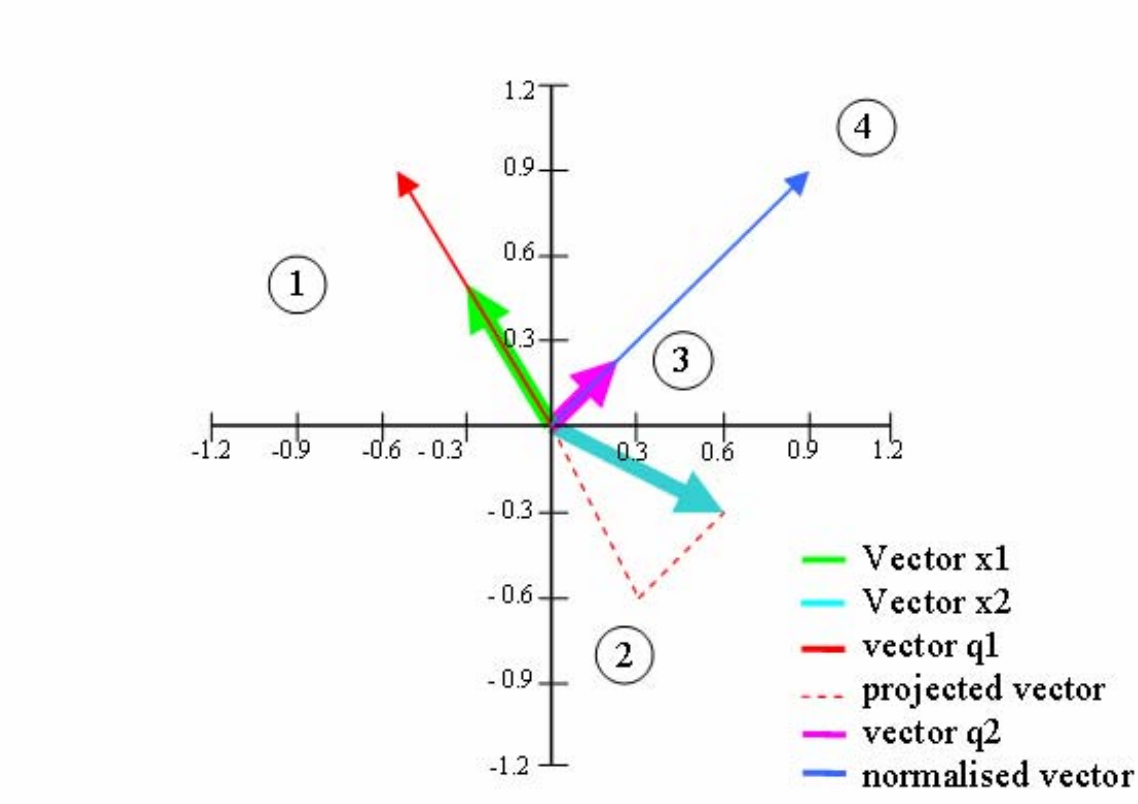

Figure 5-5: Steps for calculating orthogonal vectors from a set of base vectors

The other limitation is that, though analytical methods were successfully applied to the investigation of single leaks in a duct, there still remained room for improvement in the accuracy of the solutions. Therefore, application of optimisation methods to the problem of detecting, locating and finding the size of one or more leaks in a cylindrical pipe follows in the next two chapters.

Chapter 6

Investigating a Single Leak in a Cylindrical Duct using Numerical Optimisation

In this chapter, the methods of optimisation discussed in Chapter 5 are applied to the problem of locating and sizing a single leak in a cylindrical duct. Although analytical methods for investigating single leaks were successfully employed in Chapter 4, it is still instructive to apply the optimisation approach to the simple case of a single leak. Primarily, it enables the success of the optimisation approach to be evaluated. In particular, the accuracy of hole size/location predictions made using optimisation methods can be compared with the accuracy achieved using analytical methods.

Optimisation methods that enable a function with one variable to be minimised can be used to predict either the size of a single leak given its location or the location of a single leak given its size. The objective function is derived from the input impedance expressions introduced in Chapter 2, with the function minimiser being either the hole size or the hole position. Over the coming sections, two dimensional plots are displayed which show the relationship between the function and minimiser values. The results of using the single-variable Newton Raphson method, the Grid Search method and the Golden Section Search method to predict either the size or the position of a single hole in a cylindrical duct are also presented.

Optimisation methods that enable a function with two variables to be minimised can be used to predict both the size and the location of a single leak in one go. Again, the

objective function is derived from the input impedance expressions of Chapter 2. However, in this case, there are two function minimisers – the hole size and the hole position. Three dimensional plots are presented which show the relationship between the function value and the two minimiser values. The Alternating Variables method and the Steepest Descent method are then used to locate and size a single leak in a cylindrical duct. When employing the Alternative Variables method, the Grid Search method is used to find the local minimiser in the selected search direction and minimiser interval. In the case of the Steepest Descent method, the Newton Raphson method is used to find the local minimiser.

6.1 Objective Function

The objective function that is to be optimised is defined in such a way that, when it is minimised, the optimised parameters are close to the solution being sought. When investigating leaks in a duct, the objective function can be expressed as

$$f(x_i) = \sum_{i=4}^{40} \left| z_{in(\exp)}(48.83i) - z_{in(\mathrm{mod})}(x_i, 48.83i) \right| \tag{6.1}$$

where $z_{in(exp)}$ is the target function which is the experimentally measured input impedance of the pipe containing the leaks, $z_{in(mod)}$ is the theoretical input impedance of a model duct containing side holes (the calculation of which was outlined in Chapter 2), and x_i are the function minimisers. The equation shows a subtraction between the complex values of $z_{in(exp)}$ and $z_{in(mod)}$ from which either the impedance magnitude or the impedance phase can be extracted (in this chapter the optimisations are all magnitude based but in Chapter 7 both magnitude and phase based optimisations are presented). By carrying out the summation from i = 4 to i = 40, the objective function incorporates impedance measurements over a frequency range of 195.3 Hz to 1953.1 Hz. The frequency range used

matches the range used in Chapter 4 when investigating the single leak size using analytical means. Measurements outside this range are not included as they tend to be noise affected. The frequency interval of 48.83 Hz arises because a sampling frequency of 50 kHz and a sample length of 1024 points was used for the experimental measurements (as discussed in Chapter 3).

For the case of a pipe with a single circular hole in its wall, the theoretical input impedance $z_{in(mod)}$ of the pipe depends on the total length of the pipe l, its internal diameter r, its wall thickness l_h, the distance of the hole from the pipe input l_1, and the radius of the hole r_h.

When applying one variable optimisation methods to the problem of investigating a single leak in a cylindrical pipe, all but one of the aforementioned parameters of the pipe under investigation must be known. There is only one function minimiser - either the hole position or the hole radius – and the objective function is written either as

$$f(l_1) = \sum_{i=4}^{40} \left| z_{in(\exp)}(48.83i) - z_{in(\mathrm{mod})}(l_1, 48.83i) \right| \tag{6.2}$$

or

$$f(r_h) = \sum_{i=4}^{40} \left| z_{in(\exp)}(48.83i) - z_{in(\mathrm{mod})}(r_h, 48.83i) \right| \tag{6.3}$$

In the case that the size of the hole is known but its position is to be found, Equation (6.2) is used. The hole position l_1 is set to an arbitrary value. All the other parameters of the duct model are set equal to those of the duct under investigation. The optimisation routine then adjusts the value of l_1 until the objective function f is equal to zero (to within pre-specified bounds).

If the hole position is known but its size is unknown, Equation (6.3) is used. In this case, the hole radius r_h is assigned an arbitrary value while all the other parameters of the duct model are set equal to those of the duct under investigation. The optimisation routine then adjusts the value of r_h until the objective function f is equal to zero (again to within pre-specified bounds).

When applying two variable optimisation methods to a cylindrical pipe containing a single leak, there are two function minimisers; the hole position and the hole radius. All the other parameters of the pipe under investigation must be known. The objective function is written as

$$f(l_1, r_h) = \sum_{i=4}^{40} \left| z_{in(\exp)}(48.83i) - z_{in(\mathrm{mod})}(l_1, r_h, 48.83i) \right| \tag{6.4}$$

Both the hole position l_1 and the hole radius r_h are assigned arbitrary values. All the other parameters of the duct model are set equal to those of the duct being investigated. The optimisation routine then adjusts the values of both l_1 and r_h in Equation (6.4) until the objective function f is equal to zero (to within pre-specified bounds).

6.2 One Variable Objective Function

6.2.1 Variation of Objective Function with Hole Radius

The response of the objective function described by Equation (6.3) in Section 6.1 to a change in the hole radius can be observed by plotting the values of the objective function as the hole radius is varied. This requires all the possible values of the objective function within the specified range of the function minimiser to be evaluated and plotted.

Optimisation methods discussed later in the chapter seek to find ways of discovering the function minimum without having to calculate all the possible values of the objective function as the minimiser is varied. In this way, they aim to achieve a reduction in the computational load. The advantage of plotting the objective function values as the minimiser is varied is that it gives an easy way of observing the behaviour of the objective function, from which information necessary to apply the more complicated methods can be deduced.

To investigate the effect of varying the hole radius, the fixed parameters of the theoretical model in Equation (6.3) were set as l_h = 1 mm, r = 5.0 mm, l_1 = 0.32 m and l_2 = 0.198 m to match the dimensions of the first cylindrical pipe introduced in Chapter 4. The experimental input impedance for the pipe with a hole of radius 2 mm was taken as the target function, $z_{in(exp)}$. The hole radius r_h of the theoretical model was varied from 0.01 mm to 5 mm over the frequency range of 195.3 Hz to 1953.1 Hz and the different values of $z_{in(mod)}$ were calculated. The values of the objective function were then determined and plotted. Figure 6.1 shows the resultant plot of the objective function using the experimental input impedance of the cylindrical pipe with 2 mm radius sidehole. The graph therefore shows the magnitude of the difference between $z_{in(\exp)}$ and $z_{in(\mathrm{mod})}$ summed over the frequency range of 195.3 Hz to 1953.1 Hz plotted against the variation in the hole radius (as stated in the objective function of Equation 6.3).

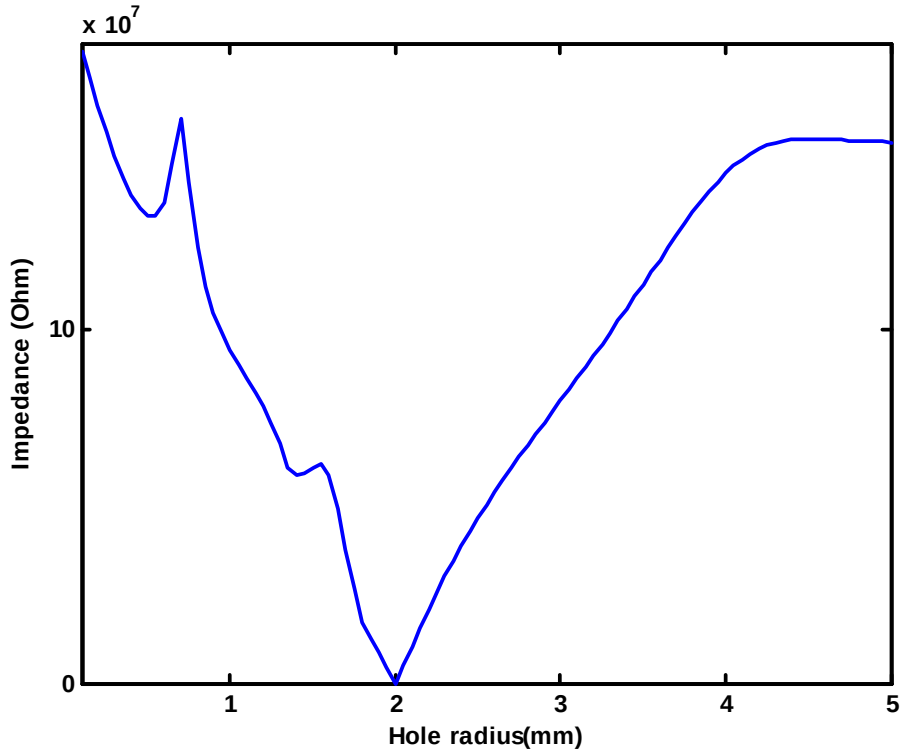

Figure 6-1: Plot of the objective function variation with hole radius for cylindrical pipe 1 with side hole of 2mm

Examination of Figure 6-1 shows that the objective function is close to zero at the minimiser value of 2 mm. Therefore, the objective function gives a correct prediction for the hole radius of 2 mm. It can also be observed from Figure 6-1 that there are two local minima in the plot of the objective function at the minimiser values of approximately 0.4 mm and 1.3 mm. Therefore the value of the objective function at the minimser value of 2 mm is really a global minimum of the objective function.

6.2.2 Variation of Objective Function with Hole Position

It is also possible to plot the response of the objective function to a change in the hole position following the procedure discussed in Section 6.2.1. To demonstrate this, the fixed parameters of the theoretical model in Equation (6.2) were set as l = 0.5 m, l_h = 1 mm, r = 5.0 mm, r_h = 2 mm. The theoretical input impedance values, $z_{in(mod)}$, were calculated by varying l_1, the hole location from the start of the cylindrical pipe. The position of the hole from the end of the cylindrical pipe l_2 was defined as $l_2 = l - l_1$. The target function was again set equal to the experimental input impedance of the first cylindrical pipe with a 2 mm radius sidehole. Figure 6-2 shows the plot of the objective function using this target function.

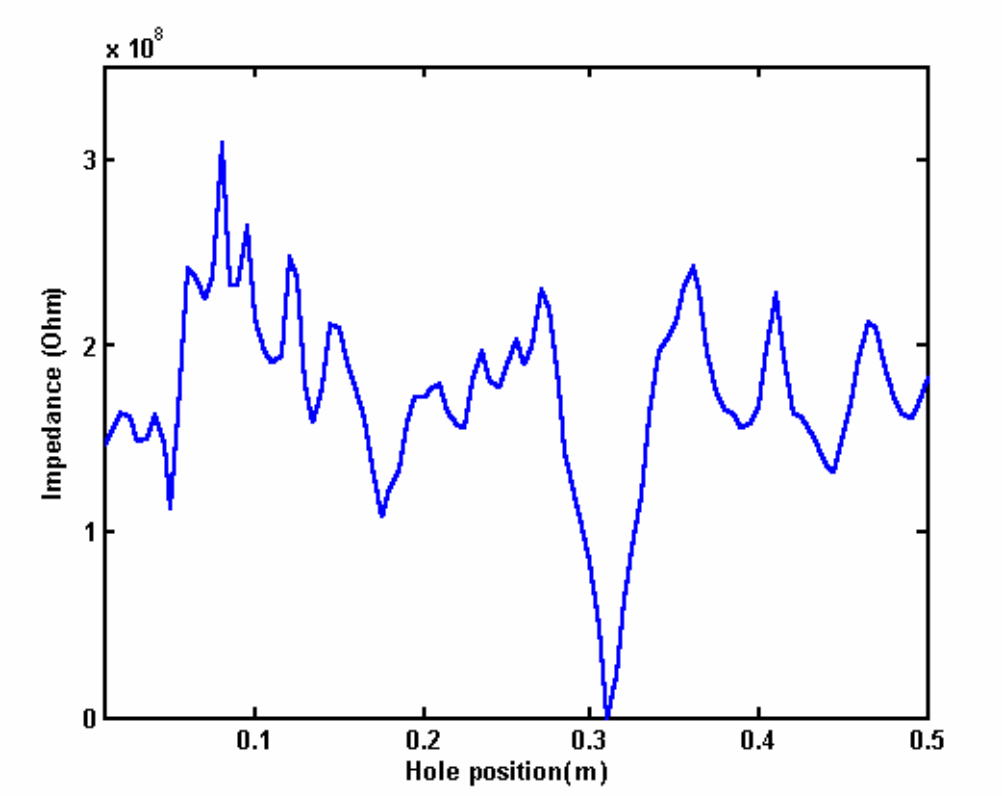

Figure 6-2: Plot of the objective function variation with hole position for cylindrical pipe 1 with side hole of 2 mm

It can be seen from Figure 6-2 that the value of the objective function is close to zero at the minimiser value of 0.31 m. As such it can be concluded that the objective function gives the correct prediction of the hole position. However, it can also be noted from Figure 6-2 that there are several positions of local minima in the plotted objective function. Indeed, the objective function when plotted against hole position variation tends to show a more rugged plot than when it is plotted against hole radius variation (see Figure 6-1).

6.3 Application of One Variable Optimisation Methods

Optimisation methods provide a way of finding the minimum of the objective function without having to calculate all the function values (as was the case when plotting the values of the objective function in Section 6.2). In this section, the one variable optimisation methods discussed in Chapter 5 are applied to the prediction of either the size or the location of a single hole in the side of a cylindrical pipe.

One variable optimisation methods work by reducing the objective function to a value close to zero. The value of the minimiser at this low value of the objective function should correspond to the correct prediction of either the hole size or hole position depending on which parameter of the leak is being investigated.

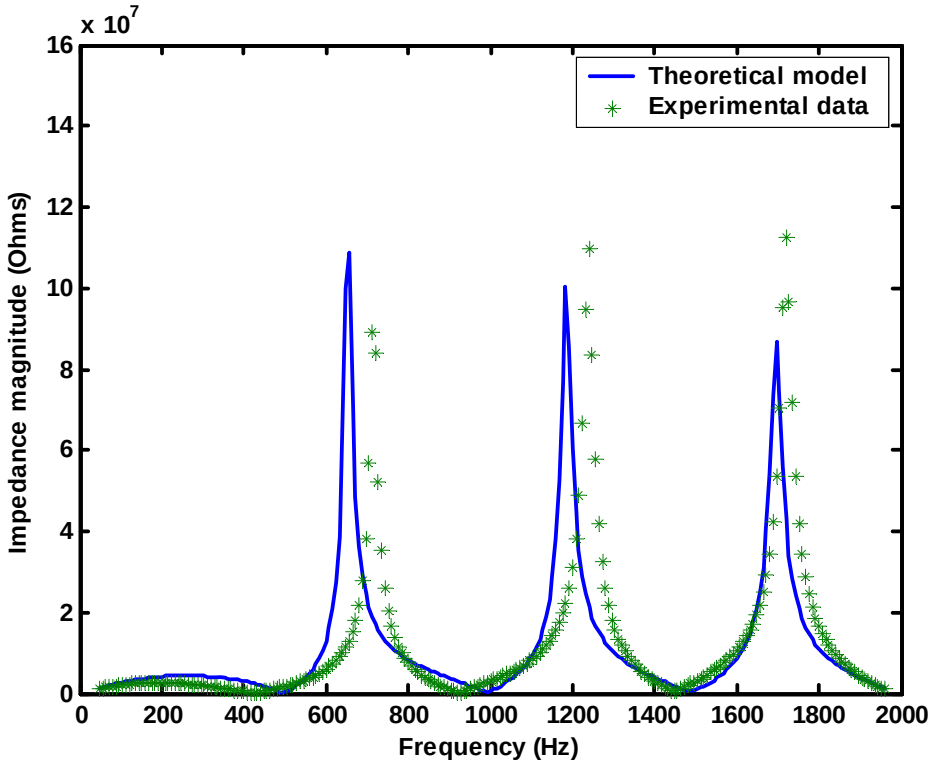

Figure 6-3: Comparison of the start and target impedances when searching for the hole size (start value of rh = 0.1 mm)

When implementing the one variable optimisation methods, the hole radius or the hole position in the theoretical model must be given an arbitrary start value; For the optimisation methods presented in this section, the start value of the hole radius was taken as 0.1 mm whilst the start value of the hole position was taken as 0.1 m.

As in Section 6.2, the test object was chosen to be the cylindrical pipe with parameters l_h = 1 mm, r = 5 mm, r_h = 2 mm, l_1 = 0.32 mm and l_2 = 0.198 mm. The experimentally measured input impedance of the pipe was taken as the target value for the optimisation. The start value for the optimisation routine was found by calculating the theoretical impedance of the pipe with the same parameters as above except that r_h was set at 0.1 mm for the case of finding the hole size and l_1 was set at 0.1 m (with $l_2 = 1 - l_1$) for the case of finding the hole position. Figure 6-3 shows a comparison of the start and target impedances

when searching for the hole size. Similarly, Figure 6-4 shows the start and target impedances when searching for the hole position.

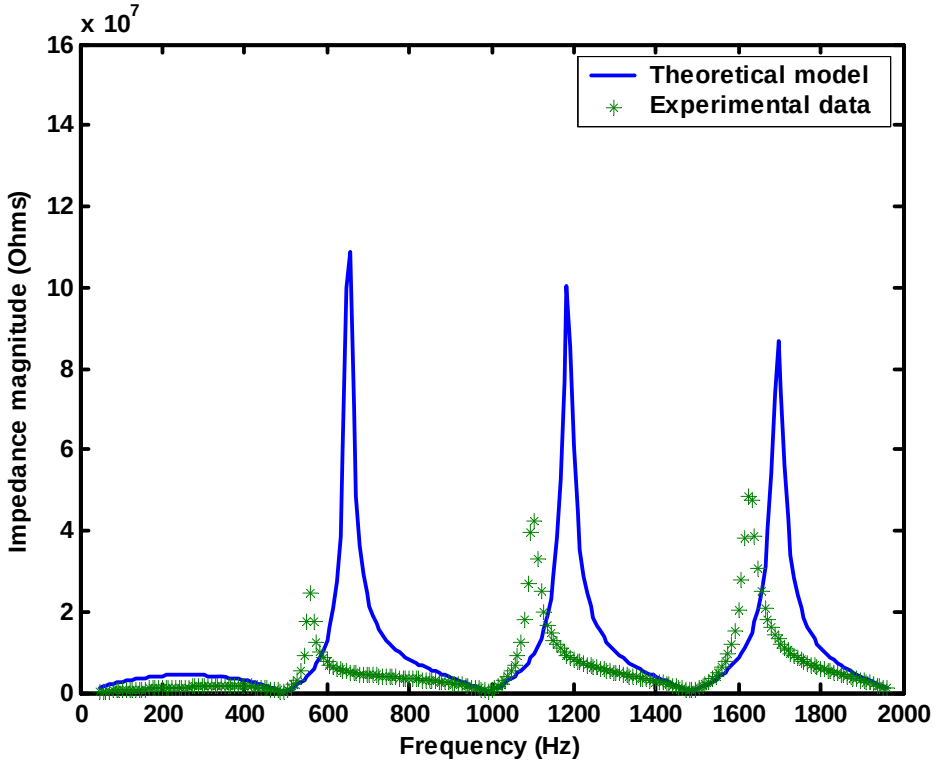

Figure 6-4: Comparison of the start and target impedances when searching for the hole position (start value of l1 = 0.1 m)

It can be seen, from both Figure 6-3 and Figure 6-4, that the start value of the theoretical impedance doesn't provide a good match with the experimentally measured target impedance. The optimisation methods discussed in the following sections work by varying either the hole radius or the hole position until a match in the two impedances is achieved.

6.3.1 Application of the Grid Search Method

The Grid Search method, whose theory was presented in Section 5.3.3, is implemented here for the purpose of predicting the hole size and hole position. The computer program to implement the Grid Search method was written in Mathcad and variables were defined to store information on the following; boundary values *a* and *b* for the initial minimiser

interval, the number of iterations *it* and the function evaluations *eval.* The method terminates when the local minimiser is known to be within distance ε of the current iterate.

6.3.1.1 Predicting Hole Size

The initial interval boundaries were set as 0.1 mm to 9 mm and an initial hole radius of 0.5 mm was used. The stopping tolerance ε was set as 0.05 mm so that the final radius prediction would agree with the physical measurement to within 2.5 %. Step sizes of 0.001 mm were used within each of the iteration stages. The step size was chosen so that it was small enough to operate within the stopping tolerance of 0.05 mm. Too large a step size would result in the local minimum point being missed and the optimisation routine would not exit.

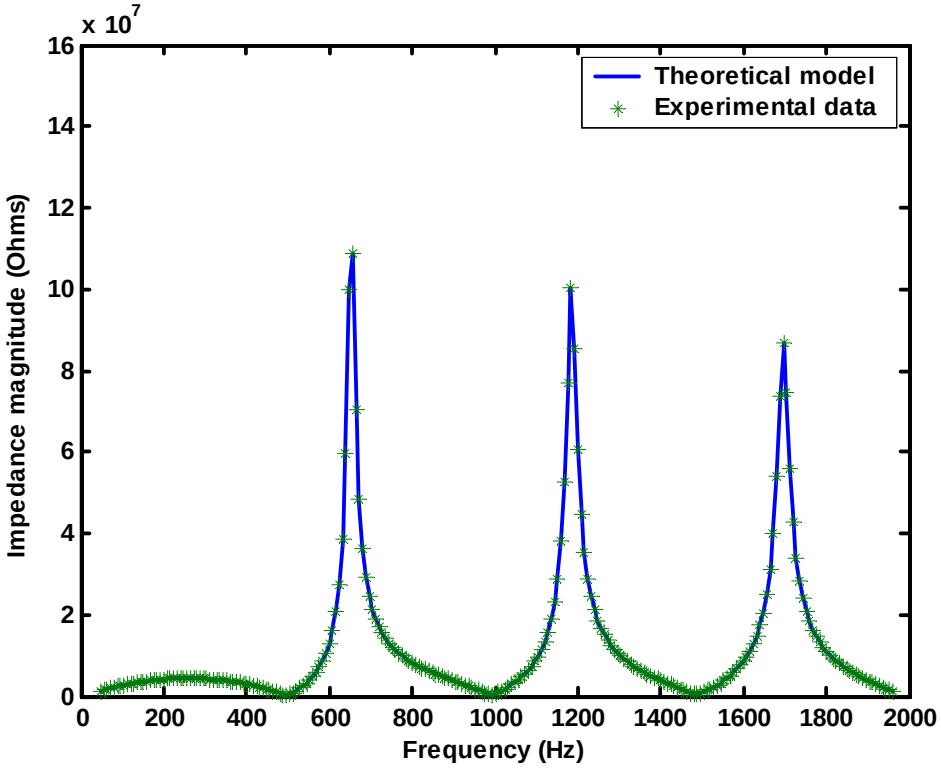

Figure 6-5: Comparison of the final impedance (after optimisation of the hole size using the Grid Search method) and the target impedance

The objective function described in Equation (6.3) was then optimised using the Grid Search method until the difference between the local minimiser and the current iterate was within the set stopping tolerance of 0.05 mm. Figure 6-5 shows a comparison of the final value of the input impedance of the duct model after optimisation and the experimentally measured target impedance. Examination of Figure 6-5 reveals that the two input impedance curves are now in good agreement.

The values of the physically measured hole radius (parameter target value), the initial start value of the minimiser (parameter start value) and the final minimiser value (optimised parameter value) are shown in Table 6-1. The percentage difference between the parameter target value *(TV)* and optimised parameter value *(OV)* is also presented, together with the number of iterations (*it*) and function evaluations (*eval*).

It can be seen from Table 6-1 that, after 7 iterations and 12 function evaluations, the predicted hole radius was 2.021 mm. This agrees with the actual hole radius of 2.00 mm to within 1.05%.

a (mm)	*b* (mm)	Parameter target value *(TV)* (mm)	Parameter start value *(SV)* (mm)	Optimised parameter Value *(OV)* (mm)	*it*	*eval*	$\frac{\lvert TV-OV\rvert}{TV}\times 100$ (%)
0.100	9.000	2.000	0.500	2.021	7	12	1.05

Table 6-1: Hole radius predictions with associated accuracies for cylindrical pipe 1 with 2 mm radius leak using the Grid Search method

6.3.1.2 Predicting Hole Position

The initial interval boundaries were set as 0.01 m to 0.4 m and an initial hole position of 0.15 m was used. The stopping tolerance was set as 0.005 m so that the hole position prediction would agree with the physical measurement to within 2 %. Step sizes of 0.001 m were used within each of the iteration stages. The step size was chosen so that it was small enough to operate with in the stopping tolerance of 0.005 m. Too large a step size would result in the local minimum point being missed and the optimisation routine not stopping as discussed previously.

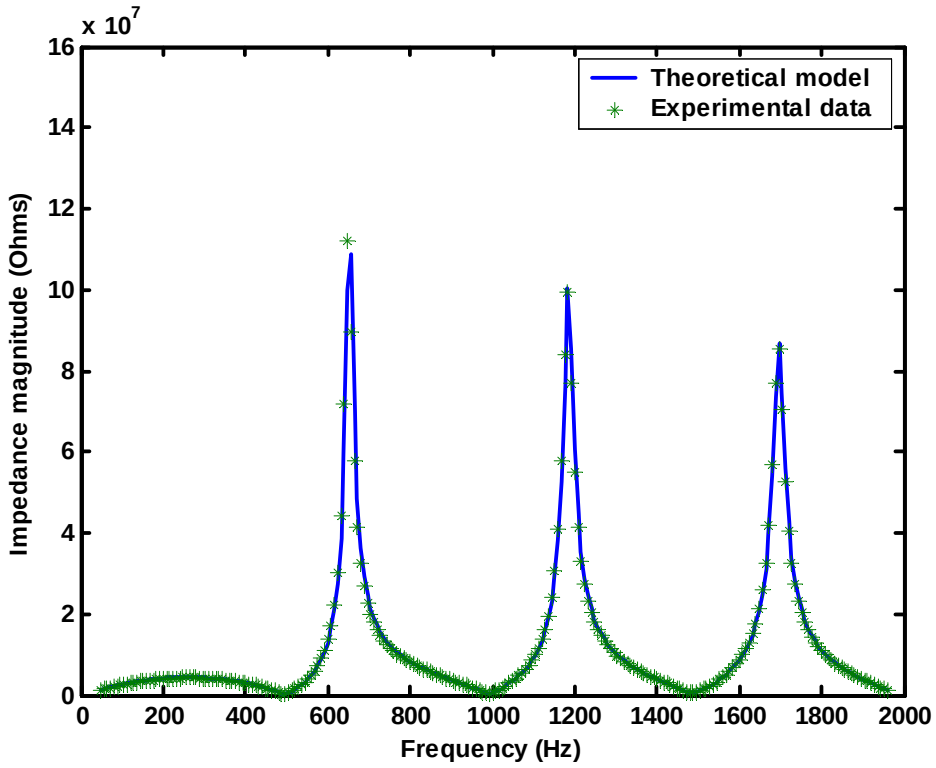

Figure 6-6: Comparison of the final impedance (after optimisation of the hole position using the Grid Search method) and the target impedance

The objective function described in Equation (6.2) was optimised until the difference between the local minimiser and the current iterate was within the set stopping tolerance of 0.005 m. Figure 6-6 compares the final value of the input impedance of the theoretical

model after optimisation with the experimentally measured target. It can be seen that the two input impedances are now closely matching.

The values of the physically measured hole position (parameter target value), the initial start values of the minimiser (parameter start value) and the final minimiser value (optimised parameter value) are shown in Table 6-2. The percentage difference between the parameter target value *(TV)* and optimised parameter value *(TV)* are also presented together with the number of iterations (*it*) and function evaluations (*eval*).

It can be seen from Table 6-2, that after 7 iterations and 12 function evaluations, the predicted hole position was 0.313 m. This agrees with the actual hole position of 0.310 m to within 0.967 %.

a (m)	*b* (m)	Parameter target value *(TV)* (m)	Parameter start value *(SV)* (m)	Optimised parameter Value *(OV)* (m)	*it*	*eval*	$\frac{\lvert TV - OV \rvert}{TV} \times 100$ (%)
0.010	0.400	0.310	0.150	0.313	12	17	0.967

Table 6-2: Hole position predictions with associated accuracies for cylindrical pipe 1 with 2 mm radius leak using the Grid Search method

6.3.2 Application of the Golden Section Search Method

The Golden Section Search method, discussed in Section 5.3.4, uses less iterations and function evaluations than the Grid Search method. The method is therefore a potentially more attractive alternative to the Grid Search method. This section discusses the application of the Golden Section Search method to the prediction of either the hole size or the hole position.

6.3.2.1 Predicting Hole Size

As with the Grid Search method, the initial interval boundaries were set as 0.1 mm to 9 mm and an initial hole radius of 0.5 mm was used. The stopping tolerance was set as 0.05mm so that the radius prediction would agree with the physical measurement to within 2.5 %. Step sizes of 0.001 mm were used within each of the iteration stages. The step size was chosen so that it was small enough to operate within the stopping tolerance of 0.05 mm.

The objective function described in Equation (6.3) was then optimised until the difference between the local minimiser and the current iterate was within the set stopping tolerance of 0.05 mm. Figure 6-7 shows a comparison of the final value of the input impedance of the duct model after optimisation and the experimentally measured target impedance. Examination of Figure 6-7 reveals that the theoretical input impedance and experimental impedance curves are now closely matching.

The values of the physically measured hole radius (parameter target value), the initial start values of the minimiser (parameter start value) and the final minimiser value (optimised parameter value) are shown in Table 6-3. The percentage difference between the parameter target value *(TV)* and optimised parameter value *(TV)* are also presented together with the number of iterations (*it*) and function evaluations (*eval*).

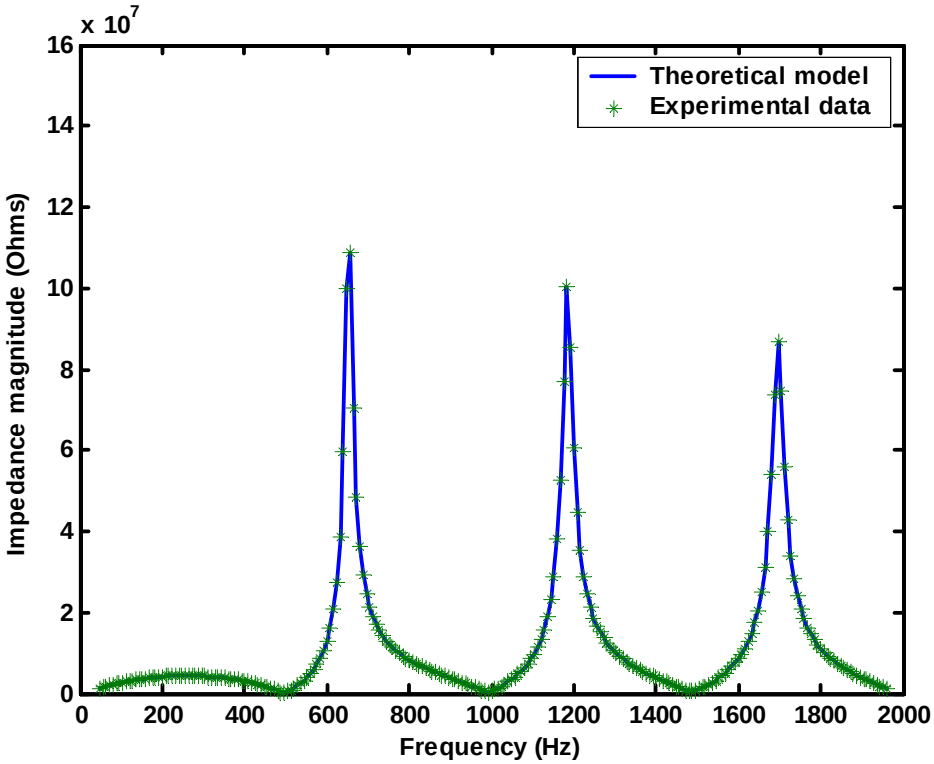

Figure 6-7: Comparison of the final impedance (after optimisation of the hole size using the Golden Section Search method) and the target impedance

From Table 6-3, it can be seen that the Golden Section Search method predicted the hole radius to be 2.036 mm. This agrees with the actual hole radius of 2.00 mm to within 1.8%**.** It can also be seen that the prediction was arrived at after 6 iterations and 9 function evaluations.

As expected the Golden Section Search method arrived at a solution with fewer iterations and function evaluations than the Grid Search Method. However, the accuracy of the predictions was not quite as good as that provided by the Grid Search method. The reason for this is that the Golden Section Search method generally takes larger iteration intervals than the Grid Search method. Large iteration intervals are more useful for separating a global minimum, where the function being evaluated shows several local minima, but tend to give poorer prediction results than methods utilising smaller iteration interval sizes.

a (mm)	*b* (mm)	Parameter target value *(TV)* (mm)	Parameter start value *(SV)* (mm)	Optimised parameter Value *(OV)* (mm)	*it*	*eval*	$\frac{\lvert TV - OV \rvert}{TV} \times 100$ (%)
0.100	9.000	2.000	0.500	2.036	6	9	1.8

Table 6-3: Hole radius predictions with associated accuracies for cylindrical pipe 1 with 2 mm radius leak using the Golden Section Search method

6.3.2.2 Predicting Hole Position

The initial interval boundaries were set as 0.01 m to 0.4 m and an initial hole position of 0.15 m was used. The stopping tolerance was set as 0.005 m so that the hole position prediction would agree with the physical measurement to within 2 %. Step sizes of 0.001 m were used within each of the iteration stages. The step size was chosen so that it was small enough to operate within the stopping tolerance of 0.005 m.

The objective function described in Equation (6.2) was optimised until the difference between the local minimiser and the current iterate was within the set stopping tolerance of 0.005 m. Figure 6-8 compares the final value of the input impedance of the theoretical model after optimisation with the experimentally measured target impedance. It can be seen that the two input impedances are now in good agreement.

The values of the physically measured hole position (parameter target value), the initial start values of the minimiser (parameter start value) and the final minimiser value (optimised parameter value) are shown in Table 6-4. The percentage difference between the parameter target value *(TV)* and optimised parameter value *(TV)* is also presented together with the number of iterations (*it*) and function evaluations (*eval*).

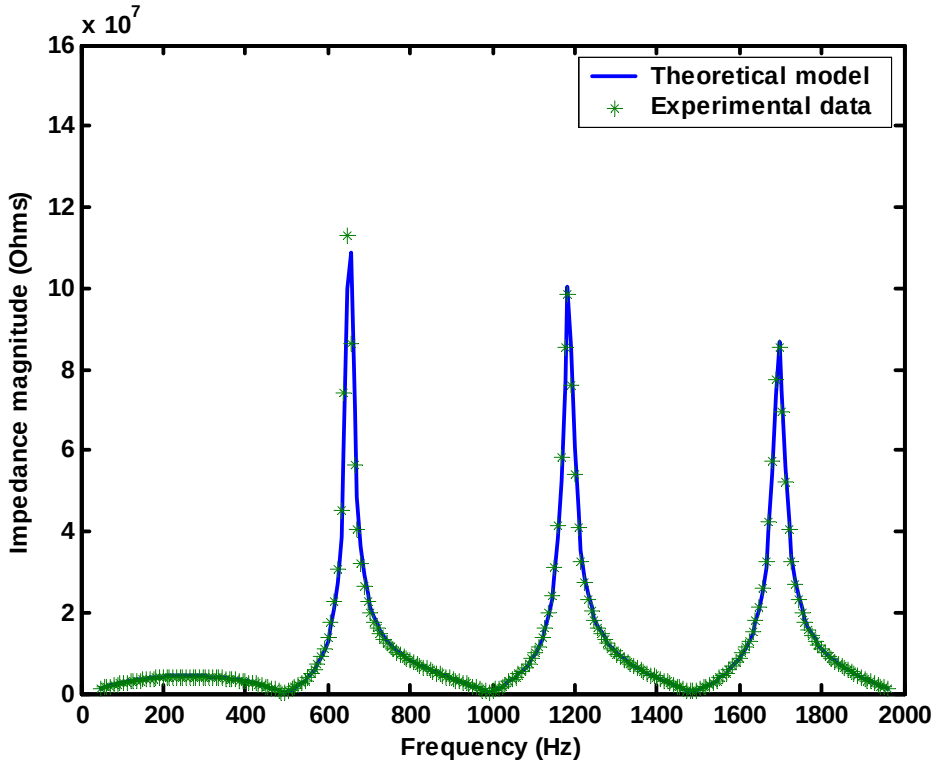

Figure 6-8: Comparison of the final impedance (after optimisation of the hole position using the Golden Section Search method) and the target impedance

From Table 6-4, it can be seen that the Golden Section Search method predicted the hole position to be 0.305 m. This agrees with the actual hole position of 0.310 m to within 1.6%**.** It can also be seen that the prediction was arrived at after 10 iterations and 16 function evaluations.

As with the prediction of hole radius, the Golden Section Search method arrived at a solution with a few iterations and function evaluations than the Grid Search method. However, again, the predictions were not quite as accurate as those provided by the Grid Search method.

a (mm)	*b* (mm)	Parameter target value *(TV)* (mm)	Parameter start value *(SV)* (mm)	Optimised parameter Value *(OV)* (mm)	*it*	*eval*	$\frac{\lvert TV-OV\rvert}{TV}\times 100$ (%)
0.010	0.400	0.310	0.150	0.305	10	16	1.6

Table 6-4: Hole position predictions with associated accuracies for cylindrical pipe 1 with 2 mm radius leak using the Golden Section Search method

6.3.3 Application of the Newton-Raphson Method

The Newton-Raphson method behaves a little differently to the methods of optimisation considered in this chapter so far. The difference in the method is that it utilises the calculated values of the objective function to determine the value of the function minimiser. The values of the objective function are used to calculate the gradient of the function from which the step size of the minimiser is determined. Therefore, boundary values for the minimiser interval are not required when using the Newton-Raphson method. It is sufficient to define the function minimiser starting value only.

As with the Grid Search and the Golden Section Search methods, the performance of the Newton Raphson method in minimising the objective function was tested using the cylindrical pipe test object. Both the hole size and then the hole position were predicted using the method.

6.3.3.1 Predicting Hole Size

The initial hole radius for the optimisation was set at 0.1 mm whilst the stopping tolerance ε for the minimiser was set as 0.05 mm (for a prediction accuracy of within 2.5 %). The maximum number of iterations was set as 1000.

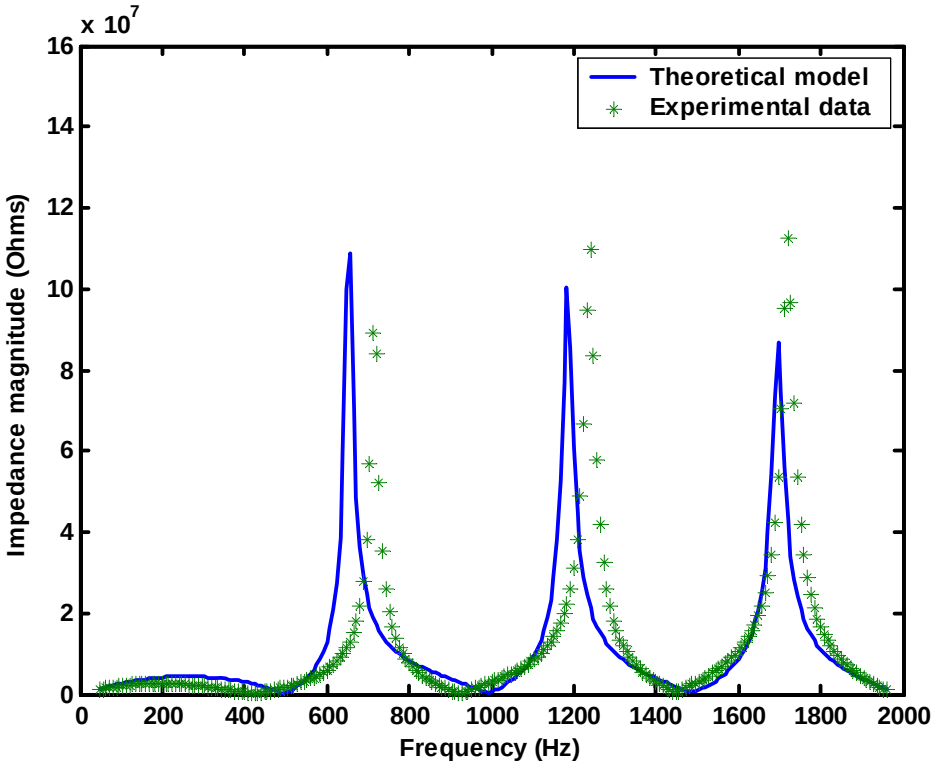

Figure 6-9: Comparison of the final impedance (after optimisation of the hole size using the Newton-Raphson method) and the target impedance

The objective function described in Equation (6.3) was optimised using the Newton-Raphson method. However, the stopping tolerances could not be reached within the specified number of iterations and the optimisation was stopped. Figure 6-9 compares the final value of the input impedance of the duct model after the optimisation was stopped with the experimentally measured target impedance. Examination of Figure 6-9 reveals that two impedances are in poor agreement.

The values of the physically measured hole radius (parameter target value), the initial start values of the minimiser (parameter start value) and the final minimiser value (optimised parameter value) are shown in Table 6-5. The percentage difference between the parameter target value *(TV)* and optimised parameter value *(TV)* is also presented together with the number of iterations (*it*) and function evaluations (*eval*).

Parameter target value *(TV)* (mm)	Parameter start value *(SV)* (mm)	Optimised parameter Value *(OV)* (mm)	*it*	*eval*	$\frac{\lvert TV - OV \rvert}{TV} \times 100$ (%)
2.000	0.100	1.4×10^{-8}	1000	2130	100

Table 6-5: Hole radius predictions with associated accuracies for cylindrical pipe 1 with 2 mm radius leak using the Newton-Raphson method

Table 6-5 shows that the agreement between the predicted radius and physically measured value is very poor. This is due to the fact that derivative based methods tend to give poor prediction results if the function being optimised is non smooth and has sudden changes in the slope or gradient of the function. From Figure 6-1, the objective function of Equation (6.3) was plotted and revealed a sharp sudden change in slope at a hole radius of approximately 0.7 mm. The slope of the function at this position is not defined. This sudden change in the slope gradient could be the reason for the breakdown in the predictions provided by the derivative based Newton-Raphson method.

6.3.3.2 Predicting Hole Position

The initial hole position for the optimisation was set at 0.1 m whilst the stopping tolerance ε for the minimiser was set as 0.005 m (for a prediction accuracy of within 2 %). The maximum number of iterations was set as 1000.

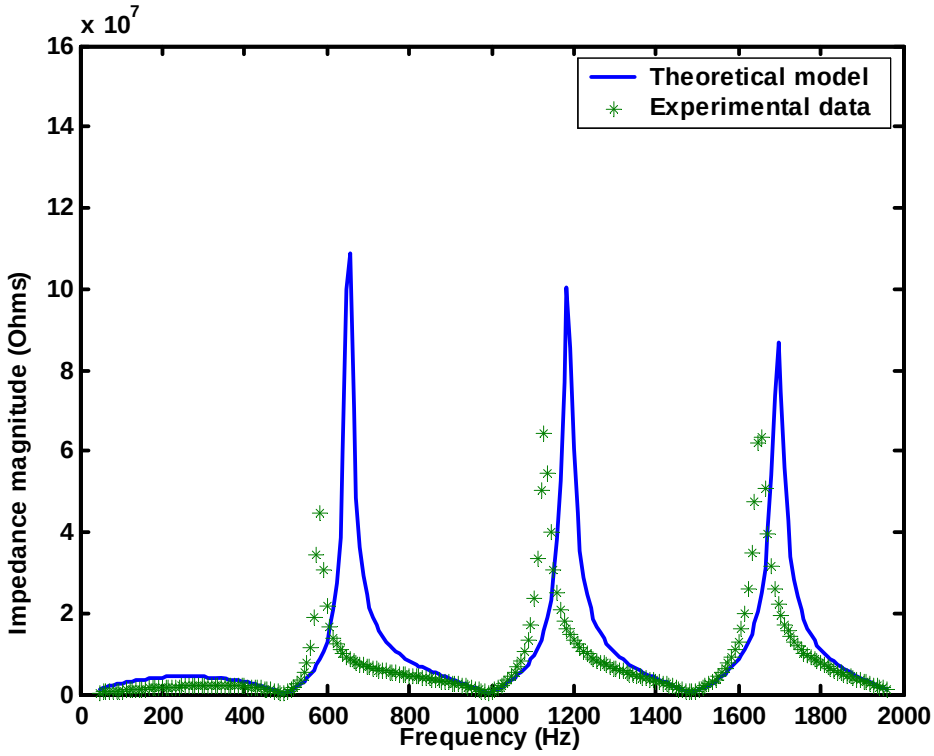

Figure 6-10: Comparison of the final impedance (after optimisation of the hole position using the Newton-Raphson method) and the target impedance

The objective function described in Equation (6.2) was optimised using the Newton-Raphson method. However, as for the hole radius prediction, the stopping tolerances could not be reached within the specified number of iterations and the optimisation was stopped. Figure 6-10 shows both the final value of the input impedance of the duct model after the optimisation was stopped and the experimentally measured target impedance. Examination of Figure 6-10 reveals that the two impedances are still in poor agreement.

The values of the physically measured hole position (parameter target value), the initial start values of the minimiser (parameter start value) and the final minimiser value (optimised parameter value) are shown in Table 6-6. The percentage difference between the parameter target value *(TV)* and optimised parameter value *(TV)* is also presented together with the number of iterations (*it*) and function evaluations (*eval*).

Parameter target value *(TV)* (m)	Parameter start value *(SV)* (m)	Optimised parameter Value *(OV)* (m)	*it*	*eval*	$\frac{\lvert TV - OV \rvert}{TV} \times 100$ (%)
0.310	0.100	0.14	1000	2340	54

Table 6-6: Hole position predictions with associated accuracies for cylindrical pipe 1 with 2 mm radius leak using the Newton-Raphson method

Table 6-6 shows that the agreement between the predicted hole position and the physically measured value is very poor. The explanation for the poor prediction is as discussed earlier. That is, derivative based methods tend to give poor optimisation results for non smooth functions. From Figure 6-2, it is clear that the objective function of Equation (6.2) has a number of sudden changes in slope at several values of hole position. These sudden changes in slope gradient are the most likely reason for the breakdown in the predictions provided by the Newton-Raphson method.

6.4 Two Variable Objective Function

The response of the objective function described by Equation (6.4) to a change in both the hole radius and hole position parameters can be observed by plotting the values of the objective function as the two parameters are varied. This requires all the possible values of

the objective function within the specified ranges of the function minimisers to be evaluated and plotted.

To investigate the effect of varying both hole radius and hole position, the cylindrical pipe test object with geometrical parameters l_h = 1 mm, r = 5.0 mm, r_h = 2 mm l_1 = 0.32 m and l_2 = 0.198 m was again used. The pipe's experimentally measured input impedance, $z_{in(exp)}$, was taken as the target function. Meanwhile, the fixed parameters of the theoretical model were set as l_h = 1 mm, r = 5.0 mm and l = 0.5 m. The hole radius r_h was then varied from 0.01 mm to 5 mm while the hole position l_1 was varied from 0.1 m to 0.4 m. For each value of r_h and l_1, the theoretical impedance of the model $z_{in(mod)}$ was calculated over the frequency range of 195.3 Hz to 1953.1 Hz. The values of the objective function were then evaluated using Equation (6.4) and plotted. The resulting three dimensional plot is shown in Figure 6-11.

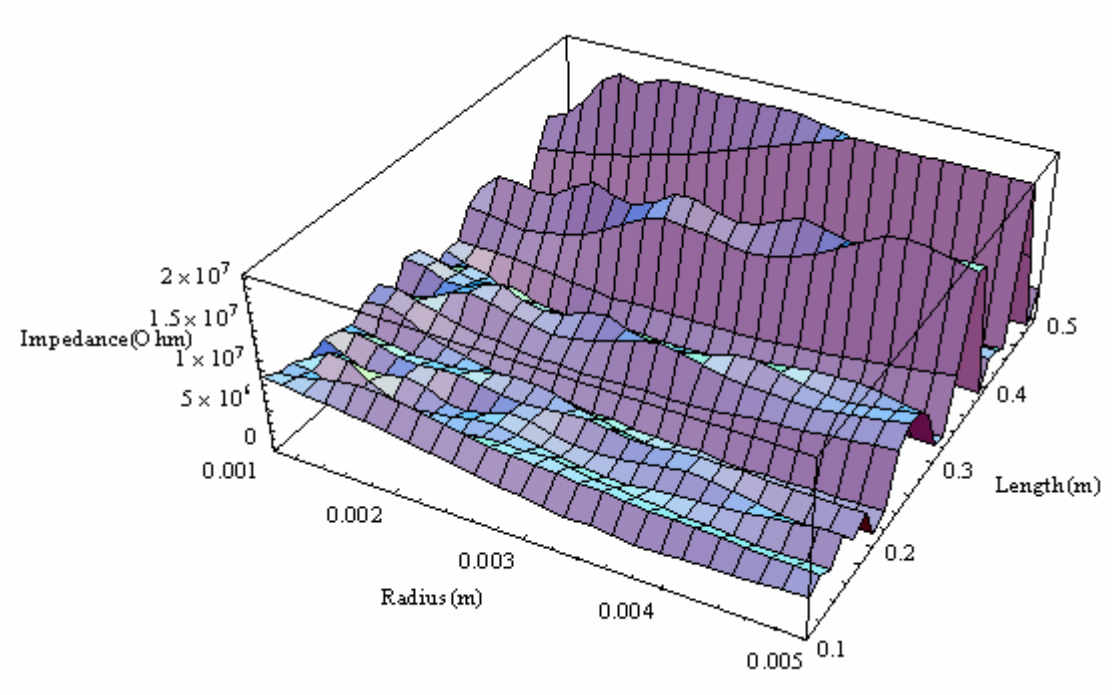

Figure 6-11: Variation of the objective function with both the hole size and position for cylindrical pipe 1 with 2mm radius sidehole

Examination of Figure 6-11 reveals a number of ridges, troughs and peaks. As expected, a trough along the minimiser value of l_1 = 0.31 m can be observed. However, it is not possible to see the expected global minimum at r_h = 2 mm and l_1 = 0.31 m as a ridge obscures this area of the plot.

To aid visualisation of the objective function, Figure 6-12 shows a contour map representation of the three dimensional plot of Figure 6-11. The trough along the minimiser value of l_1 = 0.31 m can again be observed. It is now clear that a minimum occurs somewhere between approximately r_h = 1.7 mm and r_h = 3.7 mm along the l_1 = 0.31 m line. The resolution of the contour map makes it impossible to both locate the exact position of the minimum and to confirm whether the minimum is a global minimum (or one of the several local minima that can be observed).

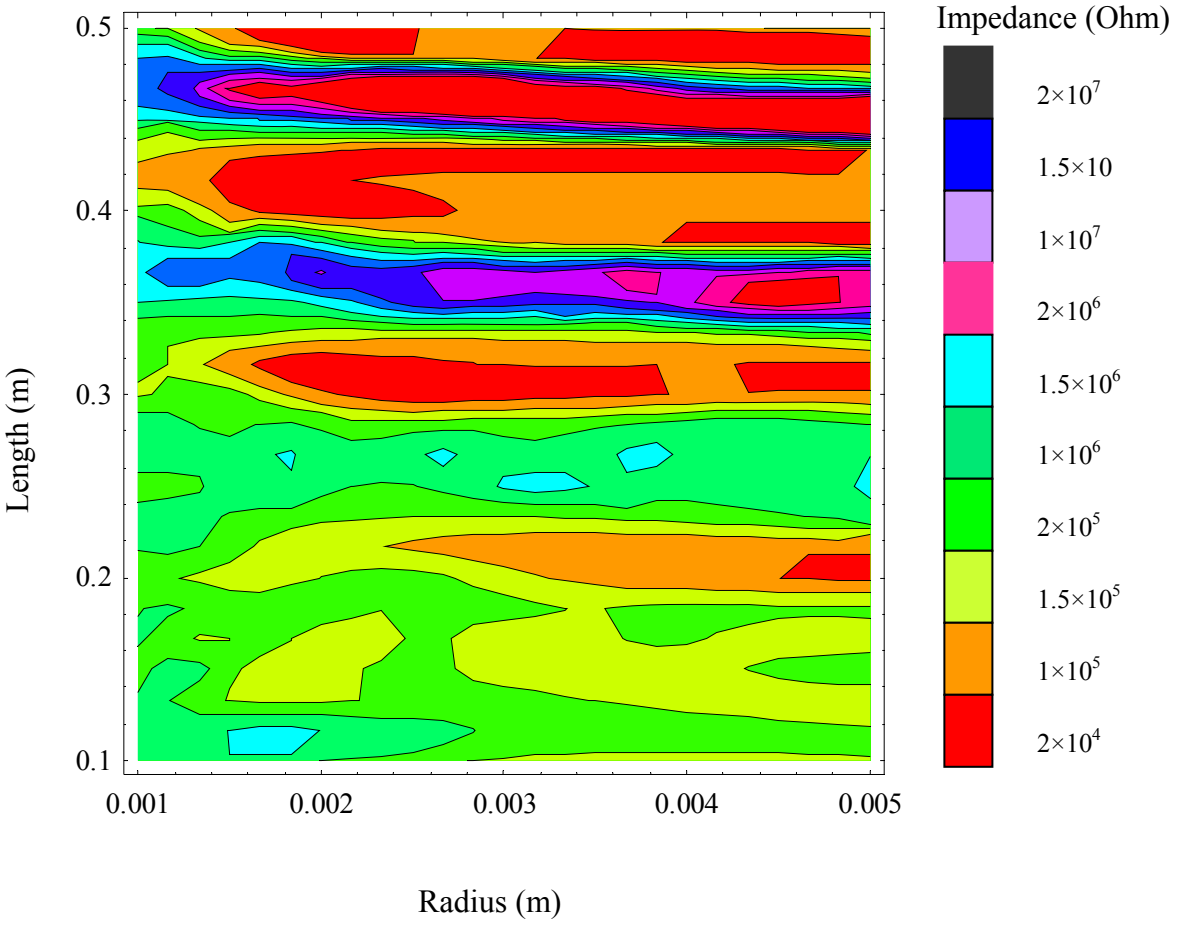

Figure 6-12: Contour map representation of the variation of the objective function for cylindrical pipe 1 with 2 mm radius sidehole with both the hole size and position

6.5 Two Variable Optimisation Methods

It proved difficult to locate the global function minimum using the objective function plots of Figures 6-11 and 6-12. However, this problem can be overcome by employing the two variable optimisation methods described in Section 5.5.1 and 5.5.2. These methods also enable both the hole size and hole location to be predicted in one operation, without having to calculate all the possible objective function values.

In this section, using the same cylindrical pipe test object as in Section 6.4, the success of both the Alternating Variable and the Steepest Descent method in predicting both hole size and hole position are investigated. As before, the pipe's experimentally measured input impedance was taken as the target value $z_{in(exp)}$ for the optimisation. The start value for the optimisation routine was found by calculating the theoretical impedance of the pipe with fixed parameters l_h = 1mm, r = 5.0 mm and l = 0.5 m and adjustable parameters r_h = 0.05 m and l_1 = 0.1 m. Figure 6-13 compares these start and target impedances.

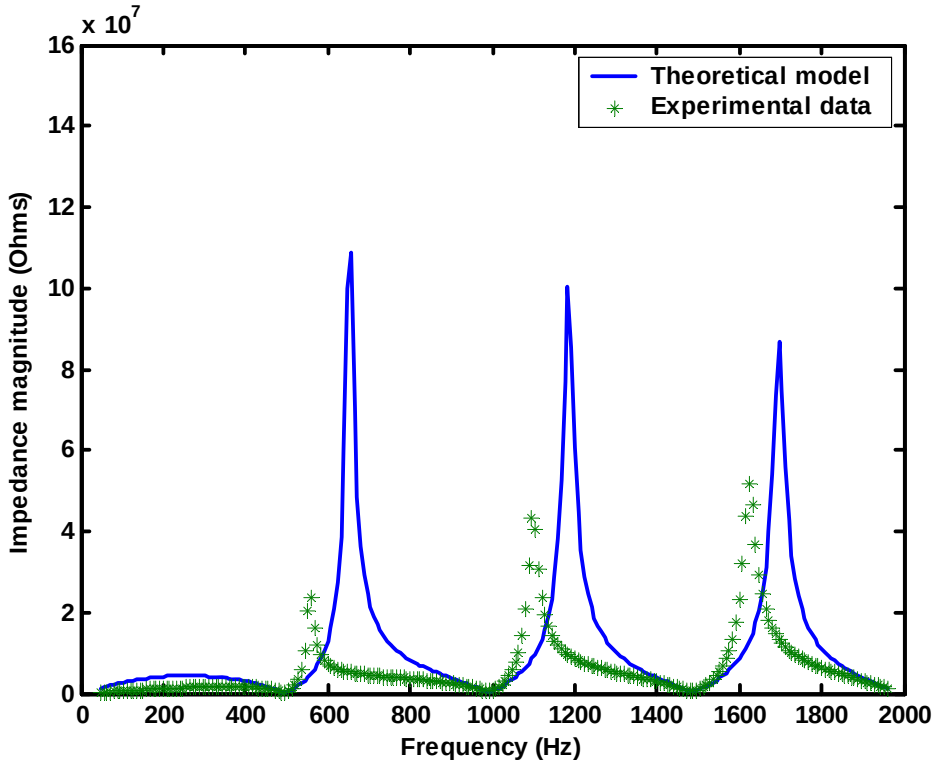

Figure 6-13: Comparison of the start and target impedances when searching for both hole size and hole position simultaneously (start values of rh = 0.05 m and l1 = 0.1 m)

It can be seen from Figure 6-13 that, as might be expected, there is a poor match between the start impedance of the model and the experimentally measured target impedance. The optimisation methods discussed in the following sections work by varying the values of r_h from 0.01 mm to 5 mm and l_1 from 0.1 m to 0.4 m until a match in the two impedances is achieved.

6.5.1 Alternating Variables Method

The initial hole radius was set as 0.05 mm and the initial hole position was set as 0.1 m. The stopping tolerance for the hole size minimiser was set as 0.05 mm and that for the hole position minimiser was set as 0.005 m.

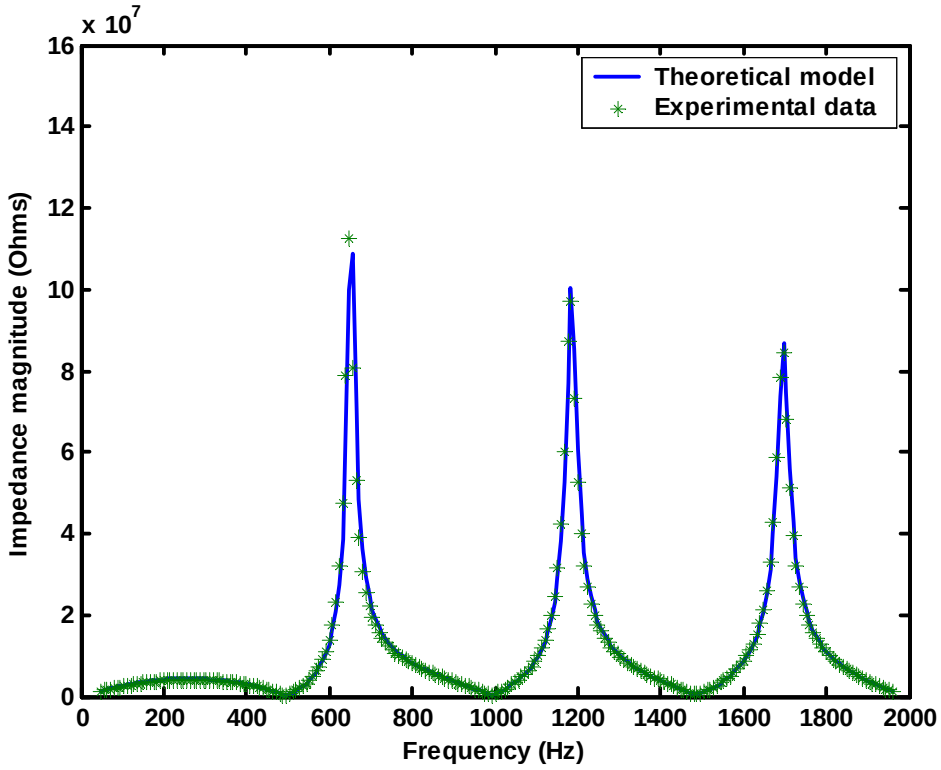

Figure 6-14: Comparison of the final and target impedances when searching for both hole size and hole position simultaneously using the Alternating Variables method

The objective function described in Equation (6.4) was optimised until the differences between the local minimisers and the current iterate were within the set stopping tolerances of 0.05 mm and 0.005 m for the hole radius and hole position respectively. Figure 6-14 compares the final value of the input impedance of the duct model after the optimisation was stopped with the experimentally measured target impedance. Examination of Figure 6-14 reveals that the theoretical input impedance and experimental impedance curves are now closely matching.

The values of the physically measured hole radius (parameter target value), the initial start values of the minimiser (parameter start value) and the final minimiser value (optimised parameter value) are shown in Table 6-7. The percentage difference between the

parameter target value *(TV)* and optimised parameter value *(TV)* was is also presented together with the number of iterations (*it*) and function evaluations (*eval*).

Parameter	Parameter target value *(TV)*	Parameter start value *(SV)*	Optimised parameter Value *(OV)*	*it*	*eval*	$\frac{\lvert TV - OV \rvert}{TV} \times 100$ (%)
r_h (mm)	2.000	0.050	2.050	36	47	2.5
L_1(m)	0.310	0.100	0.304	43	55	1.9

Table 6-7: Hole size and position predictions for cylindrical pipe 1 with 2 mm radius leak using the Alternating Variables method

From Table 6-7, it can be seen that the predicted hole radius agrees with the actual hole radius to within an accuracy of 2.5 %. The agreement between the predicted hole position and the actual hole position values is accurate to within 1.9 %**.** The success of the Alternating Variables method was expected as it is a non-derivative based method. Therefore, it was not affected by sudden changes in the gradient of the objective function (such as those observed in Figures 6-11 and 6-12).

6.5.2 Steepest Descent Method

The Steepest Descent method which uses conjugate directions for minimising a two variable function was discussed in Section 5.5.2. The method is based on finding the direction of the steepest descent of the function in order to find the function minimum value.

The initial hole radius was set as 0.05 mm and the initial hole position was set as 0.1 m. The parameter values after the optimisation are shown in Table 6-8. It can be seen from the table that neither the hole radius nor the hole position have been accurately predicted. The

reason for this is that the Steepest Descent method is a derivative based method and hence is unable to cope with sudden changes in the gradient of the objective function. This is because the gradient of the function is poorly defined at regions of sudden change and, hence, the function derivative cannot be calculated. This leads to a breakdown in the optimisation and the subsequent poor predictions.

Parameter	Parameter target value *(TV)*	Parameter start value *(SV)*	Optimised parameter Value *(OV)*	*it*	*eval*	$\frac{\lvert TV-OV\rvert}{TV}\times 100$ (%)
r_h (mm)	2.000	0.050	1.06×10^{-6}	44	176	100
l_l(m)	0.310	0.100	0.367			18

Table 6-8: Hole size and position predictions for cylindrical pipe 1 with 2 mm radius leak using the Steepest Descent method

6.6 Conclusion

From the results shown in this chapter, it can be concluded that it is possible to investigate a single leak in a cylindrical pipe using numerical optimisation. Correct predictions of the hole size and hole position are possible using methods which employ predetermined step size and search directions. These methods are the one variable Grid Search method and the Golden Section Search method. For the two variable methods, the Alternating Variables method was able to give correct predictions of both the hole size and hole location.

The derivative based methods such as the Steepest Descent and the Newton-Raphson method (which involve calculating the gradient of the objective function) generally gave predictions of hole size and position that were in poor agreement with the actual values. This can be attributed to the fact that the objective functions used in this chapter exhibited

sudden changes in slope in certain regions. For example, it was shown in the objective function plot of Figure 6-1 that a sharp peak was present at a hole radius of approximately 0.7 mm.

In Chapter 7, the Rosenbrock algorithm, a 0th order method (a method which doesn't involve calculating the derivatives of a function) described in Chapter 5, Section 5.7.7 is applied to the minimisation of functions of more than one variable. Judging from the performance of the non derivative based methods in this Chapter, it is expected that a 0th order method is likely to yield better predictions of the sizes and positions of multiple holes in the wall of a pipe than a higher order method would.

Chapter 7

Investigating Multiple Leaks in a Cylindrical Duct using Numerical Optimisation

In this chapter, the problem of detecting, locating and sizing multiple leaks in a cylindrical duct is addressed. A similar procedure to that used in Chapter 6 for a single leak is employed. First of all, the input impedance of the duct under investigation is determined. This input impedance is treated as the target value for the optimisation routine. Next, a numerical model of a duct of arbitrary length containing several leaks is derived. The theoretical input impedance of this duct model is calculated and used as the start value for the optimisation routine. The optimisation routine then proceeds to adjust the length of the modelled duct, together with the positions and sizes of the leaks, recalculating the theoretical impedance each time until it matches the target value and the objective function is minimised. At this stage, the length, position and size of leaks in the numerical duct model should match that of the duct.

In Chapter 6 it was demonstrated that the non-derivative based optimisation methods (such as the Interval Reduction, Grid Search and Golden Section Search methods) gave accurate predictions of both hole size and hole position when used to investigate a single leak in a duct. On the other hand, the derivative based optimisation methods, in which the gradient of the objective function must be calculated at each iteration step, were unable to predict the hole size and hole position correctly. This was attributed to the sharp peaks that were observed in the objective function plots, with the slope of the function being poorly defined in regions of sudden gradient change.

As a result of the success of the non-derivative based optimisation methods, it was decided to investigate the possibility of applying the multidimensional Rosenbrock algorithm, discussed in Section 5.7.5, to the problem of examining multiple leaks in a duct. The Rosenbrock algorithm is a 0th order numerical optimisation method and therefore no derivatives of the objective function are required to arrive at the solution. The Rosenbrock algorithm has been previously applied with great success to the bore reconstruction of musical wind instruments [55-58].

Over the coming sections, the application of the Rosenbrock algorithm to the problem of investigating multiple leaks in a duct is discussed. In Section 7.2, the problem of predicting the sizes of the holes in the walls of a cylindrical pipe containing two leaks, when the geometry of the pipe and the leak locations are known, is investigated. In Section 7.3, the optimisation approach is extended further to enable both the sizes and the positions of the holes in a pipe containing three leaks to be predicted. Finally, in Section 7.4, a procedure for identifying the number of leaks in a cylindrical pipe and predicting their sizes and positions is presented.

In all the test cases for the Rosenbrock algorithm demonstrated in Section 7.1, 7.2 and 7.3, the boundary parameters and starting points of the minimisers were set to represent extreme initial values for the optimisation. The results of the predictions of the radii and locations of the leaks shown in the following sections, therefore, also demonstrate the robustness of the Rosenbrock algorithm. The algorithm was tested with various boundary and initial values closer to the solution than the extreme values. As expected these values led to improved performance in the predictions from the optimisation. For the purposes of this thesis only, the prediction results for the extreme initial values have been shown.

7.1 Predicting the Sizes of Multiple Leaks in a Duct

To investigate the effectiveness of the Rosenbrock algorithm in predicting the sizes of several leaks in a cylindrical pipe when the leak locations and the pipe's geometry are both known, a new test object was introduced. This test object was a cylindrical pipe of total length l = 0.8 m, internal radius r = 5 mm and wall thickness l_h = 1 mm. It contained two 2 mm radius sideholes located at distances of 0.22 m and 0.44 m from the input end of the pipe.

When investigating a pipe containing two leaks whose locations are known, there are two function minimisers – the radii of the two holes, $r_{h(1)}$ and $r_{h(2)}$. The objective function (whose general form is given in Equation (6.1)) can be written as

$$f(r_{h(1)}, r_{h(2)}) = \sum_{i=4}^{40} \left| z_{in(\exp)}(48.83i) - z_{in(\mathrm{mod})}(r_{h(1)}, r_{h(2)}, 48.83i) \right| \tag{7.6}$$

As previously, $z_{in(exp)}$ represents the target impedance for the optimisation routine, $z_{in(mod)}$ is the theoretical input impedance of a model duct containing two sideholes (calculated in the manner described in Chapter 2 using fixed parameters r = 5 mm, l_h = 1 mm, l_1 = 0.22 m, l_2 = 0.22 m and l_3 = 0.36 m to match the dimensions of the test object), and $r_{h(1)}$ and $r_{h(2)}$ are the two function minimisers. Both $z_{in(exp)}$ and $z_{in(mod)}$ can represent either the impedance magnitude or the impedance phase.

In implementing the Rosenbrock algorithm, the boundary parameters for the minimisers were set to be 0.5 mm to 3 mm. The initial values of the minimisers must lie within these boundaries and were chosen to be $r_{h(1)}$ = 0.6 mm and $r_{h(2)}$ = 0.6 mm.

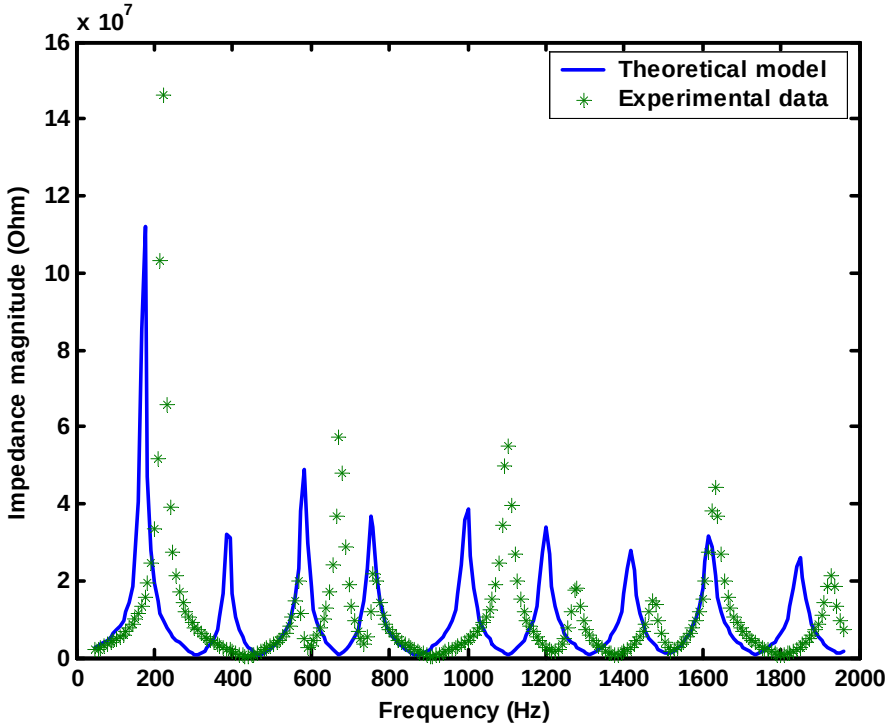

Figure 7-1: Comparison between the initial theoretical impedance of the two leak duct model and the experimentally measured (target) impedance of the cylindrical pipe containing two 2 mm radius leaks using magnitude information

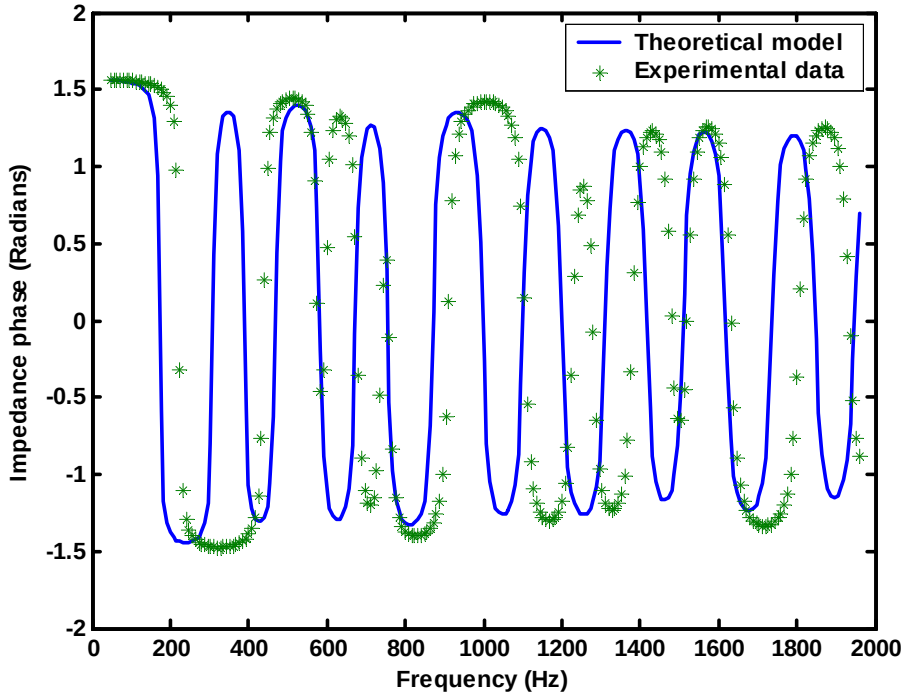

Figure 7-2: Comparison between the initial theoretical impedance of the two leak duct model and the experimentally measured (target) impedance of the cylindrical pipe containing two 2 mm radius leaks using phase information

Figures 7-1 and 7-2 compare the start impedance of the model with the target impedance for the optimisation in terms of magnitude and phase respectively. Clearly there is a poor match between the two impedances both in magnitude and phase terms.

By varying the values of $r_{h(1)}$ and $r_{h(2)}$, the Rosenbrock algorithm attempts to minimise the value of the objective function and hence improve the match between the two impedances. The initial step size was set as 0.05 mm. When carrying out the searches in each iteration cycle of the Rosenbrock algorithm, in the case of a success (a reduction in the calculated value of the objective function) the step size was multiplied by +3 while in the case of a failure (an increase in the calculated value of the objective function) the step size was multiplied by -0.5. Using these settings, the Rosenbrock algorithm was used to minimise the objective function of Equation (7.6).

Figures 7-3 and 7-4 compare the final impedance of the theoretical model (after 100 iterations of the Rosenbrock algorithm) with the target impedance in terms of both magnitude and phase. There is clearly now an excellent agreement between the two impedances both in magnitude and in phase terms.

The predictions of the radii of the two holes resulting from the optimisation are presented in Table 7-1. Examination of the table reveals that when the optimisation routine was applied to the measurements of impedance magnitude, predictions of $r_{h(1)}$ = 2.02 mm and $r_{h(2)}$ = 1.99 mm were achieved. These agree with the actual 2 mm radius values to within a 1% error. Meanwhile, when the measurements of impedance phase were used for the optimisation, predictions of $r_{h(1)}$ = 1.94 mm and $r_{h(2)}$ = 1.93 mm were made. These agree with the actual radii of the holes to within 4% accuracy.

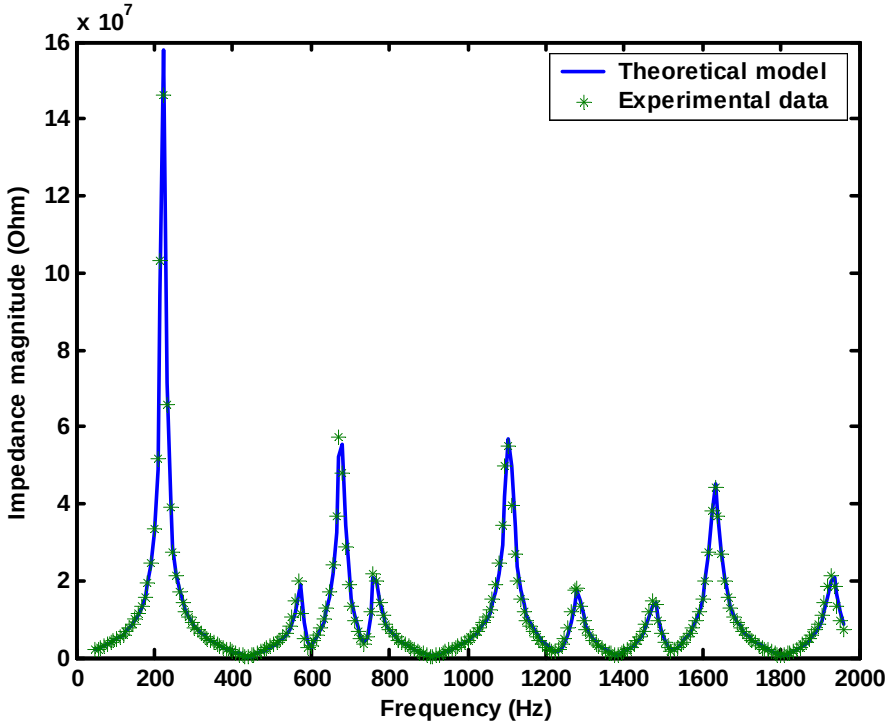

Figure 7-3: Comparison between the final theoretical impedance of the two leak duct model and the experimentally measured (target) impedance of the cylindrical pipe containing two 2 mm radius leaks using magnitude information

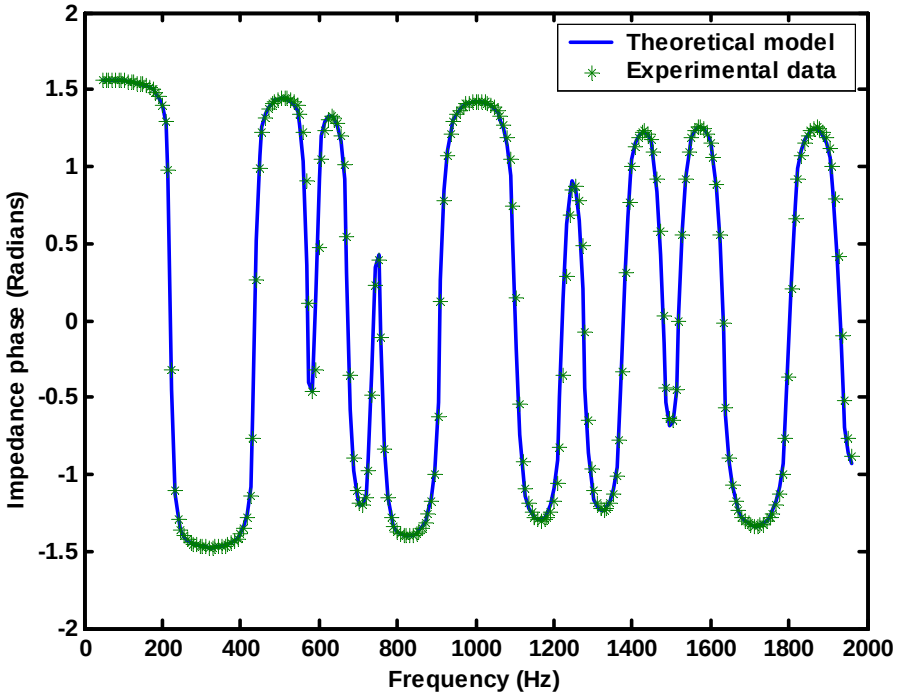

Figure 7-4: Comparison between the final theoretical impedance of the two leak duct model and the experimentally measured (target) impedance of the cylindrical pipe containing two 2 mm radius leaks using phase information

Although the impedance magnitude measurements provided slightly more accurate predictions of the hole radii, Table 7-1 shows that fewer steps were required to arrive at the predictions when using the phase information. Indeed, the average number of steps per iteration cycle when using the impedance phase measurements was 20.8 compared with 36.8 when using the impedance magnitude.

Parameter	Start parameter value (SV)	Target parameter value *(TV)*	Optimised parameter value *(OV)*	Average iteration steps *(AS)*	$\frac{\lvert TV - OV \rvert}{TV} \times 100$ (%)
Magnitude objective function					
$r_{h(1)}$	0.60 mm	2.00 mm	2.02 mm	36.8	1.0
$r_{h(2)}$	0.60 mm	2.00 mm	1.99 mm		0.5
Phase objective function					
$r_{h(1)}$	0.60 mm	2.00 mm	1.94 mm	20.8	3.0
$r_{h(2)}$	0.60 mm	2.00 mm	1.93 mm		3.5

Table 7-1: Hole size predictions with associated speeds and accuracies for the cylindrical pipe with two 2 mm radius leaks using Rosenbrock algorithm with two leak duct model

7.2 Predicting the Sizes and Positions of Multiple Leaks in a Duct

In most practical situations when investigating a leaking pipe, neither the sizes nor the positions of the holes are known. In this section, the Rosenbrock algorithm is used to predict both the sizes and the positions of several leaks in a duct. The only knowledge required by the algorithm is the pipe's internal radius, its wall thickness and how many leaks are present. In order to demonstrate the effectiveness of the Rosenbrock algorithm in making such predictions, another cylindrical pipe test object was used. This cylindrical

pipe had a total length l = 1.02 m, an internal radius r = 5 mm and a wall thickness l_h = 1 mm. It contained three 2 mm radius sideholes located at distances of 0.22 m, 0.44 m and 0.66 m from the input end of the pipe.

When investigating a pipe with three leaks whose sizes and positions are unknown, there are seven function minimisers – the radii of the three holes, $r_{h(1)}$, $r_{h(2)}$ and $r_{h(3)}$, and the four length parameters, l_1, l_2, l_3 and l_4 (see Figure 2-3), that define the positions of the three holes. The objective function for the optimisation is written:

$$f(l_1, r_{h(1)}, l_2, r_{h(2)}, l_3, r_{h(3)}, l_4) = \sum_{i=4}^{40} \left| \begin{array}{l} z_{in(\exp)}(48.83i) - \\ z_{in(\mathrm{mod})}(l_1, r_{h(1)}, l_2, r_{h(2)}, l_3, r_{h(3)}, l_4, 48.83i) \end{array} \right| \qquad (7.7)$$

where $z_{in(exp)}$ again represents the target impedance for the optimisation routine, $z_{in(mod)}$ is the theoretical input impedance of a model duct of arbitrary length containing three sideholes (calculated in the manner described in Chapter 2 using fixed parameters r = 5 mm and l_h = 1 mm to match the internal radius and wall thickness of the test object), and $r_{h(1)}$, $r_{h(2)}$, $r_{h(3)}$, l_1, l_2, l_3 and l_4 are the seven function minimisers. Both $z_{in(exp)}$ and $z_{in(mod)}$ can represent either the impedance magnitude or the impedance phase.

Before applying the Rosenbrock algorithm to the minimisation of the objective function of Equation 7.7, boundary parameters of 0.5 mm to 3 mm were set for the radius minimisers and boundary parameters of 0.05 m to 0.5 m were set for the length minimisers. The three hole radii were set to initial values of $r_{h(1)}$ = 0.6 mm, $r_{h(2)}$ =0.6 mm and $r_{h(3)}$ = 0.6 mm

whilst the four length parameters were set to initial values of l_1 = 0.1 m, l_2 = 0.1 m, l_3 = 0.1 m and l_4 = 0.1 m. Using these initial values, the start value of the input impedance of the model was calculated. Figures 7-6 and 7-7 compare this start impedance with the

target impedance for the optimisation in terms of both magnitude and phase. As might be expected, for both the magnitude and the phase, there is a poor match between the two impedances.

The Rosenbrock algorithm then adjusted the values of the seven minimisers until the objective function of Equation (7.7) was minimised. As described in the previous section, when carrying out the searches, a multiplier of +3 was applied for a success and a multiplier of -0.5 was applied for a failure.

Figures 7-7 and 7-8 compare the final impedance of the theoretical model (after 100 iterations of the Rosenbrock algorithm) with the target impedance in terms of both magnitude and phase. From Figure 7-8, it is clear that there is an excellent match between the impedance phase of the model after optimisation and the target impedance phase. However, the impedance magnitudes of Figure 7-7 exhibit a less good agreement. These results are borne out in the predictions of the radii and locations of the three holes that are presented in Table 7-2.

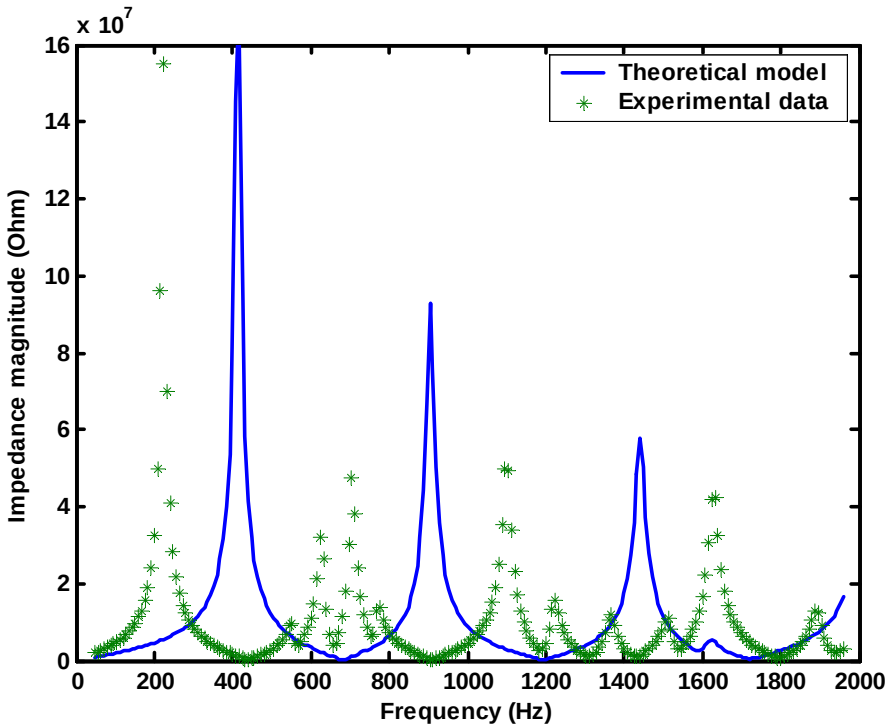

Figure 7-5: Comparison between the initial theoretical impedance of the three leak duct model and the experimentally measured (target) impedance of the cylindrical pipe containing three 2 mm radius leaks using magnitude information

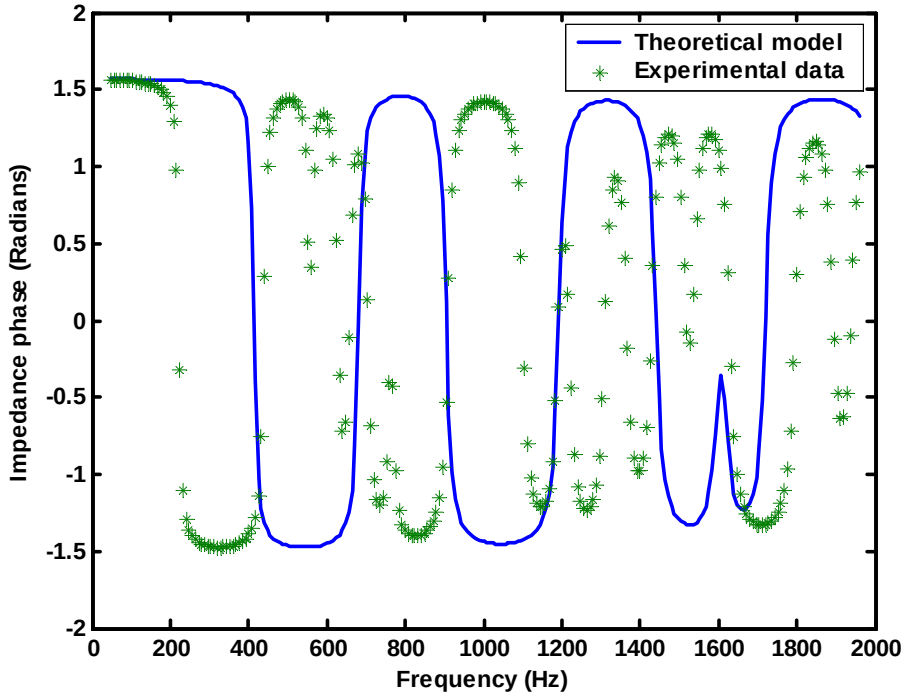

Figure 7-6: Comparison between the initial theoretical impedance of the three leak duct model and the experimentally measured (target) impedance of the cylindrical pipe containing three 2 mm radius leaks using phase information

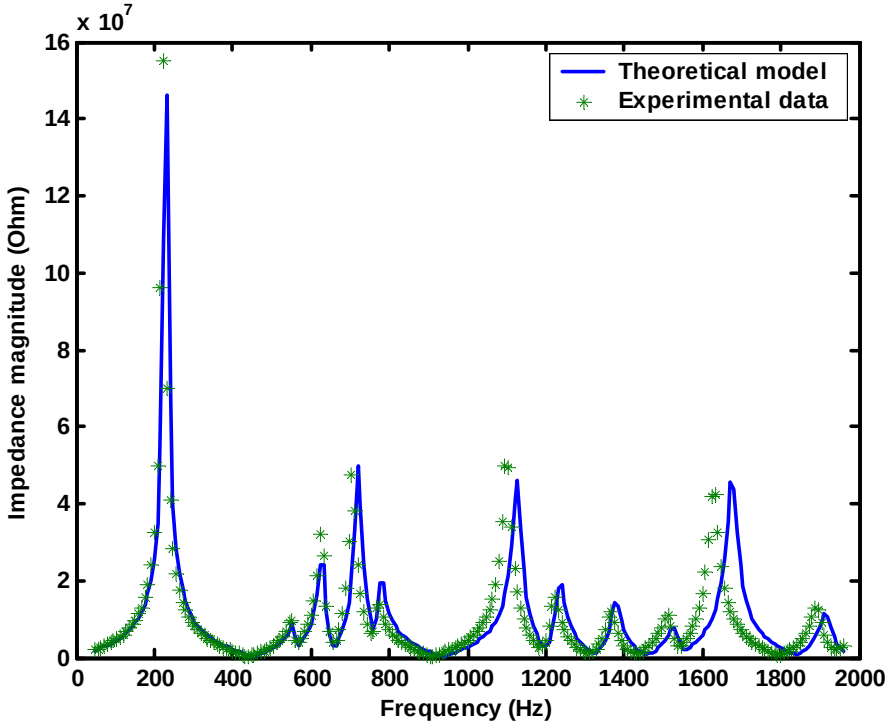

Figure 7-7: Comparison between the final theoretical impedance of the three leak duct model and the experimentally measured (target) impedance of the cylindrical pipe containing three 2 mm radius leaks using magnitude information

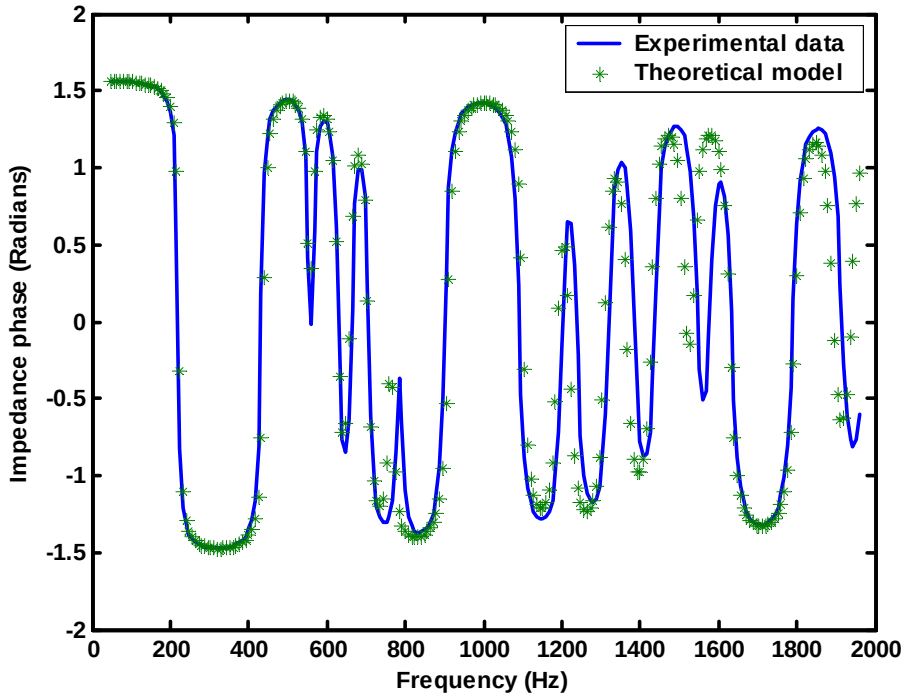

Figure 7-8: Comparison between the final theoretical impedance of the three leak duct model and the experimentally measured (target) impedance of the cylindrical pipe containing three 2 mm radius leaks using phase information

Parameter	Start parameter value (SV)	Target parameter value *(TV)*	Optimised parameter value *(OV)*	Average iteration steps *(AS)*	$\frac{\lvert TV-OV\rvert}{TV}\times 100$ (%)
Magnitude objective function					
$r_{h\,(1)}$	0.600 mm	2.000 mm	1.800 mm	62	10.0
$r_{h\,(2)}$	0.600 mm	2.000 mm	2.100 mm		5.0
$r_{h(3)}$	0.600 mm	2.000 mm	1.900 mm		5.0
l_1	0.100 m	0.220 m	0.199 m		9.5
l_2	0.100 m	0.220 m	0.202 m		8.2
l_3	0.100 m	0.220 m	0.208 m		5.2
l_4	0.100 m	0.360 m	0.336 m		6.7
Phase objective function					
$r_{h\,(1)}$	0.600 mm	2.000 mm	1.900 mm	47.2	5.0
$r_{h\,(2)}$	0.600 mm	2.000 mm	1.900 mm		5.0
$r_{h(3)}$	0.600 mm	2.000 mm	1.900 mm		5.0
l_1	0.100 m	0.220 m	0.212 m		3.7
l_2	0.100 m	0.220 m	0.209 m		4.7
l_3	0.100 m	0.220 m	0.214 m		2.7
l_4	0.100 m	0.360 m	0.364 m		1.2

Table 7-2: Hole size predictions with associated speeds and accuracies for the cylindrical pipe with three 2 mm radius leaks using Rosenbrock algorithm with three leak duct model

Examination of Table 7-2 reveals that when the optimisation routine was applied to the measurements of impedance magnitude, hole radius predictions of $r_{h(1)}$ = 1.80 mm, $r_{h(2)}$ = 2.10 mm and $r_{h(3)}$ = 1.90 mm were achieved. These agree with the actual 2 mm radius values with accuracies of 10%, 5% and 5% respectively. The impedance phase

measurements gave results of similar accuracy with hole radius predictions of $r_{h(1)}$ = 1.90 mm, $r_{h(2)}$ = 1.90 mm and $r_{h(3)}$ = 1.90 mm, each agreeing with the actual 2 mm radius values to within 5%.

The hole position predictions resulting from the application of the optimisation routine to the impedance magnitude measurements were l_1 = 0.199 m, l_2 = 0.202 m, l_3 = 0.208 m, and l_4 = 0.336 m. These agree with the actual values to within errors of 9.5%, 8.2%, 5.2% and 6.7% respectively. Better accuracy was achieved from the impedance phase measurements with hole position predictions of l_1 = 0.212 m, l_2 = 0.2096 m, l_3 = 0.214 m, and l_4 = 0.364 m, agreeing with the actual values to within 3.7%, 4.7%, 2.7% and 1.2% respectively.

Close examination of the plots of Figures 7-8 and 7-9 shows that the phases of the final impedance of the model and the target impedance were in better agreement than their magnitudes. The prediction results from Table 7-2 also show better results for the phase values. When the experimental results from this section (which incorporate both radius and length predictions) are considered alongside those of Section 7.1 (showing the impedance magnitude values gave better predictions than the impedance phase values for the hole radius alone), it appears that the phase values are more affected by variations in length whilst the magnitude values are more influenced by variations in radius.

The superior predictions provided by the impedance phase measurements were not at the expense of computational speed. Indeed, the average number of steps per iteration cycle was again found to be lower for the phase objective function than for the magnitude objective function.

It is worth noting that, as might be expected, the average number of steps per iteration cycle for the three leak objective functions shown in Table 7-2 are greater than the average number of steps for the corresponding two leak objective functions shown in Table 7-1.

7.3 Identifying the Number of Leaks in a Duct and Predicting their Sizes and Positions

In Sections 7.2 and 7.3, the number of leaks present in the duct under investigation had to be known before predictions of the radii and positions of the holes could be made. In this section, it is shown that, providing the number of sideholes included in the theoretical duct model is greater than the actual number of leaks in the duct under test, the Rosenbrock algorithm can be used both to identify the number of leaks in a duct and to predict their sizes and positions.

To demonstrate this, the cylindrical pipe containing two leaks (first introduced in Section 7.2) was used as the test object. This pipe had the following parameters: r = 5 mm, l_h = 1 mm, l_1 = 0.22 m, l_2 = 0.22 m, l_3 = 0.36 m, $r_{h(1)}$ = 2 mm and $r_{h(2)}$ = 2 mm. The experimentally determined input impedance of the pipe $z_{in(exp)}$ again provided the target value for the optimisation routine.

Although the duct under investigation contained two leaks, a theoretical duct model was constructed which contained three sideholes. This model was identical to that used in Section 7.3 with two fixed parameters r = 5 mm and l_h = 1 mm (to match the internal radius and wall thickness of the test object) and seven adjustable parameters $r_{h(1)}$, $r_{h(2)}$, $r_{h(3)}$, l_1, l_2, l_3 and l_4. As a result, the objective function described by Equation (7.7) was used in the optimisation.

Just as in Section 7.3, boundary parameters of 0.5 mm to 3 mm were set for the radius minimisers and boundary parameters of 0.05 m to 0.5 m were set for the length minimisers. The three hole radii were all set to an initial value of 0.6 mm whilst the four length parameters were all set to an initial value of 0.1 m. Using these initial values, the start value of the input impedance of the model was calculated. Figures 7-10 and 7-11 show the poor match between the start impedance and the target impedance terms of both magnitude and phase.

Applying the Rosenbrock algorithm as before, with a multiplier of +3 for a success and a multiplier of -0.5 for a failure during the searches, the seven minimisers were adjusted until the objective function was minimised. Figures 7-12 and 7-13 compare the final impedance of the theoretical model (after 100 iterations of the Rosenbrock algorithm) with the target impedance in terms of both magnitude and phase.

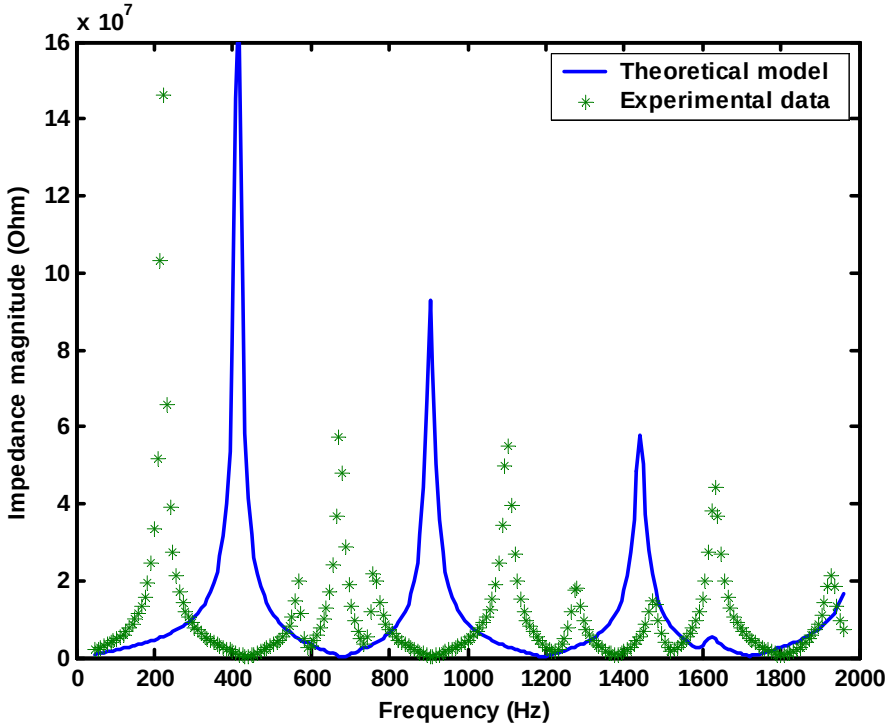

Figure 7-9: Comparison between the initial theoretical impedance of the three leak duct model and the experimentally measured (target) impedance of the cylindrical pipe containing two 2 mm radius leaks using magnitude information

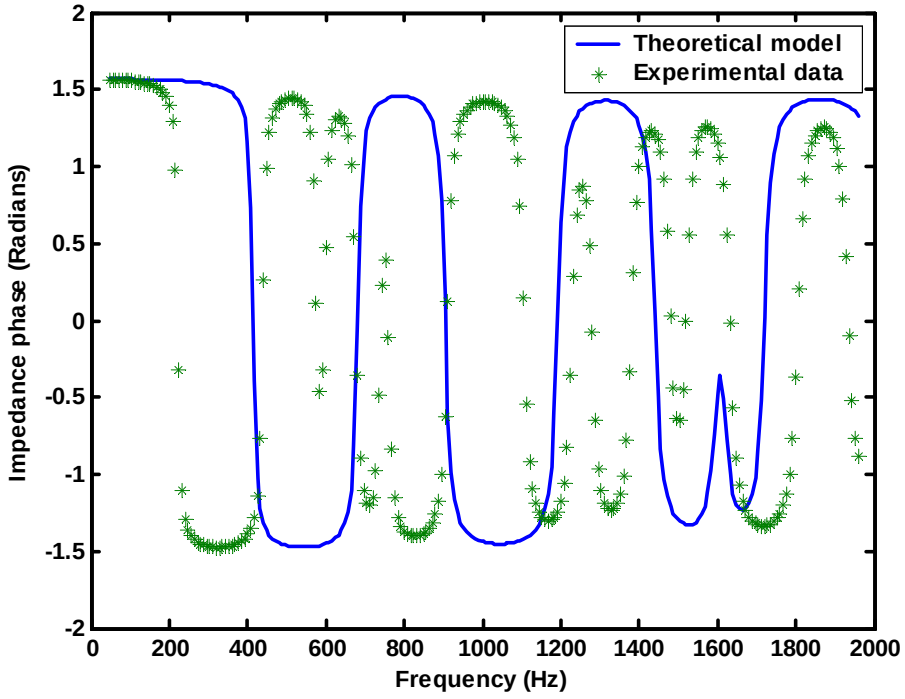

Figure 7-10: Comparison between the initial theoretical impedance of the three leak duct model and the experimentally measured (target) impedance of the cylindrical pipe containing two 2 mm radius leaks using phase information

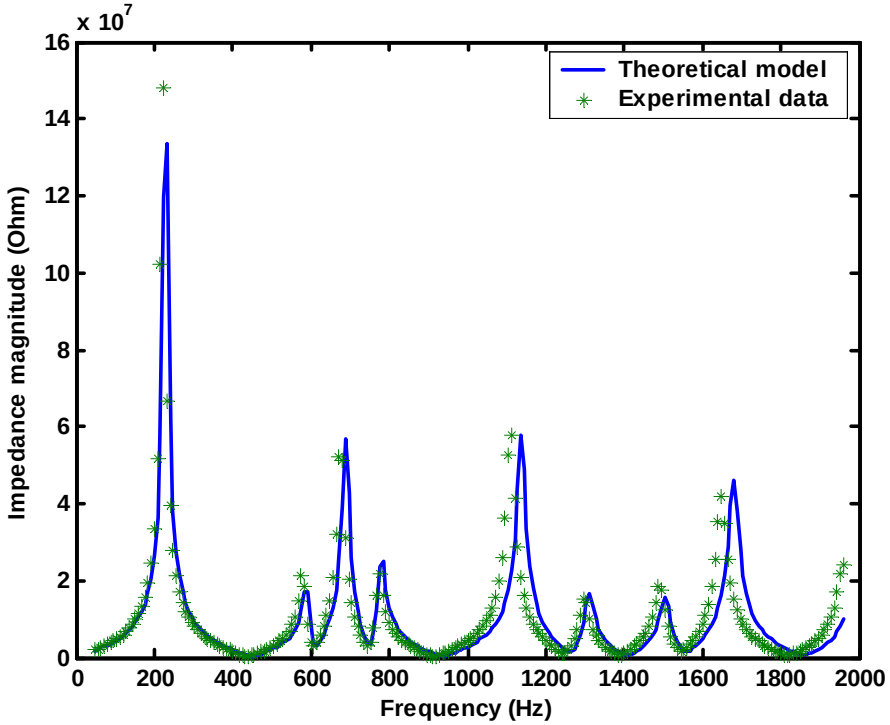

Figure 7-11: Comparison between the final theoretical impedance of the three leak duct model and the experimentally measured (target) impedance of the cylindrical pipe containing two 2 mm radius leaks using magnitude information

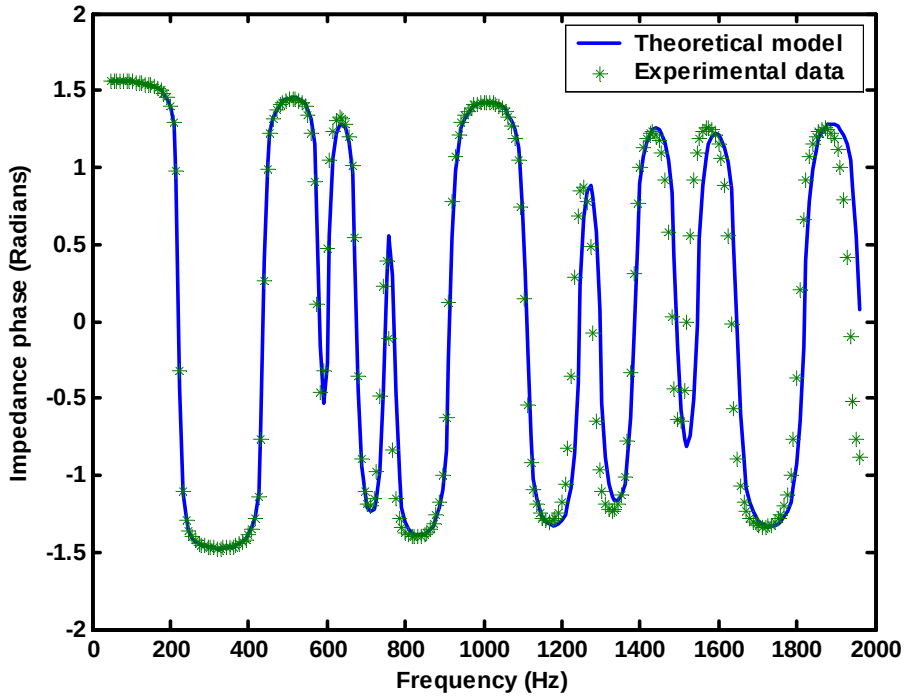

Figure 7-12: Comparison between the final theoretical impedance of the three leak duct model and the experimentally measured (target) impedance of the cylindrical pipe containing two 2 mm radius leaks using phase information

Again, examination of the two graphs reveals an excellent match between the final impedance of the theoretical duct model and the target impedance both in terms of magnitude and phase. The resultant predictions of the sizes and positions of the leaks are presented in Table 7-3.

Parameter	Start parameter value (SV)	Target parameter value *(TV)*	Optimised parameter value *(OV)*	Average iteration steps *(AS)*	$\frac{\lvert TV-OV\rvert}{TV}\times 100$ (%)
Magnitude objective function					
$r_{h\,(1)}$	0.600 mm	2.000 mm	1.900 mm	69	5.0
$r_{h\,(2)}$	0.600 mm	2.000 mm	1.800 mm		10.0
$r_{h(3)}$	0.600 mm	0.000 mm	0.100 mm		N/A
l_1	0.100 m	0.220 m	0.215 m		2.3
l_2	0.100 m	0.220 m	0.212 m		3.7
l_3	0.100 m	0.360 m	0.348 m		3.4
l_4	0.100 m	0.000 m	0.000 m		N/A
Phase objective function					
$r_{h\,(1)}$	0.600 mm	2.000 mm	1.900 mm	51	5.0
$r_{h\,(2)}$	0.600 mm	2.000 mm	2.100 mm		5.0
$r_{h(3)}$	0.600 mm	0.000 mm	0.000 mm		N/A
l_1	0.100 m	0.220 m	0.220 m		0.1
l_2	0.100 m	0.220 m	0.223 m		1.5
l_3	0.100 m	0.360 m	0.366 m		1.8
l_4	0.100 m	0.000 m	0.002 m		N/A

Table 7-3: Hole size predictions with associated speeds and accuracies for the cylindrical pipe with two 2 mm radius leaks using Rosenbrock algorithm with three leak duct model

From Table 7-3 it can be seen that after the optimisation had been carried out using measurements of input impedance magnitude, the radii of the three holes in the model duct were $r_{h(1)}$ = 1.9 mm, $r_{h(2)}$ = 1.8 mm and $r_{h(3)}$ = 0.1 mm. Of course, the cylindrical pipe under investigation only contained two leaks. This is reflected in the very small final radius for the third hole in the model duct. The radii of the first two holes in the model duct agree with the actual radii of the holes in the test object to within 10% (a similar accuracy to that

achieved in Section 7.2). The positions of the holes in the model duct after optimisation using the measurements of impedance magnitude were l_1 = 0.215 m, l_2 = 0.212 m, l_3 = 0.348 m and l_4 = 0.0003 m. The tiny final value of l_4 is again a reflection of the fact that there was not actually a third hole in the cylindrical pipe under investigation. In the model duct, the third hole has been predicted as being very small and has been placed very close to the end of the pipe. The other three length parameters are shown to agree with the actual values to within a 3.7% accuracy.

Using the phase measurements for the optimisation using the Rosenbrock algorithm provided similar results. After the optimisation, the radii of the three holes in the duct model were $r_{h(1)}$ = 1.9 mm, $r_{h(2)}$ = 2.1 mm and $r_{h(3)}$ = 0.0 mm. In this case, the third hole in the model duct actually has a zero radius (i.e. is non-existent). The final positions of the holes in the model duct were given by l_1 = 0.219 m, l_2 = 0.223 m, l_3 = 0.367 m and l_4 = 0.0002 m. Again, the tiny value of l_4 reflects the fact that this hole didn't exist in the cylindrical pipe under investigation. When the optimisation was carried out using impedance phase measurements, slightly more accurate predictions of the hole positions were achieved with the first three length parameters agreeing with the actual values to within 1.8%.

These results demonstrate that, providing that the theoretical duct model used in the objective function contains more sideholes than the pipe under investigation, the number of leaks in the pipe can be identified and their sizes and positions accurately predicted using an optimisation approach.

Finally the Resonbrock algorithm was tested with a theoretical model in the objective function having fewer sideholes than the leaks in the pipe. In all such test cases there was a

total collapse in the prediction results from the optimisation and as such results have not been shown in this thesis.

Chapter 8

Conclusion

8.1 Achievement of Aims

A method has been successfully developed in this thesis to detect, locate and predict the size of multiple leaks in air-filled pipes. To investigate the leaks, the method was applied to the acoustic reflections returning from a cylindrical pipe having one or more leaks in its side wall. The reflections were generated and acquired for processing using an acoustic pulse reflectometer.

The method presented in this thesis was first applied to the case of a single hole in the side wall of a cylindrical pipe as discussed in Chapter 4. During this investigation it was discovered that in order to fully investigate the range of hole sizes from 0.2 mm diameter up to 4 mm diameter, two separate theories needed to be applied to the acquired acoustic reflections returning from the cylindrical pipe under investigation. The original method developed by Sharp, and based on theory developed by Keefe for "large radius" holes, was applied to the investigation of holes of 1 mm, 2 mm, 3 mm and 4 mm diameters. The success of the method in predicting hole sizes within this range was excellent. All the predictions agreed with the physically measured values to within an accuracy of 10%. However, the method broke down for predictions involving holes of 0.2 mm and 0.3 mm diameters.

The method was adapted using theoretical approximations for “small radius” holes developed by Backus. This adapted method was applied to a pipe containing holes of diameter 0.2 mm and 0.3 mm. With the adjustments to the theory, the method now produced predictions of the hole sizes that agreed with the physically measured values to within a 10% accuracy.

Having successfully investigated the case of a single leak present in the side wall of a cylindrical pipe, in Chapter 5 several numerical optimisation methods which can be applied to multiple variable functions were discussed. The different possible methods were applied in Chapter 6 to the simple case of a single leak in the side wall of a cylindrical pipe. It was concluded that optimisation methods which are non-derivative based offered the best option of minimising the objective functions presented in Chapter 6.

In Chapter 7, the non-derivative based Rosenbrock algorithm was described and applied to the case of a pipe containing several leaks. In this way, it was possible to predict both the size and position of up to three leaks. A method for predicting the number of leaks in a cylindrical pipe was also implemented.

Three different cases were investigated during the application of the Rosenbrock algorithm. For the case of two leaks of known location in the side wall of a cylindrical pipe, the hole radius predictions agreed with the actual values to within 1% error when using a magnitude-based objective function and within 4% error when using a phase-based objective function. When there were three holes of unknown size and position, the results when using the magnitude-based objective function for the radius and position predictions were within 10% accuracy. The results when using the phase-based objective function were accurate to within 5 % for the radius and position predictions.

The results from the leak investigations using both analytical methods and numerical optimisation methods show that the aims of the thesis stated in the introduction have been fully met by the work covered in this research.

8.2 Future Work

8.2.1 Larger Diameter Pipes

The investigations in this thesis were limited to cylindrical pipes whose diameters were less than the wavelength of the propagating sound wave. Previous work done in this specific area of research has also been limited to such pipe diameters, largely due to the complexity of having to deal with higher order modes of sound wave propagation if larger diameter pipes are employed. However, with the successful application of numerical optimisation of objective functions that incorporate both theoretical impedance models and experimentally measured impedances, extending the investigations to larger pipes has become more feasible. By including the effects of higher order modes in the theoretical impedance models, the optimisation algorithms can be applied to the problem in a similar procedure to that described in Chapters 6 and 7.

8.2.2 Complex Bore Geometries and Modelling Musical Wind Instruments

In this thesis, the studies were confined to investigating leaks in straight cylindrical pipes. By adapting the theoretical model of the duct that is used in the objective function, it should be possible to investigate leaks in ducts with non-cylindrical, non-uniform geometry. The first step would be to extend the multiple leak investigations to conical and

horn-shaped ducts. Further extension to more complex bore geometries would then be possible by treating the shape as a combination of multiple slices. These shapes can then be connected by existing techniques such as transmission line modelling (the technique of transmission matrices upon which the technique of transmission line modelling is based was described in Chapter 3 of this thesis). This technique has been successfully applied in musical acoustics to calculate the input impedance of musical wind instruments. The different parts of the wind instrument, which are the mouthpiece, lead pipe and the bell, have all been successfully modelled and their impedances calculated. The work presented in this thesis can be used to extend work in this important area of research to cope with the modelling of tone holes.

8.2.3 Leaks of Various Shapes

The work in this thesis was based on modelling the leaks in cylindrical pipes as holes of circular geometry. However, the derivation of impedance equations for narrow tubes with an arbitrary cross-section has been discussed by Stinson [59]. He presented equations for calculating the input impedance of holes with rectangular, slit and triangular shapes. Though, most of these equations were applied in the characterisation of sound absorbers, the basic underlining derivations are the same and are applicable to the research in leak detection.

8.2.4 Longer Pipes

As the leak investigations presented in this work are based on the experimental measurement of input impedance using the object's input impulse response, the methods

described should be able to work on any pipe length as long as the impulse response from the object has been successfully separated from the noise signal.

Currently the technique of acoustic pulse reflectometry has been used to successfully make measurements of tubes with lengths similar to the cylindrical pipes investigated in this thesis (i.e. up to approximately 2 m). However, versions of the acoustic pulse reflectometer that can be used for measuring the input impulse response of longer objects have been proposed. One of the methods suggested is that of using a longer source tube. This is based on the idea that the increased distance between the speaker and the object under investigation, would allow for a longer travelling time of the reflections from the object before encountering interference from the reflections travelling back from the speaker. This method has a limitation in that it is not physically possible to keep increasing the length of the source tube of the reflectometer. Alternative methods have been proposed by Marshall, Schroeder, Amir and Sharp. The method proposed by Schroeder is considered to be more established. This method involves the introduction of a second microphone in the source tube such that the input impulse response of the object is found by deconvolving the reflected signal with the incident signal.

8.2.5 Water Pipes

It should be possible to extend the leak investigations to water-filled pipes. Several acoustical methods currently being used to detect leaks in water-filled pipes show that it is possible to extract the leak signal from the noise signal transmitted from the position of the leak using existing signal processing techniques. For example the cross-correlation technique has been successful in separating the leak signal and locating the leak using a simple algebraic relationship between the time lag, sensor-to-sensor spacing, and sound propagation velocity in the pipe. The separated noise signal can also be used to identify the

type of leak from its spectral charateristics. For example, the leak or orifice signal is known to occur within the 500 – 800 Hz range; the leak water impacting on the soil will occur normally in the range of 20 -300Hz [60].

The method described in this thesis offers a more-controlled signal than existing methods because the incident wave and reflections are self-generated from the input pulse triggered from a noise source such as a speaker. Since the characteristic of the background noise in the water pipe is a known variable, appropriate filtering coefficients can be described from which it is possible to extract the reflections resulting from the transmitted pulse. It is expected that the background noise will be varying as the factors contributing to the noise are not constant. Techniques to deal with the changing background noise can be used such as adaptive filtering where the filter coefficients are automatically adjusted in real time.
Having separated the reflections from the noise source, apart from predicting the size and position of the leak, it should be possible to study the frequency content of the extracted leak signal to identify the leak source or type. One important aspect of this work is that a successful application of the method to water pipes would provide a means of detecting smaller leaks in water pipe than is currently possible. This is crucial in the water industry as it would offer the possibility of identifying cracks in a pipeline before a water burst occurs.

References

1. Sharp, D.B., *Acoustic pulse reflectrometry for the measurement of musical wind instruments*. 1996, University of Edinburgh.
2. Jackson, A.C., et al., *Airway geometry by analysis of acoustic pulse response measurements* J.Appl.Physiol., 1977. **43**(3): p. 523-536.
3. Sondhi, M.M. and Gopinath, B., *Determination of vocal-tract shape from impulse response at the lips.* J.Acoust.Soc.Am, 1971. **49**(6): p. 1867-1873.
4. Sondhi, M.M. and Resnick, J.R., *The inverse problem for the vocal tract: numerical methods, acoustical experiments, and speech synthesis.* J.Acoust.Soc.Am, 1983. **73**(3): p. 985-1002.
5. Benade, A.H. and Smith, J.H., *Brass wind instrument impulse response measurements.* J.Acoust.Soc.Am, 1981. **70**: p. S22.
6. Smith, R.A., *It's all in the bore! International Trumpet.* Guild Journal 1988. **12**(4).
7. Watson, A.P. and Bowsher, J.M. *Recent progress in time domain work on brass instruments*. in *Proceedings of the IOA*. 1987.
8. Watson, A.P. and Bowsher, J.M., *Impulse measurements on brass musical instruments.* Acustica, 1988. **66**(3): p. 170-174.
9. Watson, A.P., *Impulse measurements on tubular acoustic systems*. 1989, University of Surrey.
10. Sharp, D.B., Campbell, D.M., and Myers, A., *Pulse reflectometry as a method of leak detection in historical brass instruments*, in *Forumn Acusticum*. 1996: Antwerp, Belgium.
11. Parker, J., *Acoustic Detection and Location of Leaks in Underground Natural Gas Distribution Lines* John Hopkins APL Technical Digest, 1981. **2**(2): p. 90-101.
12. Smith, L.O., *The Soundograph System for Gas Leak Detection* Gas Age-Record, 1933. **381-383**.
13. Gilmore, R.E., *Lost Gas Speaking.* Gas Age-Record, 1935: p. 1-4.
14. Richardson, R.B., *Listening for leaks, Gas Age-Record.* Gas Age-Record, 1935: p. 47-48.
15. Larson, D.B. *Practical use of sound amplifiers in gas leak detection*. in *Proc. Pacific Coast Gas Association* 1939.
16. McElwee, L.A. and Scott, T.W., *The Sonic Leak detector.* Am. Gas J. , 1957. **184**: p. 14-17.

17. Reid, J.M., Hogan, D.P., and Michel, P.L. *A New Approach to Pinpointing Gas Leaks*. in *presented at the A.G.A. Operating Section Distribution Conference*. 1961.
18. Kovecevich, J.J., et al., *Recent Advances in Application of Acoustic Leak Detection to Process Recovery Boilers*. 1995, Babcock and Wilcox p. 1-7.
19. Jolly, W.D., et al., *Methods for Rapid Leak Detection in Offshore Pipelines* 1992, Department of the Interior Minerals Management Service: U.S. p. 1-84.
20. Fuchs, H.V.a.R., R. Ten *Years experience with leak detection by Acoustic Signal Analysis.* Applied Acoustics 33, 1990. **33**: p. 1-19.
21. Reed, E.C., *Report on water losses* Aqua, 1980. **8**: p. 178-91.
22. Brainard, F.S., *Leakage problems and benefits of leak detection programs* J. AWWA, 1979: p. 64-5.
23. Shaw, C.E., *Methods of leak detection: An overview* J. AWWA, 1979: p. 73-5.
24. Laverty, G.L., *Leak detection: Modern methods, cost and benefits.* J. AWWA, 1979: p. 61-3.
25. Akizuki, K. *Detecton of water leakage point using cross correlation methods*. in *IMEKO symp. Flow Measurements and Control in Industry*. 1979. Tokyo.
26. Kinsler, L.E. and et al., *Fundamentals of acoustics*. 3 ed. 1982, New York John Wiley and sons.
27. Keefe, D.H., *Acoustical wave propagation in cylindrical ducts: Transmission line parameters approximations for isothermal and nonisothermal boundary conditions.* J.Acoust.Soc.Am, 1984. **75**(1): p. 58-62.
28. Backus, J., *Input impedance curves for the reed woodwind instruments* J.Acoust.Soc.Am, 1974. **56**(4): p. 1266-1279.
29. Backus, J., *Input impedance curves for the brass instruments.* J.Acoust.Soc.Am, 1976. **60**(2): p. 470-480.
30. Kinsler, L.E., et al., *Fundamentals of acoustics*. 3 ed. 1982, New York: John Wiley and sons.
31. Kirchhoff, G.R., *Vorlesungen uber mathematische physik*. 1876: Leipzig.
32. Benade, A.H., *On the propagation of sound waves in a cylindrical conduit.* J.Acoust.Soc.Am, 1968. **44**(2): p. 616-623.
33. Benade, A.H. and Murday, J., *J. Measured end corrections for woodwind toneholes.* J.Acoust.Soc.Am, 1967. **41**: p. 1609-1610.
34. Backus, J., *Acoustic impedance of an annular capillary.* J.Acoust.Soc.Am, 1975. **58**(5): p. 1078-1081.
35. Keefe, D.H., *Experiments on the single woodwind tone hole.* J.Acoust.Soc.Am, 1982. **72**(3): p. 688-99.

36. Keefe., H.D., *Theory of the single woodwind hole.* J.Acoust.Soc.Am, 1982. **72**(3): p. 676-87.
37. Marshall, I., *The production of acoustic impulses in air.* Meas.Sci.Technol., 1990. **1**: p. 413-418.
38. Amir, N. and Shimony, U., *A Discrete Model for Tubular Acoustic Systems with Varying Cross Section, Part 1 Theory, Part 2 Experiments.* Acustica, 1995. **81**: p. 450-474.
39. Amir, N., Rosenhouse, G., and Shimony, U., *Losses in tubular acoustic systems - Theory and experiment in the sampled time and frequency domains.* . Acustica - Acta Acustica, 1996. **82**(1): p. 1-8.
40. *Encyclopedic dictionary of mathematics* 1986, Massachusetss, USA and London, England: The MIT press Cambridge
41. Atkinson, K.E., *An introduction to numerical analysis*. 1989, New York: John wiley and sons.
42. Dahlquist, G. and Bjorck, A., *Numerical methods* 1974: Englewood cliffs, New Jersy
43. Dennis, *Numerical methods for unconstrained optimisation* 1983, Englewood Cliffs, NJ: Prentice Hall
44. Murray, W., *Numerical methods for unconstrained optimisation*. 1972, London and New York: Academic press.
45. Hansen, *Global optimisation using interval analysis*. 1992, New York: Marcel Dekker, inc.
46. Nocedal, J., *Numerical optimisation* 1999, New York: Springer-Verlag.
47. Gould, *On the accurate determination of search directions for simple differentiable penalty functions* Journal on Numerical Analysis, 1986. **6** p. 357-372.
48. Hestenes, M.R. and Steifel, E., *Methods of conjugate gradients for sloving linear systems* J. Res. Nat. Bur. Standards, sec, 1952. **B, 49**: p. 409-439.
49. Steihaug, T., *The conjugate gradient method and trust regions in large scale optimisation. SIAM Journal on Numerical Analysis* Journal on Numerical Analysis, 1983. **20**: p. 626-637.
50. Neumaier, A., *Global optimistion* 2002: http://solon.cma.univie.ac.at/~neum/glopt.html.
51. Ross, C. and Terlaky, T., *Nonlinear optimisation*. 1998, TU Delft, Nietherlands.
52. Byrd, R.H. and Nocedal, J., *An analysis of reduced Hessian methods for constrained optimisation, mathematical programming* 1991. **49**: p. 285-323.

53. Al-Baali, *Descent property and global convergence of the Flecther-Reeves method with inexact line search* Journal on Numerical Analysis 1985: p. 121-124.
54. Rosenbrock, H.H., *An automatic Method for findong the greatest or least Value of a Function.* Comp. J., 1960. **3**: p. 175-184.
55. Anglmayer, P., Kausel, W., and Widholm, G., *A computer program for optimization of brass instruments. Part II. Application practical examples*, in *Forum Acusticum (Joint meeting of ASA+EAA+DEGA)*. 1999: Berlin.
56. Causse', R. and et al., *Input Impedance of Brass Musical Instruments - Comparison between Experimental and Numerical Models.* J.Acoust.Soc.Am, 1984. **75**: p. 241-54.
57. Kausel, W., *Computer optimization of Brass Wind instruments*. Diderot Forum on Mathematics and Music (Joint meeting in Wien/Paris/Lissabonn). 1999, OECG. 227-42.
58. Kausel, W., Anglmayer, P., and Widholm, G., *A computer program for optimization of brass instruments. Part 1. Concept, implementation*, in *Forum Acusticum (Joint meeting of ASA+EAA+DEGA)*. 1999: Berlin.
59. Stinson, M.R., *The propagation of plane sound waves in narrow and wide circular tubes, and generalisation to uniform tubes of arbitrary cross-sectional shapes.* J. Acoust. Soc. Am., 1990. **89**(2): p. 550-558.
60. Eiswirth, M. and Burn, L.S. *New methods for defect diagnosis of water pipelines* in *Proc. 4th Int. Conf. on Water Pipeline Systems*. 2001. York, UK.